Doctoral Dissertation

# Development of computational laser treatment based on multiscale analysis of picosecond laser-skin interactions

Yu Shimojo

December 2022

Graduate School of Engineering,
Osaka University

| | |
|---|---|
| Supervisor: | Professor Kunio Awazu<br>(Medical Beam Physics Laboratory) |
| Vice supervisors: | Professor Takanori Kitada<br>(Nuclear Social Engineering Laboratory)<br>Associate Professor Hisanao Hazama<br>(Medical Beam Physics Laboratory) |

# Abstract

Laser technology has been increasingly used to achieve minimally invasive treatment. The use of picosecond lasers for the treatment of pigmented lesions has been clinically investigated to improve the safety of the conventional nanosecond laser treatments. Despite its promising clinical results, rapid and effective clinical applications have been limited due to the difficulties in quantitative evaluation of the treatment effect. To tackle these problems, this study proposes "a computational laser treatment," a laser treatment platform for rapid and effective clinical applications of novel laser devices with reproducible and precise laser treatment in the physical world by quantitatively evaluating the treatment effect and designing a treatment protocol that maximizes the treatment outcome in a virtual world. As a specific example, a computational laser treatment using picosecond laser is developed to demonstrate the feasibility of computational clinical trials and the design of numerical indices for setting the irradiation parameters.

Chapter 1 provides the background on the utilization of lasers for minimally invasive treatments, summarizes the issues in the clinical application of picosecond lasers, and describes the concept of computational laser treatment. The significance of the proposed platform in preclinical and clinical trials and laser treatments is also presented.

Chapter 2 shows the optical properties of Asian epidermis, dermis, and subcutaneous fat measured with a double integrating sphere spectrophotometer and inverse Monte Carlo technique. A light transport model with the measured optical properties provided a quantitative evaluation of optical penetration depth and energy deposition in Asian skin for various combinations of irradiation parameters, which is difficult to measure in clinical studies.

Chapter 3 investigates the morphologies of melanosomes irradiated with picosecond laser analyzed by dynamic light scattering and scanning electron microscopy. The results confirmed that the threshold fluences for melanosome disruption were 2.19 and 2.49 J/cm$^2$ for 550- and 750-ps laser pulses, respectively. The thresholds obtained allow for the construction of a mathematical model to provide numerical indices for setting the irradiation parameters in computational laser treatment.

In Chapter 4, a nonlinear absorption-based analysis of melanin was performed to quantitatively evaluate energy deposition in melanosomes. Nonlinear absorption by melanin was found to have a significant influence on the treatment mechanism. The computational analysis demonstrates that the difference in treatment effect between picosecond and nanosecond lasers can be evaluated, augmenting preclinical and clinical evaluations.

Chapter 5 highlights the evaluation of photothermal skin damage caused by a novel picosecond laser device with a computational simulation of light propagation and thermal diffusion in skin. The photothermal damage caused by the novel device was shown to be less than that caused by the approved laser devices. The result of the comparison demonstrates that computational laser treatment can be applied to computational clinical trials for the partial replacement of preclinical

and clinical trials.

In Chapter 6, incident fluences of picosecond laser were calculated with a mathematical model based on the optical properties of the skin and the disruption threshold fluence. The validity of the calculated fluences was confirmed by comparison with the reported clinical study results. The simulation results demonstrate that computational laser treatment can provide numerical indices for setting distinct irradiation endpoints.

Chapter 7 discusses the prospects of the impacts of computational laser treatment on the processes of device development through regulatory evaluation to clinical use in the field of laser medicine.

Chapter 8 provides the overall conclusion. The proposed computational laser treatment offers a quantitative and reproducible evaluation method for picosecond laser treatment for the augmentation and partial replacement of preclinical and clinical trials and robust setting of irradiation parameters.

# List of Acronyms

| | |
|---|---|
| 3D | three-dimensional |
| DLS | dynamic light scattering |
| DMSO | dimethyl sulfoxide |
| EDTA | ethylenediaminetetraacetic acid |
| FDA | Food and Drug Administration |
| FWHM | full width at half maximum |
| iMC | inverse Monte Carlo |
| LIOB | laser-induced optical breakdown |
| MC | Monte Carlo |
| NIH | National Institute of Health |
| Nd:YAG | neodymium-doped yttrium aluminum garnet |
| NIR | near-infrared |
| PBS | phosphate-buffered saline |
| PIH | post-inflammatory hyperpigmentation |
| PMDA | Pharmaceuticals and Medical Devices Agency |
| RPE | retinal pigment epithelium |
| SD | standard deviation |
| SEM | scanning electron microscopy |
| UV | ultraviolet |
| VIS | visible |

# Contents

# List of Figures

# List of Tables

# Chapter 1

# Introduction

## 1.1 Laser treatment as a minimally invasive treatment

In an effort to achieve medical care that improves patient well-being and quality of life, laser technology has been increasingly used for diagnosis and therapy. Lasers are unique in their abilities of power density, directionality, coherence, monochromatic wavelength, and short pulse, which enable the delivery of energy to biological tissues selectively, with high resolution, and without contact. Depending on the parameters of the laser light, tissue can be affected by photobiological [1], photochemical [2], photothermal [3], or photomechanical [4] effects. The appropriate choice of irradiation parameters provides specific laser-tissue interactions for the treatment of target lesions or tumors. Thus, lasers are a versatile tool to provide a minimally invasive treatment that preserves the function and cosmetic appearance of organs. Many types of laser have been applied in a wide range of clinical departments, including dermatology [5], plastic surgery [6], cosmetic surgery [7], neurosurgery [8], ophthalmology [9], dentistry [10], and gastrointestinal surgery [11]. One property of using a laser over common surgical tools, such as a surgical knife, monopolar, bipolar, thermal cautery, and ultrasonic vibrations, is to provide a treatment without resection. The use of lasers is especially powerful in the treatment of organs where the preservation of cosmetic appearance is strongly desired, such as skin.

## 1.2 Clinical application of picosecond lasers for a potentially safe treatment

The use of picosecond lasers for the treatment of pigmented lesions has been clinically investigated to improve the safety of the conventional nanosecond laser treatments [6, 12]. Pigmented lesions are usually the result of abnormal production of dendritic melanocytes in the dermis or overproduction of melanin by melanocytes in the epidermis. These lesions often occur in Asians and cause cosmetic and psychological burdens on patients, which significantly reduces their quality of life [13]. Nanosecond lasers whose pulse width is shorter than the thermal relaxation time of melanosomes, approximately 50 ns, can confine heat inside melanosomes, and increase temperature owing to the high power density (see Fig. 1.1(a), (b)) [14]. This process induces selective disruption of

melanosomes, resulting in treatment effects [15, 16]. However, the long recovery time and the risk of complications, such as erythema, blistering, hypopigmentation, and PIH, remain major concerns for Asian skin, with its higher epidermal melanin content [17–20]. Picosecond lasers satisfy the thermal confinement condition of melanosomes more strongly than nanosecond lasers, and thus the damage is more localized to the lesions [21]. Furthermore, their pulse width is comparable to or shorter than the stress relaxation time of melanosomes, approximately 700 ps [22]. Picosecond lasers can generate a photomechanical effect more efficiently than nanosecond lasers to disrupt melanosomes (see Fig. 1.1(c)) [23]. The influence of different pulse widths on the treatment effect needs to be evaluated to provide well-established modalities for the treatment of pigmented lesions.

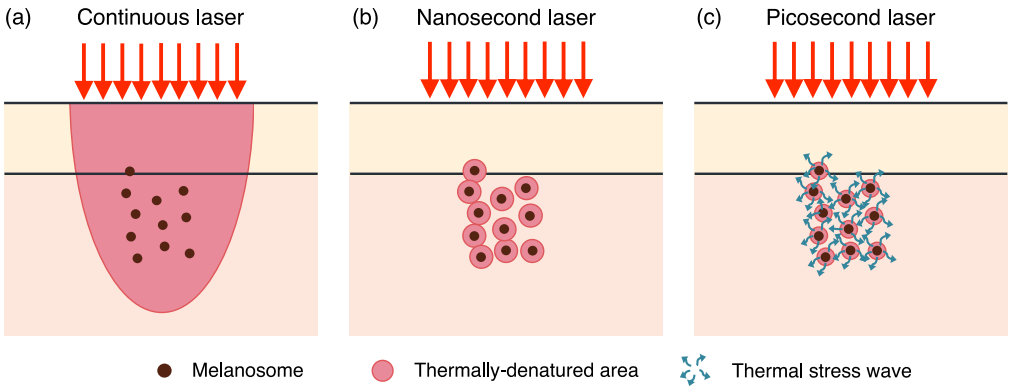


Figure 1.1: (a) Continuous lasers cause thermal diffusion to normal tissues. (b) Nanosecond lasers can confine heat inside melanosomes because the thermal confinement condition of melanosomes is satisfied. However, the long recovery time and the risk of complications remain major concerns for Asian skin. (c) Picosecond lasers can confine heat inside melanosomes more locally, and generate a photomechanical effect more efficiently than nanosecond lasers because their pulse widths are comparable to or shorter than the stress relaxation time of melanosomes.

## 1.3 Drawbacks in clinical evaluation and practice of picosecond laser

The evaluation of the safety and efficacy of picosecond laser irradiation to tissue is required for clinical applications. Because lasers inject energy into tissues, the light distribution in skin affects the treatment effect. However, direct measurements of spatial distributions of light and subsequent photothermal and photomechanical effects are difficult because of the high scattering nature of tissue. Furthermore, during picosecond laser, the physical phenomena are too fast to make direct observations. Therefore, the clinical evaluation of picosecond lasers has relied on statistical comparison of the safety and efficacy with nanosecond laser treatments and histological analysis of laser-irradiated tissues [24–29]. Picosecond laser treatments tended to record higher mean safety and efficacy scores than nanosecond laser treatments [26–29]. Controversially, some clinical studies reported significant differences in efficacy between picosecond and nanosecond lasers [27, 28], while other clinical studies with a similar protocol reported a different conclusion,

that the difference did not reach statistical significance [29]. Additionally, whether significant differences were detected varied between investigators and subjects [27, 28]. In terms of the setting of the irradiation parameters, the spot size was almost similar, ranging from 2 to 4 mm, but nanosecond laser treatments used approximately double the fluence of picosecond laser treatments [24, 26–29]. To resolve the ambiguities in the clinical evaluation, a laser-tissue interaction-based analysis is desired to quantitatively evaluate differences in treatment effect between different laser pulses.

In clinical practice, the appropriate choice of picosecond laser irradiation parameters, including wavelength, fluence, pulse width, and spot size, is critical to maximizing treatment outcome. It is urgently necessary to develop established indices to determine the irradiation parameters [30]. However, the current setting is highly dependent on the laser surgeon's skill and experience. The irradiation parameters are adjusted by their visual assessment of immediate or early tissue reactions after the laser shot [31]. Inappropriate settings cause adverse events such as scarring and burning. Additionally, there are clinical reports of successful clearance at low fluences without the skin reaction [32, 33]. These clinical study results suggest that it remains difficult to provide standardized treatment with picosecond laser. The irradiation parameters should be designed based on numerical indices to provide an optimal treatment protocol, leading to the determination of distinct irradiation endpoints. The drawbacks in clinical evaluation and practice of picosecond laser treatment are summarized in Fig. 1.2.

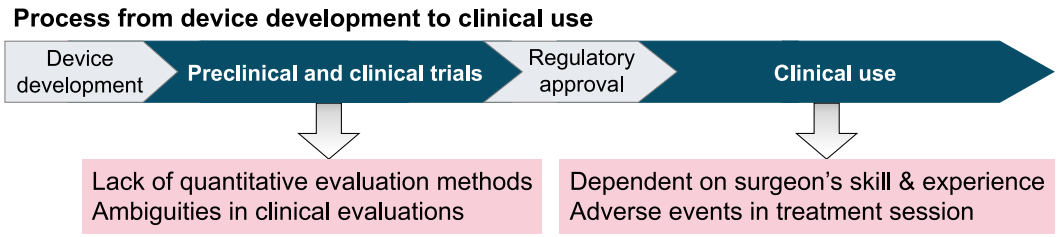


Figure 1.2: Drawbacks in the clinical evaluation and practice of picosecond laser.

## 1.4 Digital twin simulation of picosecond laser-skin interactions

In response to the above issues, digital twin simulations have the potential to provide a promising platform for evaluating the treatment effect and designing a treatment protocol. The "digital twin" concept is an *in silico* representation of the physical world to optimize design and control processes of products while connecting the physical world and a model in real time, and has been pioneered in engineering industries [34]. Recently, such computational approaches for regulatory evaluation and treatment have begun to be deployed in the medical field, including medical devices and pharmaceuticals [35–38]. By accurately reproducing the treatment procedure on a computer with virtual patient models obtained from measurements, the computational approach can overcome the difficulties in directly measuring the treatment effect and setting the treatment conditions.

For a digital twin simulation of picosecond laser treatment, mathematical models of picosecond

laser-skin interactions are required.With recent advances in computational modeling and simulation of biomedical optics, light transport models based on an MC method or diffusion approximation allow for computational simulations of physical phenomena in tissue induced by laser irradiation with high accuracy [39–41]. The mechanism of action of picosecond laser has been modeled from linear optical absorption and subsequent photothermal and photomechanical effects and has been computationally simulated at the tissue or cellular scale [23, 42–44]. In this model, the light distribution of short-pulsed lasers in skin tissue is calculated approximating the temporal pulse profile as a delta-like function [45], because the speed of light propagation in skin is much faster than the speed of thermal diffusion and stress propagation. However, it is not applicable to the evaluation of the impact of different pulse widths that satisfy the thermal and stress confinement conditions on the treatment effect. Furthermore, the high power density of a picosecond laser pulse causes nonlinear absorption by melanin [46]. The influence of nonlinear absorption by melanin on the treatment effect becomes more pronounced with increasing power density. The construction of mathematical models taking power density into account is essential for comparative evaluation between different laser pulses. The removal of pigmented lesions with short-pulsed lasers results from the disruption of melanosomes through the absorption of light propagated through the skin by the internal melanin [47]: The complex laser-skin interactions involve the tissue, cellular, and molecular scales. The construction of mathematical models requires a multiscale analysis of laser-skin interactions. In addition to mathematical models, physical parameters of the skin are necessary for computational simulations. Such parameters can be obtained using optical measurements such as spectroscopy and inverse problem analyses with the light transport model [48–50].

## 1.5 Concept of computational laser treatment

This study proposes "a computational laser treatment," a laser treatment platform for rapid and effective clinical applications of novel laser devices with reproducible and precise laser treatment in the physical world by quantitatively evaluating the treatment effect and designing a treatment protocol that maximizes the treatment outcome in a virtual world, as shown in Fig. 1.3. Laser-tissue interactions are quantified with computational simulations using mathematical models of laser treatment and optical structural data of the patient's tissue to evaluate the treatment effect. Because the irradiation parameters can be easily set on a computer, a comprehensive analysis of the irradiation parameters and a complement of physical phenomena that are difficult to measure in preclinical and clinical experiments can be taken into account in the evaluation. Furthermore, a treatment protocol that maximizes the treatment outcome can be designed by fast repetition of the above process based on the results of the evaluation. The designed treatment protocol can be reproduced using advanced optical devices and robot-assisted technology. The proposed platform will contribute to the establishment of computational clinical trials that augment and partially replace preclinical and clinical trials with reproducible and precise laser treatment regardless of the surgeon's skill and experience.

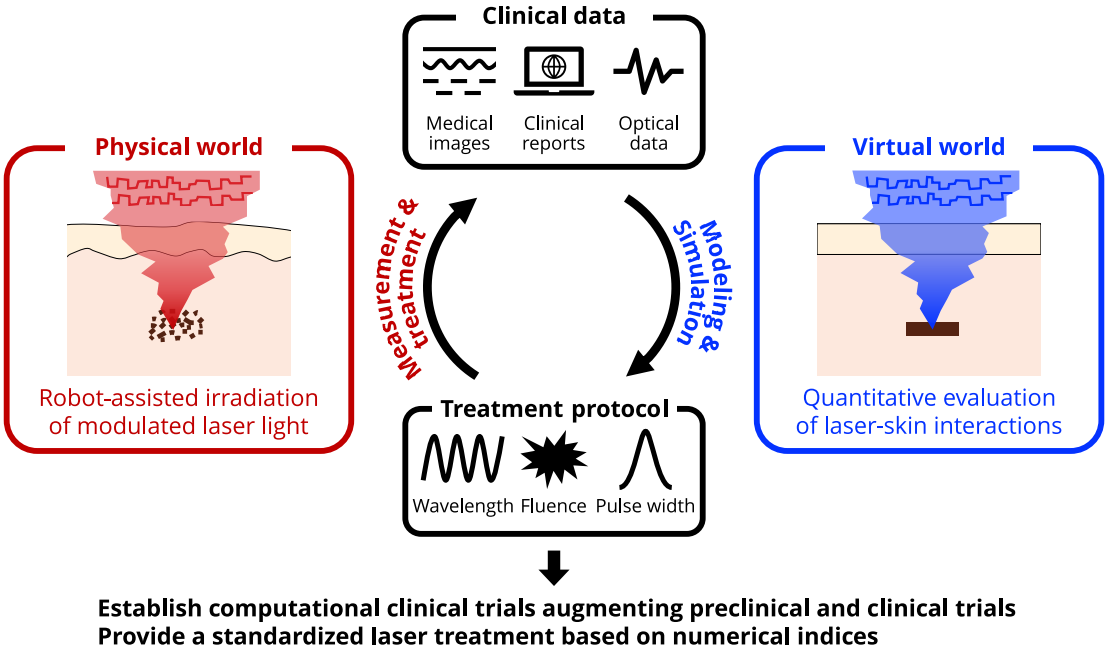


Figure 1.3: Concept of computational laser treatment. This platform quantitatively evaluates the treatment effect and designs a treatment protocol that maximizes the treatment outcome in a virtual world for rapid and effective clinical applications of novel laser devices with reproducible and precise laser treatment in the physical world.

## 1.6 Aim of this study

This study aims to develop a computational laser treatment using picosecond laser. Despite the potential of picosecond lasers to provide a highly safe treatment of pigmented lesions, rapid and effective clinical applications have been limited due to the difficulties in quantitative evaluation of the treatment effect. To address the issues, picosecond laser-skin interactions are experimentally and computationally analyzed at the tissue, cellular, and molecular scales to construct mathematical models of treatment and measure the physical parameters of the skin. The applicability of the developed computational laser treatment to partially replace preclinical and clinical trials and to achieve reproducible and precise laser treatment is then evaluated.

## 1.7 Outline of this dissertation

For multiscale analysis of picosecond laser-skin interactions, optical properties of Asian epidermis, dermis, and subcutaneous fat are measured with a DIS spectrophotometer and iMC technique to quantitatively evaluate picosecond laser propagation in skin tissue in Chapter 2. Threshold fluences of picosecond laser for melanosome disruption are determined with DLS and SEM in Chapter 3. A nonlinear absorption-based analysis of melanin is performed to quantitatively evaluate energy deposition in melanosomes in Chapter 4. For rapid and effective clinical applications of novel laser devices, the feasibility of computational clinical trial is demonstrated by evaluating the

photothermal skin damage caused by a picosecond laser device with a computational simulation of light propagation and thermal diffusion in skin in Chapter 5. Incident fluences of picosecond laser are calculated with a mathematical model based on the optical properties of the skin and the threshold fluences for melanosome disruption to provide numerical indices for setting the irradiation parameters in Chapter 6. The prospects of computational laser treatment are discussed in Chapter 7. The overall conclusion is provided in Chapter 8.

## References


[1] M. Mitsunaga, M. Ogawa, N. Kosaka, L.T. Rosenblum, P.L. Choyke, and H. Kobayashi. Cancer cell-selective *in vivo* near infrared photoimmunotherapy targeting specific membrane molecules. *Nature Medicine*, 17(12):1685–1691, 2011.

[2] S. Mallidi, S. Anbil, A.L. Bulin, G. Obaid, M. Ichikawa, and T. Hasan. Beyond the barriers of light penetration: Strategies, perspectives and possibilities for photodynamic therapy. *Theranostics*, 6(13):2458–2487, 2016.

[3] H. Arami, S. Kananian, L. Khalifehzadeh, C.B. Patel, E. Chang, Y. Tanabe, Y. Zeng, S.J. Madsen, M.J. Mandella, A. Natarajan, and others. Remotely controlled near-infrared-triggered photothermal treatment of brain tumours in freely behaving mice using gold nanostars. *Nature Nanotechnology*, 17(9):1015–1022, 2022.

[4] D. Eversole, K. Subramanian, R.K. Harrison, F. Bourgeois, A. Yuksel, and A. Ben-Yakar. Femtosecond Plasmonic Laser Nanosurgery (fs-PLN) mediated by molecularly targeted gold nanospheres at ultra-low pulse fluences. *Scientific Reports*, 10(1):1–16, 2020.

[5] S.R. Mercuri, P. Brianti, A. Dattola, L. Bennardo, M. Silvestri, G. Schipani, and S.P. Nisticò. $CO_2$ laser and photodynamic therapy: Study of efficacy in periocular BCC. *Dermatologic Therapy*, 31(4):e12616, 2018.

[6] C. Chesnut, J. Diehl, and G. Lask. Treatment of nevus of Ota with a picosecond 755-nm alexandrite laser. *Dermatologic Surgery*, 41(4):508–510, 2015.

[7] E. Russe, M. Purschke, M. Herold, F.H. Sakamoto, G. Wechselberger, and K. Russe-Wilflingseder. Evaluation of safety and efficacy of laser hair removal with the long-pulsed 755 nm wavelength laser: A two-center study with 948 patients. *Lasers in Surgery and Medicine*, 52(1):77–83, 2020.

[8] W.A. Ross, W.M. Hill, K.B. Hoang, A.S. Laarakker, B.P. Mann, and P.J. Codd. Automating neurosurgical tumor resection surgery: Volumetric laser ablation of cadaveric porcine brain with integrated surface mapping. *Lasers in Surgery and Medicine*, 50(10):1017–1024, 2018.

[9] C.K. Hwang, G.B. Hubbard, A.K. Hutchinson, and S.R. Lambert. Outcomes after intravitreal bevacizumab versus laser photocoagulation for retinopathy of prematurity: A 5-year retrospective analysis. *Ophthalmology*, 122(5):1008–1015, 2015.

[10] V. Akhavan Zanjani, H. Ahmadi, A. Nateghifard, A. Ghasemi, H. Torabzadeh, M. Abdoh Tabrizi, F. Alikhani, R. Razi, and A. Nateghifard. Effect of different laser surface treatment on microshear bond strength between zirconia ceramic and resin cement. *Journal of Investigative and Clinical Dentistry*, 6(4):294–300, 2015.

[11] T. Noguchi, H. Hazama, T. Nishimura, Y. Morita, and K. Awazu. Enhancement of the safety and efficacy of colorectal endoscopic submucosal dissection using a $CO_2$ laser. *Lasers in Medical Science*, 35(2):421–427, 2020.

[12] M.W. Chan, S.Y.N. Shek, C.K. Yeung, and H.H.L. Chan. A prospective study in the treatment of lentigines in Asian skin using 532 nm picosecond Nd:YAG laser. *Lasers in Surgery and Medicine*, 51(9):767–773, 2019.

[13] L. Raveendra, H. Sidappa, and S. Shree. A study of quality of life in patients with facial melanoses. *Indian Dermatology Online Journal*, 11(2):154–157, 2020.

[14] R.R. Anderson and J.A. Parrish. Selective Photothermolysis: Precise Microsurgery by Selective Absorption of Pulsed Radiation. *Science*, 220(4596):524–527, 1983.

[15] L.L. Polla, R.J. Margolis, J.S. Dover, D. Whitaker, G.F. Murphy, S.L. Jacques, and R.R. Anderson. Melanosomes are a primary target of Q-switch ruby laser irradiation in guinea pig skin. *Journal of Investigative Dermatology*, 89(3):281–286, 1987.

[16] R.R. Anderson, R.J. Margolis, S. Watenabe, T. Flotte, G.J. Hruza, and J.S. Dover. Selective photothermolysis of cutaneous pigmentation by Q-switched Nd:YAG laser pulses at 1064, 532, and 355 nm. *Journal of Investigative Dermatology*, 93(1):28–32, 1989.

[17] H.H. Chan, R.S.C. Leung, S.Y. Ying, C.F. Lai, T. Kono, J.K.H. Chua, and W.S. Ho. A retrospective analysis of complications in the treatment of nevus of Ota with the Q-switched alexandrite and Q-switched Nd:YAG Lasers. *Dermatologic Surgery*, 26(11):1000–1006, 2000.

[18] T. Kono, D. Manstein, H.H. Chan, M. Nozaki, and R.R. Anderson. Q-switched ruby versus long-pulsed dye laser delivered with compression for treatment of facial lentigines in Asians. *Lasers in Surgery and Medicine*, 38(2):94–97, 2006.

[19] S. Ho, C. Yeung, N. Chan, S. Shek, and H. Chan. A comparison of Q-switched and long-pulsed alexandrite laser for the treatment of freckles and lentigines in oriental patients. *Lasers in Surgery and Medicine*, 43(2):108–113, 2011.

[20] T. Kono, S.Y. Shek, H.H. Chan, W.F. Groff, K. Imagawa, and T. Akamatsu. Theoretical review of the treatment of pigmented lesions in Asian skin. *Laser Therapy*, 25(3):179–184, 2016.

[21] S. Watanabe, R.R. Anderson, S. Brorson, G. Dalickas, J.G. Fujimoto, and T.J. Flotte. Comparative studies of femtosecond to microsecond laser pulses on selective pigmented cell injury in skin. *Photochemistry and Photobiology*, 53(6):757–762, 1991.

[22] J. Neumann and R. Brinkmann. Boiling nucleation on melanosomes and microbeads transiently heated by nanosecond and microsecond laser pulses. *Journal of Biomedical Optics*, 10(2):024001, 2005.

[23] D.D.M. Ho, R. London, G.B. Zimmerman, and D.A. Young. Laser-tattoo removal—a study of the mechanism and the optimal treatment strategy via computer simulations. *Lasers in Surgery and Medicine*, 30(5):389–397, 2002.

[24] K. Negishi, H. Akita, and Y. Matsunaga. Prospective study of removing solar lentigines in Asians using a novel dual-wavelength and dual-pulse width picosecond laser. *Lasers in Surgery and Medicine*, 50(8):851–858, 2018.

[25] Y. Yang, L. Peng, Y. Ge, and T. Lin. Comparison of the efficacy and safety of a picosecond alexandrite laser and a Q-switched alexandrite laser for the treatment of freckles in Chinese patients. *Journal of the American Academy of Dermatology*, 79(6):1155–1156, 2018.

[26] Y. Ge, Y. Yang, L. Guo, M. Zhang, Q. Wu, R. Zeng, H. Rong, G. Jia, H. Shi, J. Fang, and T. Lin. Comparison of a picosecond alexandrite laser versus a Q-switched alexandrite laser for the treatment of nevus of Ota: A randomized, split-lesion, controlled trial. *Journal of the American Academy of Dermatology*, 83(2):397–403, 2020.

[27] C. Ungaksornpairote, W. Manuskiatti, N. Junsuwan, and R. Wanitphakdeedecha. A prospective, split-face, randomized study comparing picosecond to Q-switched Nd:YAG laser for treatment of epidermal and dermal pigmented lesions in Asians. *Dermatologic Surgery*, 46(12):1671–1675, 2020.

[28] J.Y. Kim, J. Yang, G. Huh, Y.J. Choi, and W.S. Kim. A split-face, single-blinded, randomized controlled comparison of 532 nm picosecond neodymium-doped yttrium aluminum garnet laser versus 532 nm Q-switched neodymium-doped yttrium aluminum garnet laser in the treatment of solar lentigines. *Annals of Dermatology*, 32(1):8–13, 2020.

[29] V. Vachiramon, W. Iamsumang, and K. Triyangkulsri. Q-switched double frequency Nd:YAG 532-nm nanosecond laser vs. double frequency Nd:YAG 532-nm picosecond laser for the treatment of solar lentigines in Asians. *Lasers in Medical Science*, 33(9):1941–1947, 2018.

[30] D.C. Wu, M.P. Goldman, H. Wat, and H.H. Chan. A systematic review of picosecond laser in dermatology: Evidence and recommendations. *Lasers in Surgery and Medicine*, 53(1):9–49, 2021.

[31] M. Wanner, F.H. Sakamoto, M.M. Avram, H.H. Chan, M. Alam, Z. Tannous, and R.R. Anderson. Immediate skin responses to laser and light treatments: Therapeutic endpoints:

How to obtain efficacy. *Journal of the American Academy of Dermatology*, 74(5):821–833, 2016.

[32] R. Sakio, T. Ohshiro, K. Sasaki, and T. Ohshiro. Usefulness of picosecond pulse alexandrite laser treatment for nevus of Ota. *Laser Therapy*, 27(4):251–255, 2018.

[33] T. Ohshiro, T. Ohshiro, K. Sasaki, and K. Kishi. Picosecond pulse duration laser treatment for dermal melanocytosis in Asians: A retrospective review. *Laser Therapy*, 25(2):99–104, 2016.

[34] F. Tao, M. Zhang, Y. Liu, and A. Nee. Digital twin driven prognostics and health management for complex equipment. *CIRP Annals*, 67(1):169–172, 2018.

[35] S.A. Niederer, J. Lumens, and N.A. Trayanova. Computational models in cardiology. *Nature Reviews Cardiology*, 16(2):100–111, 2019.

[36] P.M. Boyle, T. Zghaib, S. Zahid, R.L. Ali, D. Deng, W.H. Franceschi, J.B. Hakim, M.J. Murphy, A. Prakosa, S.L. Zimmerman, and others. Computationally guided personalized targeted ablation of persistent atrial fibrillation. *Nature Biomedical Engineering*, 3(11):870–879, 2019.

[37] B. Björnsson, C. Borrebaeck, N. Elander, T. Gasslander, D.R. Gawel, M. Gustafsson, R. Jörnsten, E.J. Lee, X. Li, S. Lilja, and others. Digital twins to personalize medicine. *Genome Medicine*, 12(1):1–4, 2020.

[38] M. Viceconti, F. Pappalardo, B. Rodriguez, M. Horner, J. Bischoff, and F.M. Tshinanu. *In silico* trials: Verification, validation and uncertainty quantification of predictive models used in the regulatory evaluation of biomedical products. *Methods*, 185:120–127, 2021.

[39] S.L. Jacques. Coupling 3D Monte Carlo light transport in optically heterogeneous tissues to photoacoustic signal generation. *Photoacoustics*, 2(4):137–142, 2014.

[40] S. Yan and Q. Fang. Hybrid mesh and voxel based Monte Carlo algorithm for accurate and efficient photon transport modeling in complex bio-tissues. *Biomedical Optics Express*, 11(11):6262–6270, 2020.

[41] H. Elkhalil, A. Alshare, G. Shafirstein, and J. Bischof. A three-dimensional transient computational study of 532-nm laser thermal ablation in a geometrical model representing prostate tissue. *International Journal of Hyperthermia*, 35(1):568–577, 2018.

[42] A. Humphries, T.S. Lister, P.A. Wright, and M.P. Hughes. Finite element analysis of thermal and acoustic processes during laser tattoo removal. *Lasers in Surgery and Medicine*, 45(2):108–115, 2013.

[43] J. Tian, B. Chen, and D. Li. Efficacy evaluation and treatment parameter optimization for laser surgery of Ota's nevus based on an advanced non-equilibrium bio-tissue heat transfer model. *Lasers in Medical Science*, 37(1):369–379, 2022.

[44] M. Luecking, R. Brinkmann, S. Ramos, W. Stork, and N. Heussner. Capabilities and limitations of a new thermal finite volume model for the evaluation of laser-induced thermomechanical retinal damage. *Computers in Biology and Medicine*, 122:103835, 2020.

[45] M. Xu and L.V. Wang. Photoacoustic imaging in biomedicine. *Review of Scientific Instruments*, 77(4):041101, 2006.

[46] D.J. Stolarski, J. Stolarski, R.J. Thomas, G.D. Noojin, K.J. Schuster, and B.A. Rockwell. Nonlinear absorption studies of melanin. *Proceedings of SPIE*, 4617:161–171, 2002.

[47] S.L. Jacques and D.J. McAuliffe. The melanosome: Threshold temperature for explosive vaporization and internal absorption coefficient during pulsed laser irradiation. *Photochemistry and Photobiology*, 53(6):769–775, 1991.

[48] L.V. Wang and S. Hu. Photoacoustic tomography: In vivo imaging from organelles to organs. *Science*, 335(6075):1458–1462, 2012.

[49] M. Siddiqui, A.S. Nam, S. Tozburun, N. Lippok, C. Blatter, and B.J. Vakoc. High-speed optical coherence tomography by circular interferometric ranging. *Nature Photonics*, 12(2):111–116, 2018.

[50] N. Verdel, J. Tanevski, S. Džeroski, and B. Majaron. Predictive model for the quantitative analysis of human skin using photothermal radiometry and diffuse reflectance spectroscopy. *Biomedical Optics Express*, 11(3):1679–1696, 2020.

# Chapter 2

# Measurement of optical properties of Asian epidermis, dermis, and subcutaneous fat

## 2.1 Introduction

Light distributions in skin tissue provide fundamental information for predicting the outcome of computational laser treatment using picosecond laser [1]. Skin tissue consists primarily of three layers, including the epidermis, dermis, and subcutaneous fat. The irradiated pulsed light is scattered and absorbed while propagating through each layer. The light absorbed by the lesions is translated into photothermal and photomechanical effects, resulting in treatment effects. On the other hand, excessive light absorption by normal tissue surrounding the lesions risks thermal damage. The light distribution in skin tissues is therefore a key factor in predicting the treatment outcome. One limitation in the prediction is the difficulty in direct measurements of light distribution in tissue due to scattering and absorption.

Light transport models based on an MC method and physical parameters including optical properties and structural parameters of tissues have been developed to evaluate optical diagnosis and laser treatment [2, 3]. These models enable computational simulations to calculate light distribution in skin tissues, overcoming the technical challenges associated with direct measurements. The accuracy of the simulated light distribution depends on the optical properties because they differ depending on the skin type. Since pigmented lesions are common in Asians, high accuracy of the optical properties of Asian skin tissues is necessary to evaluate the safety and efficacy of picosecond laser treatment. Several papers have reported optical properties of each skin layer obtained from *in vitro* measurements [4, 5]; however, all the works have measured only Caucasian and African skin tissues. The validity of estimating the absorption coefficients of each Asian skin layer from the concentrations of chromophores, including blood, water, and melanin, has not yet

This chapter was originally published under the title, "Measurement of absorption and reduced scattering coefficients in Asian epidermis, dermis, and subcutaneous fat tissues in the 400- to 1100-nm wavelength range for optical penetration depth and energy deposition analysis" by Yu Shimojo, Takahiro Nishimura, Hisanao Hazama, Toshiyuki Ozawa, and Kunio Awazu in *Journal of Biomedical Optics* 25(4):045002 (2020).

been verified in detail. Although *in vivo* measurements have also been performed [6, 7], optical properties and structural data of each layer cannot be easily determined because there are a large number of variables involved in solving inverse problems [8, 9]. The construction of a virtual human skin model with optical properties of Asian skin tissues allows for the calculation of light distributions in Asian skin with higher accuracy in computational laser treatment.

This chapter presents a measurement of the optical properties of Asian epidermis, dermis, and subcutaneous fat in the VIS–NIR range with a DIS spectrophotometer and iMC technique. The use of this spectrophotometer allows the simultaneous measurement of diffuse reflectance $R_\mathrm{d}$ and total transmittance $T_\mathrm{t}$, and reduces sample degradation during measurement. When comparing measured $R_\mathrm{d}$ and $T_\mathrm{t}$ with simulated $R_\mathrm{d}$ and $T_\mathrm{t}$ with the iMC technique, respectively, the optical properties of Asian epidermis, dermis, and subcutaneous fat can be obtained. To confirm the validity of the measured optical properties of each layer, the measured values are compared with the reported values for Caucasian and African skin tissues. Using a light transport model with the measured optical properties, computational simulations are performed to analyze optical penetration depth $\delta$ and energy deposition $S$ for different types of skin and various combinations of irradiation parameters. These analyses allow for the complement of measurement data that are difficult to obtain in preclinical and clinical experiments due to technical challenges [10]. Therefore, computational simulations will provide laser device manufacturers and laser surgeons with a better understanding of the light behavior in each layer of Asian skin and how changes in skin types can cause differences in light distribution in skin.

## 2.2 Materials and Methods

### 2.2.1 Sample preparation

Freshly discarded specimens of Japanese human skin tissue were obtained from surgeries at the Department of Dermatology of Osaka City University, immersed in a solution of saline, and then delivered to Osaka University. A study protocol approved by the Research Ethics Committee of Osaka University (approval number: R 29) and the Ethics Committee of the Graduate School of Medicine of Osaka City University (approval number: 4252) was followed and each participating patient signed an informed consent form before surgeries. Skin specimens from the face, abdomen, thigh, axilla, clavicle, and ear of adult patients were used. The specimens were stored at low temperature (4°C) until sectioned into the epidermis, dermis, and subcutaneous fat. The number of sectioned specimens was 21, 20, and 15, respectively. In total, 15 epidermis samples, 20 dermis samples, and 15 subcutaneous fat samples were successfully separated and then measured and analyzed. The time taken from sample preparation to measurement did not exceed 50 hours for the epidermis and dermis and 12 hours for the subcutaneous fat. The subcutaneous fat was cut with surgical scissors. The epidermis and dermis were then separated with surgical tweezers using a split skin technique [11]. The skin samples were incubated in PBS (163-25265, FUJIFILM Wako Pure Chemical Corporation, Japan) containing 2 mM EDTA (06894-14, Nacalai Tesque, Japan) and 1 mM phenylmethylsulfonyl fluoride (160-12183, FUJIFILM Wako Pure Chemical Corporation) for

48 hours at 4°C with a daily exchange of the solution. The thickness of each section was measured at three points using a high-precision digital micrometer (MDE-25MX, Mitutoyo, Japan) with a precision of ±1 $\mu$m and averaged. The thickness of the epidermis, dermis, and subcutaneous fat sections ranged from 0.09 to 0.32, 1.03 to 2.10, and 1.21 to 1.90 mm, respectively. The lateral size of the sectioned tissues was around 20 mm × 20 mm. The sections were sandwiched between glass slides (S1112, Matsunami Glass Ind., Japan) without (or with minimal) compression, and the thickness was fixed using spacers. The samples were sealed with scotch tape to prevent desiccation during measurement.

### 2.2.2 DIS spectrophotometer

The $R_d$ and $T_t$ were obtained with a DIS spectrophotometer (see Fig. 2.1) as previously reported [12]. In the setup, a xenon lamp (L2273 and C8849, Hamamatsu Photonics, Japan) was used. The light was focused into a 1 mm spot on the sample, which was mounted between the 100 mm outer diameter reflectance and transmittance spheres (CSTM-3P-GPS-033SL, Labsphere, USA). The integrating spheres were made of Spectralon®, which is a solid thermoplastic that exhibits the highest diffuse reflectance of any material or coating in the 250–2500 nm band. All ports of the integrating spheres had a diameter of 10 mm. The sample size was larger than the diameter of the sample port. After incident light was illuminated onto the samples, the diffusely reflected and transmitted light from the sample was diffused in the integrating spheres and then detected through an optical fiber (CUSTOM-PATCH-2243142, Ocean Optics, USA) connected to a spectrometer (MAYP10161, Maya2000-Pro, Ocean Optics) that is sensitive in the 400–1100 nm wavelength range. The exposure time for the measurement was 500 ms. $R_d$ and $T_t$ were measured at five points in the samples and averaged. The DIS spectrophotometer was calibrated using a diffuse reflectance standard (SRS-20-010, Labsphere) and a transmittance filter (JCRM130, Japan Quality Assurance Organization, Japan). A diffuse reflectance standard (SRS-99-010, Labsphere) and a beam trap (BT610, Thorlabs, USA) were used to measure the background of the $R_d$ spectrum.

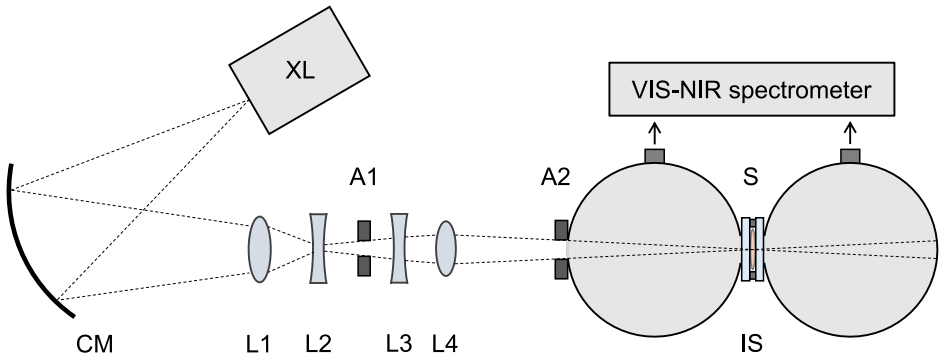


Figure 2.1: Schematic diagram of DIS spectrophotometer. A1, aperture ($\phi$ = 1 mm); A2, aperture ($\phi$ = 4 mm); CL, concave mirror; IS, integrating spheres; L1, convex lens (f = 70 mm); L2, concave lens (f = −60 mm); L3, concave lens (f = −50 mm); S, Sample; L4, convex lens (f = 30 mm); XL, xenon lamp.

The $R_d$ difference between the measured and standard values was found to be within 0.7% for wavelengths below 1000 nm and within 2.5% above 1000 nm (Figs. 2.2(a),(c)). The larger difference above 1000 nm was caused by the wavelength dependence of the integrating spheres and the spectrometer. The reflectance of the integrating spheres and the detection sensitivity of the spectrometer decreased in the NIR range. The difference in the measured $T_t$ was within 0.2% (Figs. 2.2(b),(d)). All measurements were made at room temperature (23°C).

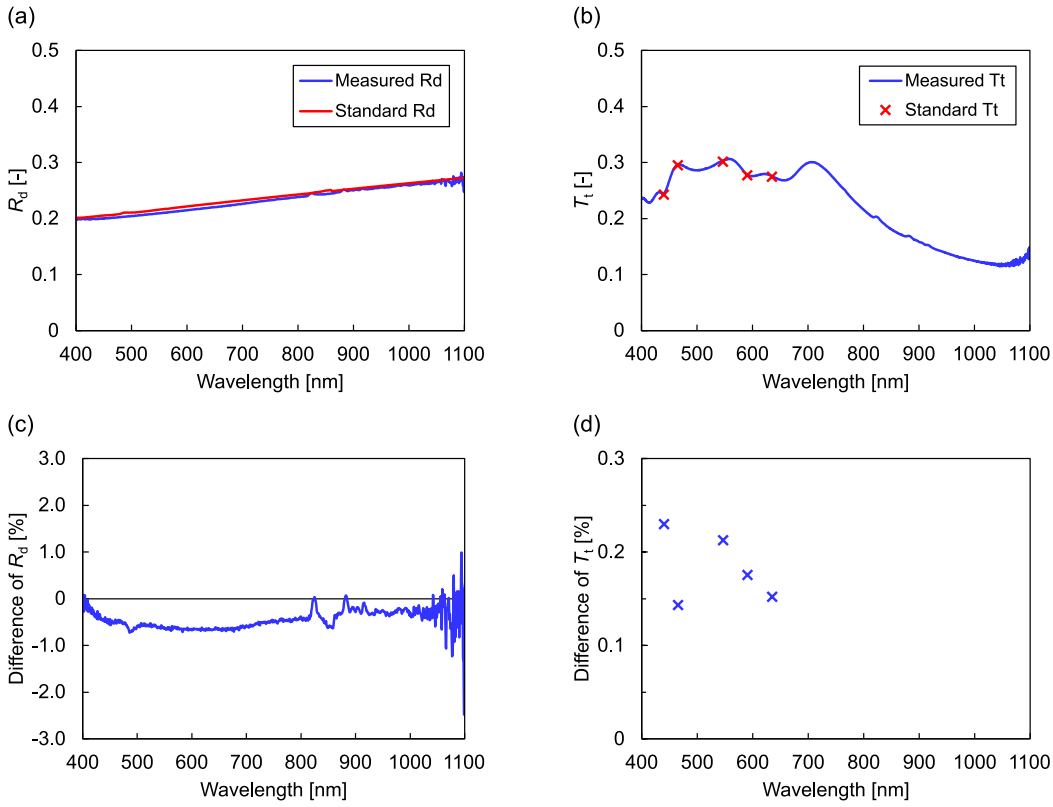


Figure 2.2: (a), (b) Comparison of the measured and standard values of diffuse reflectance $R_d$ and total transmittance $T_t$, respectively. (c), (d) Differences between the measured and standard values of $R_d$ and $T_t$, respectively.

### 2.2.3 Data processing technique

The optical properties were determined from the measured diffuse reflectance $R_{d,exp.}$ and total transmittance $T_{t,exp.}$ with an iMC technique [12]. First, possible ranges of optical property values were estimated according to Ref. [13] and sets of optical properties were prepared in 0.1 $mm^{-1}$ increments. The diffuse reflectance $R_{d,cal.}$ and the total transmittance $T_{t,cal.}$ were then calculated with the sets of optical properties prepared and the geometry of the sample using an MC simulation [14]. The $R_{d,cal.}$ and $T_{t,cal.}$ values were then compared with the $R_{d,exp.}$ and $T_{t,exp.}$ values, respectively, and the differences were calculated. Finally, the estimated optical properties were accepted as the optical properties of the samples if the relative differences were smaller than 0.5%. Otherwise,

sets of optical properties that minimized the differences between the measured and calculated values were taken, and the above steps were repeated in smaller increments until the measured and calculated values were agreed upon within 0.5%. This iterative process produced the set of optical properties of each skin layer that most closely matched the $R_{d,exp}$ and $T_{t,exp}$ values. The anisotropy factor $g$ was assumed to be 0.9, which is a typical value for many types of tissue [15]. The refractive indices of epidermis, dermis, and subcutaneous fat were fixed at 1.34, 1.39, and 1.44 at a wavelength of 633 nm, respectively [3].

### 2.2.4 Geometry of the modeled skin tissue

To calculate $\delta$ and $S$ using the measured optical properties, a virtual human skin model was constructed. Figure 2.3 shows the skin model consisting of the epidermis, dermis, and subcutaneous fat. In the dermis, three different sizes of blood vessels, namely the capillary plexus, the upper dermis blood vessels, and the deep dermis blood vessels, were modeled to simulate the distribution of blood vessels. Table 2.1 shows the parameters of the blood vessels used in the model [16]. The capillary plexus was 150 $\mu$m in thickness. The upper dermis blood vessels and the deep dermis blood vessels were lined at a depth of 340 and 1210 $\mu$m, respectively. The skin model was constructed using $500 \times 500 \times 400$ cubic voxels. The size of each voxel was 10 $\mu$m $\times$ 10 $\mu$m $\times$ 10 $\mu$m. The depth direction was set as the $z$ axis. The skin surface was set at $z = 0$ mm. The center of the model on the $xy$ plane was set at $(x, y) = (0 \text{ mm}, 0 \text{ mm})$. The thicknesses of the epidermis and dermis layer were set to the average of the measured values.

### 2.2.5 Optical penetration depth and energy deposition analysis

A 3D MC simulation was performed to calculate $\delta$ and $S$ [17]. This computational simulation enables a calculation of the light distribution in a complex tissue composed of many types of tissue, each with its own optical properties. Uniform circular beams with diameters of 2, 3, and 4 mm were assumed to enter the skin model vertically at $(x, y) = (0 \text{ mm}, 0 \text{ mm})$. The $\delta$ and $S$ were calculated at wavelengths of 405, 532, 595, 632, 694, 755, 800, 980, and 1064 nm, which are available for current picosecond laser treatment. The measured optical properties at each wavelength were assigned in the skin model. The optical properties of human blood at each wavelength are summarized in Table 2.2 [18–20]. The blood oxygen saturation was 96%. The $g$ was assumed to be 0.9 [15]. The simulation was carried out for 180 million photons to achieve a sufficient distribution of light fluence in the skin tissue.

Table 2.1: Parameters of blood vessels. Table reproduced with permission from Ref. [21].

| | Depth of the center [$\mu$m] | Volume fraction [%] | Diameter [$\mu$m] |
|---|---|---|---|
| Capillary plexus | 230 | 4 | 10 |
| Upper dermis blood vessel | 340 | 30 | 50 |
| Deep dermis blood vessel | 1210 | 10 | 80 |

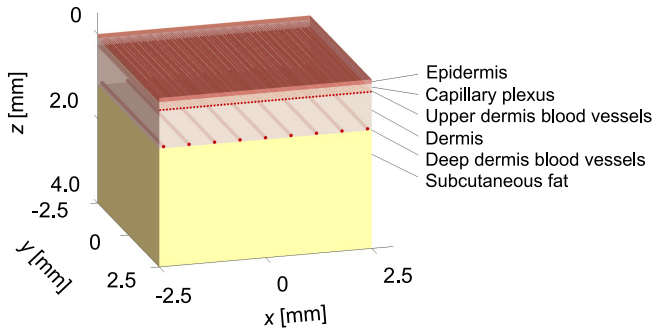


Figure 2.3: Virtual human skin tissue model consisting of the epidermis, dermis, subcutaneous fat, and three kinds of blood vessels (capillary plexus, upper dermis blood vessels, and deep dermis blood vessels). Figure reproduced with permission from Ref. [21].

Table 2.2: Absorption $\mu_a$ and reduced scattering $\mu_s'$ coefficients of human whole blood. The blood oxygen saturation was 96%. Table reproduced with permission from Ref. [21].

| Wavelength [nm] | $\mu_a$ [mm$^{-1}$] | $\mu_s'$ [mm$^{-1}$] |
|---|---|---|
| 405 | 176.03 | 2.53 |
| 532 | 23.43 | 2.11 |
| 595 | 3.89 | 1.96 |
| 632 | 0.39 | 1.88 |
| 694 | 0.19 | 1.77 |
| 755 | 0.32 | 1.68 |
| 800 | 0.44 | 1.61 |
| 980 | 0.59 | 1.41 |
| 1064 | 0.30 | 1.34 |

## 2.3 Results

### 2.3.1 Optical properties of Asian epidermis, dermis, and subcutaneous fat

The optical properties of Asian epidermis, dermis, and subcutaneous fat were measured in the 400–1100 nm wavelength range. Figure 2.4 shows the $R_d$ and $T_t$ spectra of Asian epidermis, dermis, and subcutaneous fat. The optical properties were obtained by comparing the measured $R_d$ and $T_t$ values with the values calculated with the iMC technique. Figure 2.5(a) shows the absorption coefficient $\mu_a$ spectra of epidermis, dermis, and subcutaneous fat. The higher SDs compared to the detection sensitivity of the optical setup were caused by individual differences and body-site differences of the samples used. The $\mu_a$ values of the epidermis decreased with increasing wavelength. The absorption by the epidermis was remarkably higher than that by the dermis and subcutaneous fat due to the large absorption by melanin in the epidermis. The absorption by melanin increases steadily at shorter wavelengths over the 250–1200 nm wavelength range [22]. There was a marked dispersion of the $\mu_a$ values in the 400–600 nm wavelength range owing to the difference in melanin content between samples obtained from photoexposed and photoprotected skin [23]. In the $\mu_a$ spectrum of the dermis, hemoglobin absorption peaks at 403 and 573 nm and a water absorption peak at 968 nm were observed. The hemoglobin absorption peaks were not pronounced, because the blood in the samples was removed during the sample preparation. In the $\mu_a$ spectrum of the subcutaneous fat, hemoglobin absorption peaks appeared around 416 and 575 nm, and a broad band of bilirubin absorption between 400 and 500 nm. The increase in SD in the absorption bands was caused by differences in blood content in different tissue samples. Figure 2.5(b) shows the reduced scattering coefficient $\mu_s'$ spectra of epidermis, dermis, and subcutaneous fat. The $\mu_s'$ values of the epidermis were noticeably higher than those of dermis and subcutaneous fat. The $\mu_s'$ values decreased with increasing wavelength. The steady decrease could be attributed to the decrease in the contribution of Rayleigh scattering and the increase in the contribution of Mie scattering with increasing wavelength [24].

### 2.3.2 Effect of sample preparation on optical properties

The sample preparation technique could have influenced the evaluation of the optical properties [25, 26]. The effect of sample preparation during epidermis and dermis separation was investigated by comparing the optical properties of skin tissue consisting of epidermis and dermis (epidermis + dermis) before and after sample preparation. For measurement before sample preparation, epidermis + dermis separated from subcutaneous fat was immediately used. For measurements after sample preparation, the same epidermis + dermis was immersed in PBS for 48 hours at 4°C. Figure 2.6 shows the $\mu_a$ and $\mu_s'$ spectra of epidermis + dermis before and after sample preparation, and the relative difference of the $\mu_a$ and $\mu_s'$ values after sample preparation. The mean $\mu_a$ after sample preparation was lower than before sample preparation. The largest difference in the $\mu_a$ values was −35% at 432 nm. In the 400–570 nm wavelength range, the difference was significant because most of the blood in the sample was removed by the soak solution. However, in the wavelength range longer than 570 nm, the relative difference was within the SD of the result before

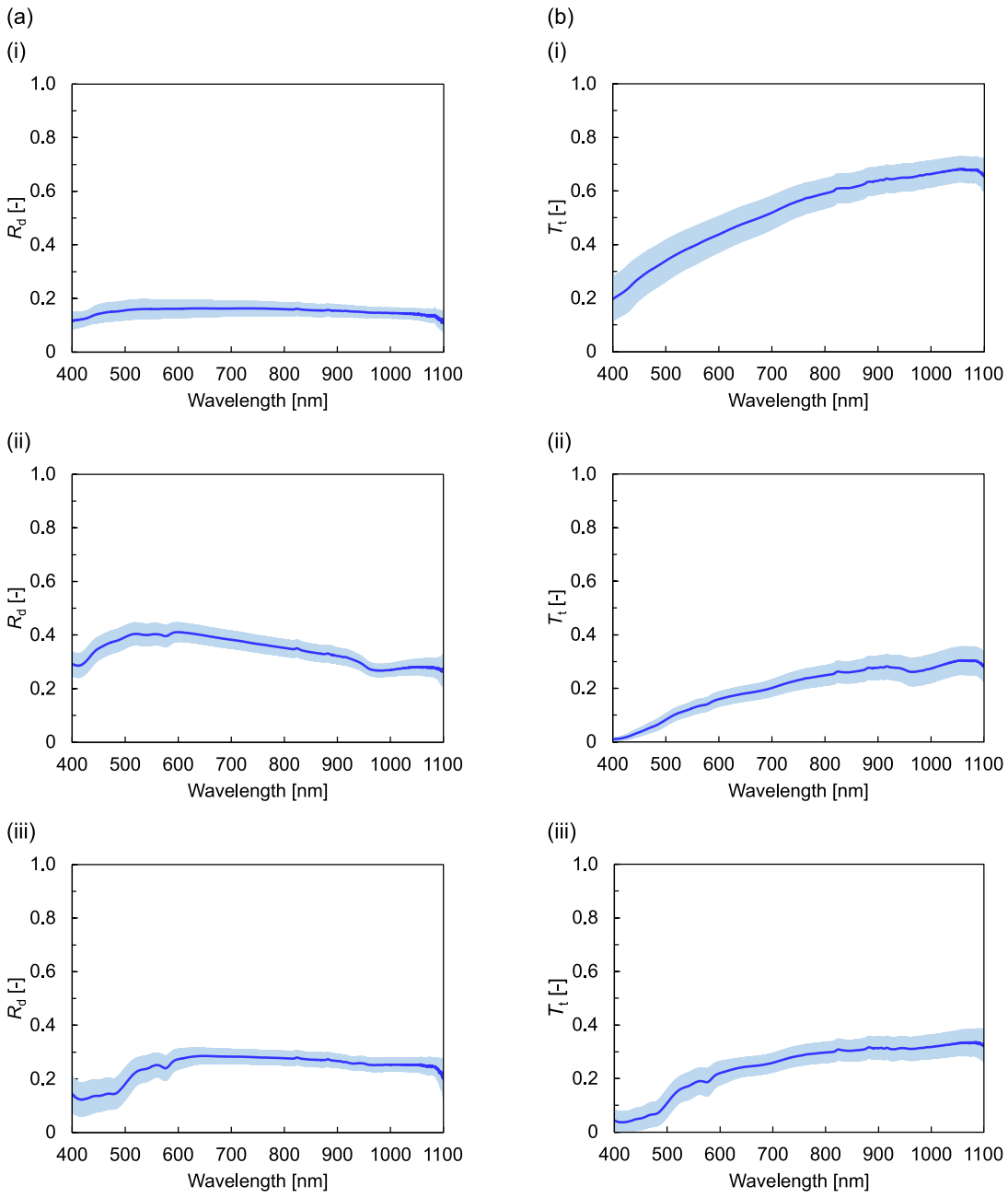


Figure 2.4: (a) Diffuse reflectance $R_d$ and (b) total transmittance $T_t$ spectra of (i) epidermis, (ii) dermis, and (iii) subcutaneous fat averaged over the 15, 20, and 20 samples, respectively. The shaded area represents the SD. Figure reproduced with permission from Ref. [21].

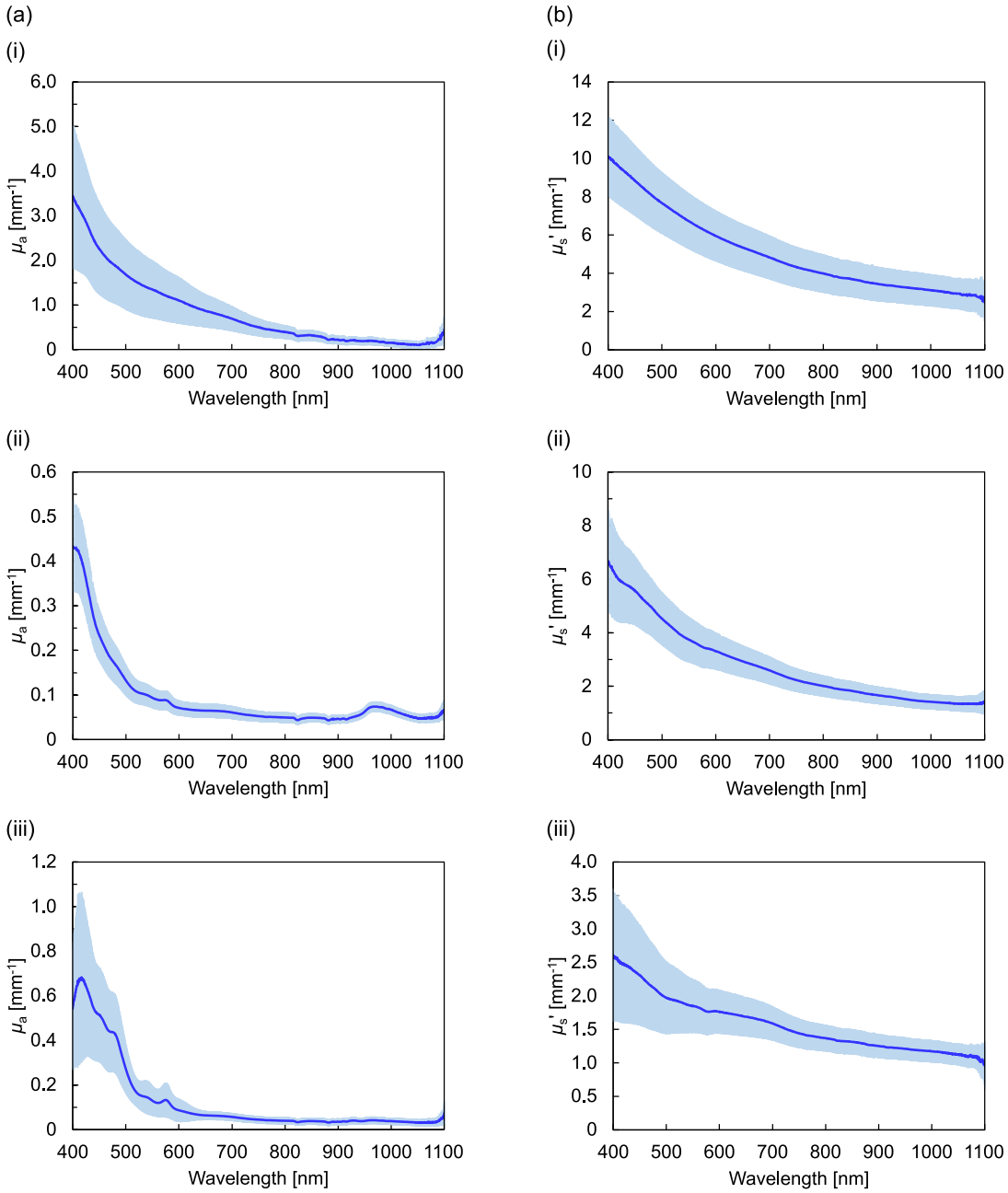


Figure 2.5: Wavelength dependences of (a) absorption coefficient $\mu_a$ and (b) reduced scattering coefficient $\mu_s'$ of (i) epidermis, (ii) dermis, and (iii) subcutaneous fat averaged over the 15, 20, and 20 samples, respectively. The shaded area represents the SD. Figure reproduced with permission from Ref. [21].

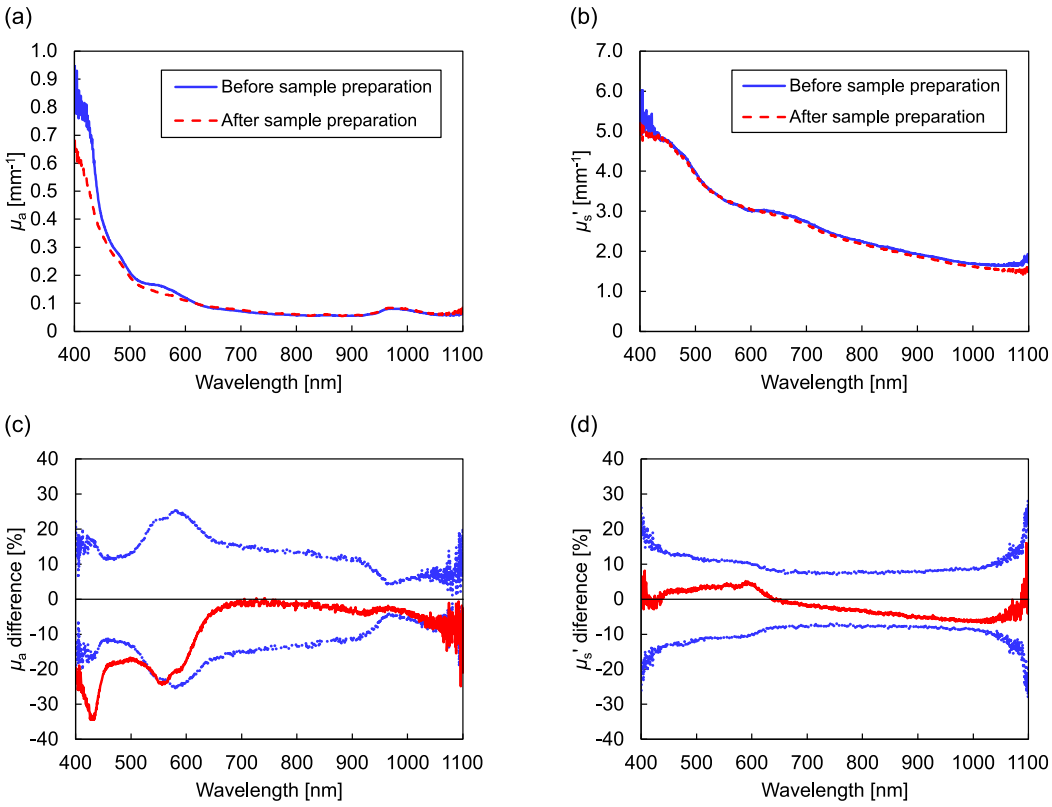


Figure 2.6: (a), (b) Wavelength dependences of absorption $\mu_a$ and reduced scattering $\mu_s'$ coefficients of epidermis + dermis before and after sample preparation. The solid and broken lines show the values before and after sample preparation, respectively. (c), (d) Wavelength dependences of the relative differences between the $\mu_a$ and $\mu_s'$ values of epidermis + dermis before and after the sample preparation. The solid line and dotted lines represent the relative differences in the $\mu_a$ and $\mu_s'$ values, and ±1SD, respectively. Figure reproduced with permission from Ref. [21].

sample preparation, as shown in Fig. 2.6(c); therefore, it was considered not significant. The difference in the $\mu_s'$ values was approximately ±10% throughout the wavelength range and showed a gradual increase with increasing wavelength. The difference was regarded as not significant. The SDs of both $\mu_a$ and $\mu_s'$ values increased from 1000 nm to 1100 nm due to the low detection sensitivity of the used setup in the NIR range.

### 2.3.3 Optical penetration depth and energy deposition

The $\delta$ and $S$ were calculated with a computational simulation based on the light transport model and the measured optical properties as shown in Table 2.3. The $\delta$ was defined as the depth at which the fluence inside the skin model falls to $1/e$ (36.8%) of the incident fluence. Figure 2.7(a) shows the $\delta$ at various wavelengths. To estimate the dispersion of $\delta$ in skin tissue, the maximum and minimum values of $\delta$ were calculated using the SDs of the $\mu_a$ and $\mu_s'$ values of each tissue layer. The maximum $\delta$ was obtained from the minimum $\mu_a$ and $\mu_s'$ values (mean − 1SD), while the minimum $\delta$ was obtained from the maximum $\mu_a$ and $\mu_s'$ values (mean + 1SD). The $\delta$ depended

Table 2.3: Absorption $\mu_a$ and reduced scattering $\mu_s'$ coefficients (mean ± 1SD) of Asian epidermis, dermis, and subcutaneous fat at typical wavelengths available for laser skin treatments. Table reproduced with permission from Ref. [21].

| Wavelength | Epidermis | | Dermis | | Subcutaneous fat | |
|---|---|---|---|---|---|---|
| [nm] | $\mu_a$ [mm$^{-1}$] | $\mu_s'$ [mm$^{-1}$] | $\mu_a$ [mm$^{-1}$] | $\mu_s'$ [mm$^{-1}$] | $\mu_a$ [mm$^{-1}$] | $\mu_s'$ [mm$^{-1}$] |
| 405 | 3.32 ± 1.51 | 9.95 ± 2.02 | 0.43 ± 0.10 | 6.46 ± 1.77 | 0.62 ± 0.34 | 2.56 ± 0.94 |
| 532 | 1.44 ± 0.69 | 7.04 ± 1.48 | 0.10 ± 0.03 | 3.96 ± 0.89 | 0.15 ± 0.07 | 1.89 ± 0.45 |
| 595 | 1.13 ± 0.53 | 6.02 ± 1.33 | 0.07 ± 0.02 | 3.35 ± 0.71 | 0.09 ± 0.05 | 1.77 ± 0.33 |
| 632 | 0.94 ± 0.41 | 5.55 ± 1.25 | 0.07 ± 0.02 | 3.06 ± 0.62 | 0.07 ± 0.03 | 1.72 ± 0.30 |
| 694 | 0.72 ± 0.29 | 4.89 ± 1.15 | 0.06 ± 0.02 | 2.64 ± 0.53 | 0.06 ± 0.02 | 1.60 ± 0.26 |
| 755 | 0.49 ± 0.19 | 4.28 ± 1.04 | 0.05 ± 0.01 | 2.20 ± 0.43 | 0.04 ± 0.02 | 1.43 ± 0.22 |
| 800 | 0.39 ± 0.15 | 3.98 ± 1.00 | 0.05 ± 0.01 | 2.01 ± 0.39 | 0.04 ± 0.02 | 1.37 ± 0.20 |
| 980 | 0.17 ± 0.09 | 3.17 ± 0.85 | 0.07 ± 0.01 | 1.45 ± 0.29 | 0.04 ± 0.02 | 1.18 ± 0.17 |
| 1064 | 0.13 ± 0.10 | 2.85 ± 0.86 | 0.05 ± 0.01 | 1.34 ± 0.29 | 0.03 ± 0.02 | 1.11 ± 0.16 |

on irradiation wavelength. At 405 and 532 nm, the light penetrated the upper dermis. At 595, 632, 694, 755, and 800 nm, the light penetrated the deep dermis. At 980 and 1064 nm, the light penetrated the subcutaneous fat. Figures 2.7(b)–(d) show the comparison of $\delta$ at the spot diameters of 2, 3, and 4 mm between the three types of skin. The $\delta$ increased with increasing spot diameter due to forward scattering by the skin tissue. Therefore, the required fluence can be reduced as the diameter of the spot increases [27]. The $\delta$ did not differ significantly between skin types when taking into account the dispersion of optical properties.

The $S$ was obtained by multiplying the fluence and the $\mu_a$ value of each tissue. Figure 2.8 shows the differences in skin type in the $S$ profiles along the depth $z$ axis at 500, 700, and 900 nm. The amount of light energy delivered to each tissue varied depending on wavelength. The peaks occurred in the epidermis and blood vessels owing to absorption by melanin and hemoglobin, respectively. The energy deposited in Caucasian subcutaneous fat was larger than that in Asian and African subcutaneous fats. The maximum $S$ at 500 nm appeared in the capillary blood vessels. The maximum $S$ in Asian skin was lower than in Caucasian skin tissue. At 700 nm, the maximum $S$ was observed in the epidermis. The maximum $S$ in Asian skin was two times higher than that in Caucasian skin and two times lower than that in African skin. At 900 nm, the maximum $S$ was found in the capillary blood vessels in Caucasian and Asian skins and the epidermis in African skin. The maximum $S$ in African epidermis was four times higher than in Asian epidermis.

## 2.4 Discussion

The validity of the optical properties of Asian epidermis, dermis, and subcutaneous fat was evaluated by comparison with the reported values of Caucasian and African skins. Figure 2.9(a) shows the comparison of the $\mu_a$ values of each layer in Asian skin with the reported values of Caucasian and African skins. The $\mu_a$ values of Asian epidermis were between those of Caucasian and African epidermises in the entire wavelength range because the darkly pigmented skin contains

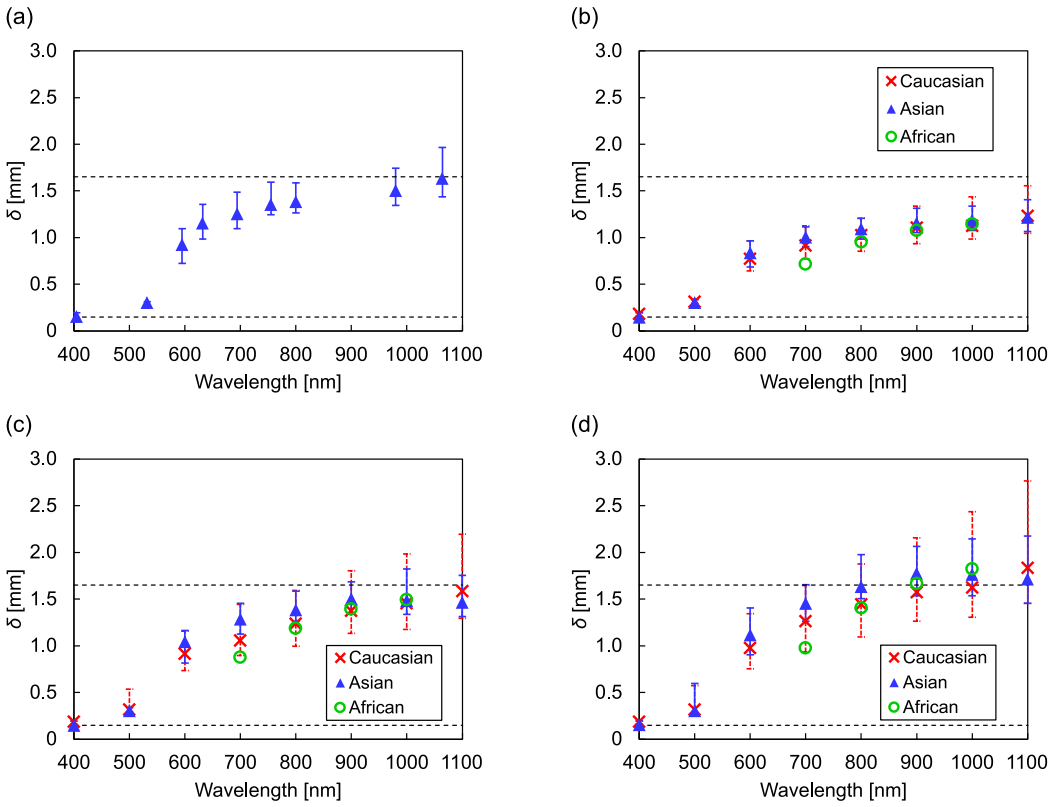


Figure 2.7: (a) Optical penetration depths $\delta$ at spot diameter of 3 mm and wavelengths currently available for clinical use in dermatology and plastic surgery. (b)–(d) Comparisons of $\delta$ at spot diameters of 2, 3, and 4 mm between the three skin types. The broken lines at 0.15 mm and 1.65 mm show the boundaries between the epidermis and the dermis, and between the dermis and the subcutaneous fat, respectively. Figure reproduced with permission from Ref. [21].

more melanin than the lightly pigmented skin [23]. These results were in good agreement with the *in vivo* study by Tseng *et al.* [7]. The $\mu_a$ values of Asian dermis and subcutaneous fat were comparable to the reported values in the wavelength range of more than 700 nm [4, 5]. In the shorter wavelength range, the $\mu_a$ values of Asian dermis were lower than the reported values. This seems to be caused by blood absorption. The *in vitro* $\mu_a$ values reported by Salomatina *et al.* [4] included blood absorption. On the other hand, the effect of blood in the dermis on the $\mu_a$ values obtained was almost eliminated because the specimens were soaked in a solution. In the *ex vivo* study by Simpson *et al.* [5], "dermis" indicated the tissues from the skin surface to the bottom of the dermis (including the epidermis). Therefore, the reported values included absorption by the epidermis. The $\mu_a$ values of Asian subcutaneous fat in the wavelength range shorter than 700 nm were lower than the $\mu_a$ values of Salomatina *et al.* [4] owing to the blood in the samples. Simpson *et al.* [5] also reported the $\mu_a$ values, which were lower than those measured in this experiment by half. They removed blood from their samples to exclude the influence of hemoglobin on the $\mu_a$ values.

Figure 2.9(b) shows the comparison of the $\mu_s'$ values of each layer in Asian skin with the

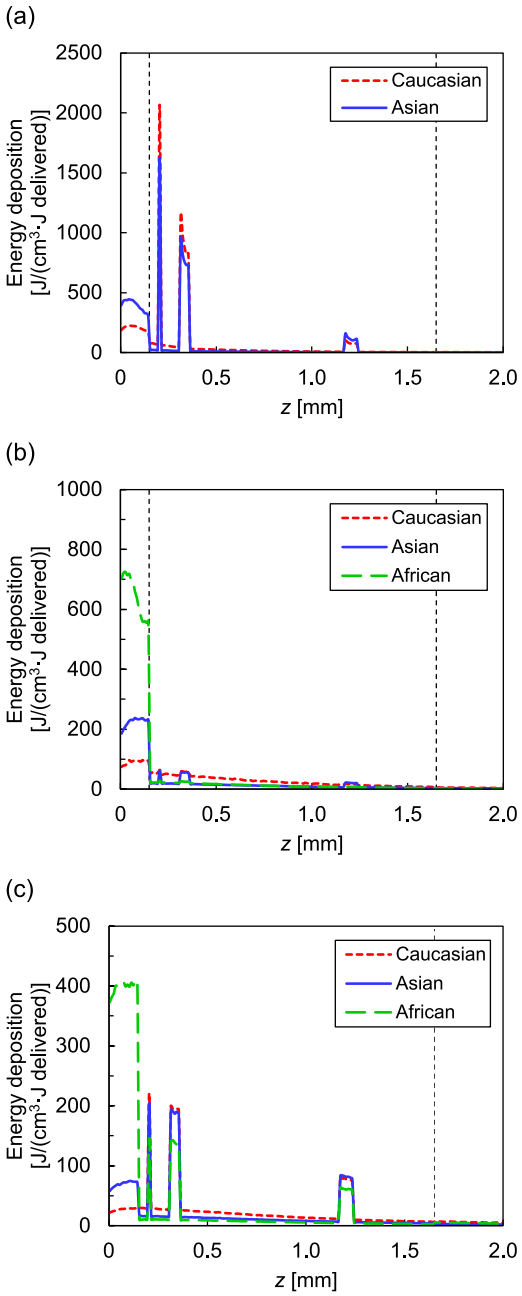


Figure 2.8: Differences in energy deposition $S$ profile on the $z$ axis ($x$ = $y$ = 0 mm) between different skin types at the wavelengths of (a) 500 nm, (b) 700 nm, and (c) 900 nm. The broken lines at 0.15 mm and 1.65 mm show the boundaries between the epidermis and the dermis, and between the dermis and the subcutaneous fat, respectively. Figure reproduced with permission from Ref. [21].

reported values of Caucasian and African skins. The $\mu_s'$ values of Asian epidermis and dermis were similar to the reported values in magnitude and slope across the entire wavelength range [4, 5]. The difference indicated that the epidermis and dermis of these groups have similar compositions in terms of average scatter size and density. The $\mu_s'$ values of Asian subcutaneous fat were lower than the values reported by Salomatina *et al.* [4] They attributed the increase in the scattering coefficient to the presence of connective tissue septa composed of thicker and denser collagen-elastin nets in subcutaneous fat samples obtained from the facial or scalp area. Compared with the *ex vivo* study by Simpson *et al.* [5], the $\mu_s'$ values were higher. This disagreement was likely related to unavoidable differences in the tissue sample storage and preparation procedure used. Their samples were refrigerated for five days and allowed to return to room temperature before being dissected.

In the iMC technique, the $g$ value was assumed as 0.9 for each type of tissue. So far, the measured $\mu_a$ and $\mu_s'$ values of each skin layer had the insensitivity to $g$ used for the iMC technique [5]. A small variation ($< 1\%$) was observed in the $\mu_s'$ values and negligible change in the $\mu_a$ values when the $g$ value was changed between 0.8 and 0.95 [5]. Figure 2.10 shows the $\mu_a$ and $\mu_s'$ values of the samples after sample preparation measured in Subsec. 2.3.2 using $g$ = 0.8, 0.9, and 0.95. The $\mu_a$ and $\mu_s'$ values obtained using the different $g$ values were almost the same, indicating that the measurement of $\mu_a$ and $\mu_s'$ values was insensitive to the $g$ value. The SDs of the $\mu_a$ and $\mu_s'$ derived from the individual and body-site differences of the samples were more dominant than the variations in the obtained $\mu_a$ ($< 2\%$) and $\mu_s'$ values ($< 1\%$) caused by changing $g$ values, respectively.

The effect of sample preparation on the $\mu_a$ values in the hemoglobin absorption band was significant. The volume fraction of blood after sample preparation was estimated to be 0.2% from the comparison of the $\mu_a$ values before and after sample preparation. The results were inconsistent with the reported value of 5.4% [16], which indicated that the absence of blood was mainly caused by immersion in solution during the delivery of the specimens. Roggan *et al.* postulated that storage of specimens in solution caused hemoglobin loss, resulting in considerable changes in the $\mu_a$ values [26]. The measured $\mu_a$ values were therefore regarded as bloodless parameters. To apply such parameters for clinical purposes, the $\mu_a$ values of blood must be considered to reproduce the actual *in vivo* situation.

The $\delta$ and $S$ in skin tissue have complemented the measurement data for various combinations of irradiation parameters that are difficult to obtain in preclinical and clinical experiments due to the technical challenges [10]. The differences in $\delta$ were not significant between skin types, while $\delta$ increased with increasing spot size. These results suggested that differences between skin types might have an insignificant effect on the depth of the treatment. In the $S$ calculation, the degree of peaks observed in the epidermis and blood vessels varied depending on wavelength and had significant differences between the skin types. The $S$ of the epidermis was affected by the difference in the $\mu_a$ values of the epidermis between the skin types. Because the $S$ distribution is a heat source in skin tissue, thermal damage to the skin can be calculated using the heat conduction equation [29]. The difference in damage to the epidermis and blood vessels between the skin types can

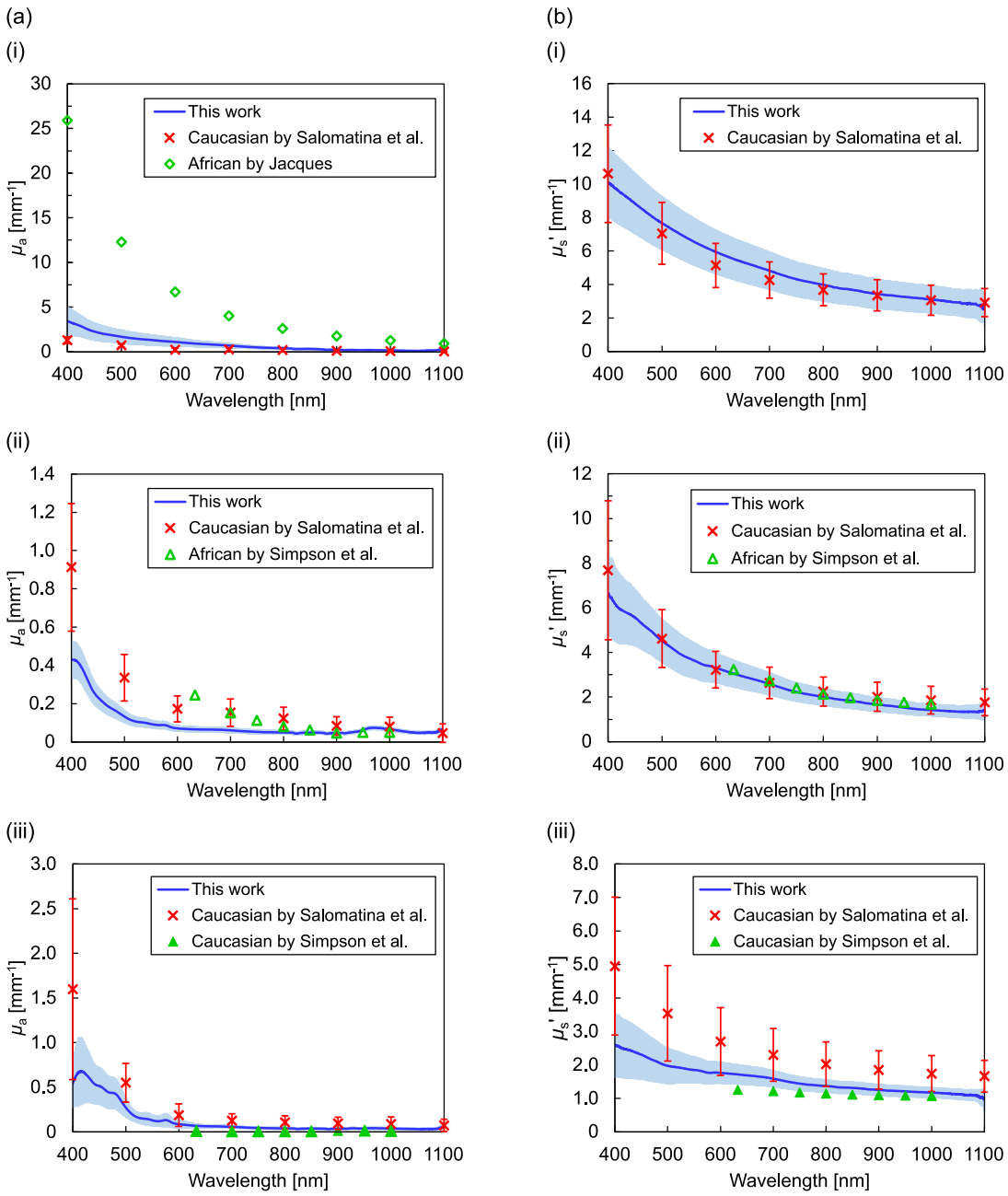


Figure 2.9: (a) Absorption $\mu_a$ and (b) reduced scattering $\mu_s'$ coefficients of (i) epidermis, (ii) dermis, and (iii) subcutaneous fat are compared with the reported values of Caucasian and African skins. The crosses correspond to Caucasian epidermis, dermis, and subcutaneous fat [4]. The open diamonds correspond to African epidermis [28]. The open and closed triangles correspond to African dermis and Caucasian subcutaneous fat, respectively [5]. The error bars represent the SD of the reported values. Figure reproduced with permission from Ref. [21].

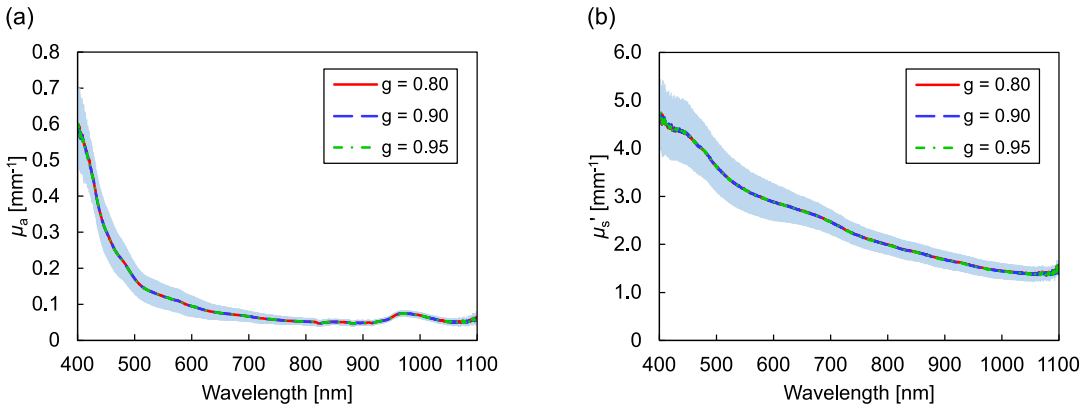


Figure 2.10: Wavelength dependences of (a) absorption $\mu_a$ and (b) reduced scattering $\mu_s'$ coefficients of epidermis + dermis for $g$ = 0.80 (red), 0.90 (blue), and 0.95 (green). The shaded area represents the SD for $g$ = 0.90. Figure reproduced with permission from Ref. [21].

affect the treatment outcome. This analysis leads to the evaluation of the risk of complications such as burning, dyspigmentation, and scarring [30]. These results demonstrated that computational simulations with the measured optical properties can provide detailed and quantitative evaluation of picosecond laser propagation in skin tissue depending on the irradiation parameters and skin type.

The measured skin samples were obtained from a variety of body sites, ages, and sexes. This may have introduced variations to the $\mu_a$ and $\mu_s'$ spectra. Furthermore, the thickness of each skin layer varies individually and site-dependently [31]. The accumulation of sufficient knowledge of these differences will allow the construction of virtual human skin models for various sites and will improve their clinical applicability. Using these skin models in combination with light transport models will improve the precision of computational simulations for laser skin treatment.

## 2.5 Conclusion of this chapter

The optical properties of Asian epidermis, dermis, and subcutaneous fat were measured in the 400–1100 nm wavelength range with the DIS spectrophotometer and iMC technique. The $\mu_a$ values of Asian epidermis differed markedly from those of Caucasian and African epidermises, while the $\mu_s'$ values of each layer in Asian skin were similar to those of the other types of skin. Computational simulations using a layered skin model and the measured optical properties analyzed $\delta$ and $S$ in skin tissue. The $\delta$ and $S$ complemented the measurement data for various combinations of irradiation parameters that were difficult to obtain in preclinical and clinical experiments. The computational simulations allow for the light propagation analysis in each Asian skin layer for computational laser treatment using picosecond laser.

# References


[1] S.L. Jacques. Optical properties of biological tissues: A review. *Physics in Medicine & Biology*, 58(11):R37–R61, 2013.

[2] S. Flock, M. Patterson, B. Wilson, and D. Wyman. Monte Carlo modeling of light propagation in highly scattering tissues. I. Model predictions and comparison with diffusion theory. *IEEE Transactions on Biomedical Engineering*, 36(12):1162–1168, 1989.

[3] I. Meglinski and S. Matcher. Computer simulation of the skin reflectance spectra. *Computer Methods and Programs in Biomedicine*, 70(2):179–186, 2003.

[4] E.V. Salomatina, B. Jiang, J. Novak, and A.N. Yaroslavsky. Optical properties of normal and cancerous human skin in the visible and near-infrared spectral range. *Journal of Biomedical Optics*, 11(6):064026, 2006.

[5] C.R. Simpson, M. Kohl, M. Essenpreis, and M. Cope. Near-infrared optical properties of *ex vivo* human skin and subcutaneous tissues measured using the Monte Carlo inversion technique. *Physics in Medicine & Biology*, 43(9):2465, 1998.

[6] H. Jonasson, I. Fredriksson, S. Bergstrand, C.J. Östgren, M. Larsson, and T. Strömberg. *In vivo* characterization of light scattering properties of human skin in the 475-to 850-nm wavelength range in a Swedish cohort. *Journal of Biomedical Optics*, 23(12):121608, 2018.

[7] S.H. Tseng, A. Grant, and A.J. Durkin. *In vivo* determination of skin near-infrared optical properties using diffuse optical spectroscopy. *Journal of Biomedical Optics*, 13(1):014016, 2008.

[8] N. Verdel, J. Tanevski, S. Džeroski, and B. Majaron. Predictive model for the quantitative analysis of human skin using photothermal radiometry and diffuse reflectance spectroscopy. *Biomedical Optics Express*, 11(3):1679–1696, 2020.

[9] S.Y. Tsui, C.Y. Wang, T.H. Huang, and K.B. Sung. Modelling spatially-resolved diffuse reflectance spectra of a multi-layered skin model by artificial neural networks trained with Monte Carlo simulations. *Biomedical Optics Express*, 9(4):1531–1544, 2018.

[10] A. Izumoto, T. Nishimura, H. Hazama, N. Ikeda, Y. Kajimoto, and K. Awazu. Singlet oxygen model evaluation of interstitial photodynamic therapy with 5-aminolevulinic acid for malignant brain tumor. *Journal of Biomedical Optics*, 25(6):063803, 2019.

[11] L. Sevilha-Santos, A. Dos Santos Júnior, V. Medeiros-Silva, J. Bergmann, and others. Accuracy of qPCR for quantifying Leishmania kDNA in different skin layers of patients with American tegumentary leishmaniasis. *Clinical Microbiology and Infection*, 25(2):242–247, 2019.

[12] N. Honda, K. Ishii, Y. Kajimoto, T. Kuroiwa, and K. Awazu. Determination of optical properties of human brain tumor tissues from 350 to 1000 nm to investigate the cause of false negatives in fluorescence-guided resection with 5-aminolevulinic acid. *Journal of Biomedical Optics*, 23(7):075006, 2018.

[13] A.N. Bashkatov, E.A. Genina, and V.V. Tuchin. Optical properties of skin, subcutaneous, and muscle tissues: A review. *Journal of Innovative Optical Health Sciences*, 4(1):9–38, 2011.

[14] L. Wang, S.L. Jacques, and L. Zheng. MCML—Monte Carlo modeling of light transport in multi-layered tissues. *Computer Methods and Programs in Biomedicine*, 47(2):131–146, 1995.

[15] V.V. Tuchin. *Tissue Optics: Light Scattering Methods and Instruments for Medical Diagnosis*. SPIE, Bellingham, WA, USA, 2007.

[16] I.V. Meglinski and S.J. Matcher. Quantitative assessment of skin layers absorption and skin reflectance spectra simulation in the visible and near-infrared spectral regions. *Physiological Measurement*, 23(4):741–753, 2002.

[17] S.L. Jacques. Coupling 3D Monte Carlo light transport in optically heterogeneous tissues to photoacoustic signal generation. *Photoacoustics*, 2(4):137–142, 2014.

[18] S. Prahl. Optical absorption of hemoglobin. *Oregon Medical Laser Center*, 1999.

[19] G. Alexandrakis, F.R. Rannou, and A.F. Chatziioannou. Tomographic bioluminescence imaging by use of a combined optical-PET (OPET) system: A computer simulation feasibility study. *Physics in Medicine & Biology*, 50(17):4225, 2005.

[20] N. Bosschaart, G.J. Edelman, M.C. Aalders, van T.G. Leeuwen, and D.J. Faber. A literature review and novel theoretical approach on the optical properties of whole blood. *Lasers in Medical Science*, 29(2):453–479, 2014.

[21] Y. Shimojo, T. Nishimura, H. Hazama, T. Ozawa, and K. Awazu. Measurement of absorption and reduced scattering coefficients in Asian human epidermis, dermis, and subcutaneous fat tissues in the 400- to 1100-nm wavelength range for optical penetration depth and energy deposition analysis. *Journal of Biomedical Optics*, 25(4):045002, 2020.

[22] R.R. Anderson and J.A. Parrish. The optics of human skin. *Journal of Investigative Dermatology*, 77(1):13–19, 1981.

[23] S. Alaluf, D. Atkins, K. Barrett, M. Blount, N. Carter, and A. Heath. Ethnic variation in melanin content and composition in photoexposed and photoprotected human skin. *Pigment Cell Research*, 15(2):112–118, 2002.

[24] A. Yaroslavsky, P. Schulze, I. Yaroslavsky, R. Schober, F. Ulrich, and H. Schwarzmaier. Optical properties of selected native and coagulated human brain tissues *in vitro* in the visible and near infrared spectral range. *Physics in Medicine & Biology*, 47(12):2059, 2002.

[25] E.K. Chan, B. Sorg, D. Protsenko, M. O'Neil, M. Motamedi, and A.J. Welch. Effects of compression on soft tissue optical properties. *IEEE Journal of Selected Topics in Quantum Electronics*, 2(4):943–950, 1996.

[26] A. Roggan, D. Schädel, U. Netz, J.P. Ritz, C.T. Germer, and G. Müller. The effect of preparation technique on the optical parameters of biological tissue. *Applied Physics B*, 69(5):445–453, 1999.

[27] C. Ash, M. Dubec, K. Donne, and T. Bashford. Effect of wavelength and beam width on penetration in light-tissue interaction using computational methods. *Lasers in Medical Science*, 32(8):1909–1918, 2017.

[28] S.L. Jacques. Skin optics summary. *Oregon Medical Laser Center News*, 1998.

[29] Y. Shimojo, T. Nishimura, H. Hazama, I. Nobuhisa, and K. Awazu. *In silico* evaluation of thermal skin damage caused by picosecond laser irradiation. *Bio-Optics: Design and Application*, pages DS1A–7, 2019.

[30] A. Alexis. Lasers and light-based therapies in ethnic skin: Treatment options and recommendations for Fitzpatrick skin types IV and VI. *British Journal of Dermatology*, 169:91–97, 2013.

[31] Y. Lee and K. Hwang. Skin thickness of Korean adults. *Surgical and Radiologic Anatomy*, 24(3):183–189, 2002.

# Chapter 3

# Determination of threshold fluences for melanosome disruption

## 3.1 Introduction

Studies performed in Chapter 2 have measured the optical properties of Asian epidermis, dermis, and subcutaneous fat as a tissue-scale analysis of picosecond laser-skin interactions. Computational simulations with these parameters have provided light distributions in the skin for various irradiation parameters. In the removal of pigmented lesions with picosecond laser, the treatment effect is achieved by selective disruption of melanosome structures through the absorption of local fluence [1]. For effective treatment, the local fluence at the target should be greater than the threshold for melanosome disruption while at the same time, the local fluence in normal tissue should be minimal. A threshold-based analysis can provide numerical indices for setting the irradiation parameters in computational laser treatment.

Threshold fluences for selective melanosome responses with short-pulsed laser of various widths have been measured [2–6]. The threshold fluences of femtosecond-to-microsecond lasers for melanosome disruption in laser skin treatment have been reported [7, 8]. These studies visually observed the disruption through the immediate whitening of the skin surface from increased optical scattering. The fluences obtained were affected by optical attenuation in the skin before reaching the target melanosomes. Melanosome disruption from the net threshold fluences was thus not shown. Experimental analyses of picosecond-to-microsecond lasers for selective retina treatment have also been performed using melanosomes isolated from porcine and bovine eyes [2–6]. However, these analyses investigated the threshold fluences for microbubble formation around melanosomes to overstretch the RPE cell membrane [9]. These reported values are not applicable to melanosome disruption. A detailed investigation of melanosome disruption by picosecond laser is required to design a treatment protocol that maximizes the treatment outcome.

---

Portions of this chapter were originally published under the titles,"Incident fluence analysis for 755-nm picosecond laser treatment of pigmented skin lesions based on threshold fluences for melanosome disruption" by Yu Shimojo, Takahiro Nishimura, Hisanao Hazama, Nobuhisa Ito, and Kunio Awazu in *Lasers in Surgery and Medicine* 53(8):1096–1104 (2021) and "Experimental analysis of morphological change in melanin for multiscale modeling of picosecond laser skin treatment" by Yu Shimojo, Takahiro Nishimura, Hisanao Hazama, and Kunio Awazu in *Proceedings of SPIE* 11640, Optical Interactions with Tissue and Cells XXXII; 1164005 (2021).

Here, this chapter presents experimental analyses of picosecond laser-melanosome interactions to determine the threshold fluences for melanosome disruption. The mean particle sizes of melanosomes irradiated with picosecond laser for different fluences are measured by DLS, and their morphological changes are confirmed by SEM. From the relationships between the irradiated fluences and the mean particle sizes, the threshold fluences are determined. Furthermore, because melanosome disruption is triggered by optical absorption by the internal melanin, the effect of melanin on picosecond laser-melanosome interactions is investigated. These experimental analyses will help to create a mathematical model for computational laser treatment based on the picosecond laser-melanosome interactions.

## 3.2 Materials and Methods

### 3.2.1 Sample preparation

Melanosomes isolated from the RPE of fresh porcine eyes (purchased from Tokyo Shibaura Zouki, Japan) were prepared as alternative samples for human cutaneous melanosomes [2]. They were dissected, and the lens and vitreous were removed. Subsequently, they were briefly immersed in distilled water, and the neural retina was peeled off. The RPE cells were extracted using a toothbrush and suspended in distilled water. The suspensions were purified using a glass microfiber filter with a 2.7-$\mu$m pore size (1823-090, Whatman, UK) to collect melanosomes released from RPE cells. Distilled water was added to the purified suspensions such that the samples had an optical density of approximately 0.05 at a wavelength of 755 nm when the sample thickness was 1 cm, thus providing laser energy from the sample surface to the bottom. Because no aggregation of the melanosomes was observed using an inverted laboratory microscope (Leica DM IRB, Leica, Germany), the effects of the interaction between the individual melanosomes were discounted. The samples were stored at 4°C until use.

Synthetic melanin powder produced by oxidation of tyrosine with hydro peroxide (M8631, Sigma-Aldrich, USA) was used to prepare melanin samples. Melanin powder was mixed with distilled water at a ratio of 1 mg melanin to 1 mL distilled water. This mixture was ultrasonicated for 15 minutes to disperse the melanin powder and centrifuged at 10,000 rpm for 10 minutes. The decanted melanin suspension was filtered with a 0.22-$\mu$m pore size polyvinylidene fluoride membrane (SLGVR33RS, Merck Millipore, Germany) to remove large insoluble aggregates. The filtered melanin suspension was homogeneous [10].

### 3.2.2 Laser system and irradiation setup

A 755-nm picosecond alexandrite laser device for therapeutic use (PicoSure, Cynosure, USA) was employed. Table 3.1 shows the irradiation parameters. The irradiation parameters were based on the nominal values specified in the system operation manual (PicoSure Operator Manual). Various fluences were used to determine the thresholds. The fluence was dependent on the spot size; the larger the spot size, the lower the fluence, *e.g.*, 2.0 mm at 5.25 J/cm$^2$ for 550 ps. The variance

in the measured fluence over an incident beam obtained from the beam profile data was within the range of −20% to +30% from the average value. The samples that were to be irradiated were added to Petri dishes at a height of 1 cm (179830, Thermo Fisher Scientific, USA), under which a sheet of black flocked paper (BFP1, Thorlabs, USA) was placed to prevent backscattering. The tip of the handpiece was fixed on the sample surface to maintain a constant distance between the surface and the irradiation port. The laser pulse was irradiated with a beam divergence (full angle) of 11–77 mrad. The optical axis was adjusted to be perpendicular to the sample surface. During the irradiation, the sample was moved with a motorized linear translation stage (SGSP20-20(XY), Sigmakoki, Japan) at a speed of the spot size per second in such a way that the entire surface was irradiated without overlapping the already irradiated areas. The temperature of the samples was maintained at 37°C during irradiation using a digital temperature controller (TS-P, As One, Japan) and a silicon rubber heater (SAM0310, Sakaguchi E.H VOC, Japan).

Table 3.1: Irradiation parameters of picosecond alexandrite laser based on the nominal values specified on the PicoSure Operator Manual. Table reproduced with permission from Ref. [11].

| | Picosecond alexandrite laser | |
|---|---|---|
| Wavelength [nm] | 755 | |
| Pulse width [ps] | 550 | 750 |
| Spot size [mm] | 2.0, 2.6, 2.8, 2.9, 3.0, 3.1, 3.2, 3.6 4.0, 4.4, 4.8 | 2.2, 2.6, 2.8, 2.9, 3.0, 3.1, 3.2, 3.3, 3.4, 3.5, 3.6, 4.0, 5.0 |
| Fluence [J/cm$^2$] | 0.91, 1.09, 1.31, 1.62, 2.04, 2.19, 2.33, 2.50, 2.68, 3.11, 5.25 | 1.02, 1.59, 1.96, 2.08, 2.20, 2.34, 2.49, 2.65, 2.83, 3.03, 3.25, 3.77, 5.26 |
| Repetition rate [Hz] | 1 | |
| Output stability of fluence [%] | ±20 | |
| Variance of spot size [%] | ±10 | |

### 3.2.3 Measurement of mean particle sizes of melanosomes and melanins

Melanosome disruption was measured by comparing the mean particle sizes of unirradiated melanosomes and melanosomes irradiated with picosecond laser to determine the threshold. The particle size measurements were performed using DLS (Zetasizer Nano ZS, Malvern, UK), incorporating noninvasive backscatter optics. This technique measures the time-dependent fluctuations in the intensity of scattered light that occur from Brownian motion [12]. The measurement results do not depend on the number of particles [13]. The irradiated samples were placed in disposable cells (BRA759116, As One) with an optical path length of 10 mm. The refractive indices of melanosomes and distilled water were 1.65 and 1.33, respectively [14]. Each sample was measured three times and the values were averaged. For melanin samples, the same experimental protocol was used to measure the mean particle size. Laser irradiated the melanin samples at a wavelength of 755 nm, a pulse width of 550 ps, and a fluence of 5.25 J/cm$^2$.

### 3.2.4 Morphological observation of melanosomes and melanins

Unirradiated melanosomes and melanins, and melanosomes and melanins irradiated with picosecond laser were observed by SEM (JCM-5700, JEOL, Japan) to confirm their morphological change. Laser irradiation was applied at a wavelength of 755 nm, a pulse width of 550 ps, and a fluence of 5.25 J/cm$^2$ because it was inferred that melanosomes could be disrupted and clearly observed under this irradiation condition from Fig. 3.1. The melanosomes and melanins were dried and coated with platinum to a thickness of 5 nm using an ion sputtering system (E-1010, Hitachi, Japan) to increase the electrical conductivity. For melanosome samples, the long axis was measured using ImageJ (NIH, USA).

### 3.2.5 Transmittance measurement of melanins

The transmittance of the melanin samples used in the particle size measurements was measured with a spectrophotometer (U3500, Hitachi, Japan) to evaluate their optical properties. The picosecond laser was irradiated with the same condition as for the DLS analysis and SEM observation.

### 3.2.6 Statistical analysis

A two-tailed unpaired Student's *t*-test determined a significant difference in the mean particle sizes between unirradiated samples and samples irradiated with picosecond laser. The probability value of $P < 0.01$ indicated statistical significance.

## 3.3 Results

### 3.3.1 Threshold fluences for melanosome disruption

The mean particle sizes of unirradiated melanosomes and melanosomes irradiated with picosecond laser were statistically compared to determine the threshold fluences for melanosome disruption. Figure 3.1 shows the mean particle sizes of melanosomes exposed to 550- and 750-ps laser pulses with varying fluence. The mean particle sizes decreased with increasing irradiated fluence. The mean particle sizes of unirradiated melanosomes in Fig. 3.1(a) were slightly larger than those in Fig. 3.1(b) owing to the individual differences. Statistical comparison indicated that the mean particle sizes significantly changed when 550- and 750-ps laser pulses were irradiated at or above 2.19 and 2.49 J/cm$^2$, respectively. The morphologies of unirradiated melanosomes and melanosomes irradiated with picosecond laser were then observed with SEM to confirm melanosome disruption when the mean particle sizes changed significantly (Fig. 3.2). Although the unirradiated melanosomes retained their native shape (Fig. 3.2(i)), the smooth surface structures were broken in the irradiated melanosomes (Fig. 3.2(ii)). The lengths of the unirradiated and irradiated melanosomes were $1.6 \pm 0.3$ and 1.3 $\mu$m, respectively, and the sizes of the disrupted melanosomes decreased, showing consistency with the results of the DLS analysis. Therefore, the DLS analysis and SEM observation resulted in determining the threshold fluences for melanosome disruption as 2.19 and 2.49 J/cm$^2$ for 550- and 750-ps laser pulses, respectively.

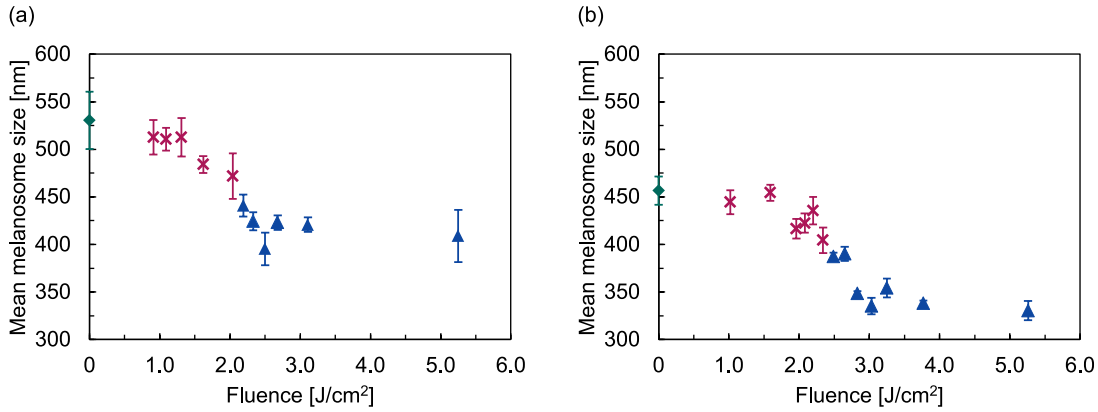


Figure 3.1: Mean particle sizes of melanosomes irradiated with (a) 550- and (b) 750-ps laser pulses with varying fluences ($n = 3$). The error bars represent the SD. The differences in the mean particle sizes between irradiated (crosses and triangles) and unirradiated (diamonds) melanosomes were statistically evaluated. Despite no significant differences in the crosses, there are significant differences in the triangles ($P < 0.01$). The threshold fluences of 550- and 750-ps laser pulses disrupting the melanosomes were determined as 2.19 and 2.49 J/cm$^2$, respectively. Figure reproduced with permission from Ref. [11].

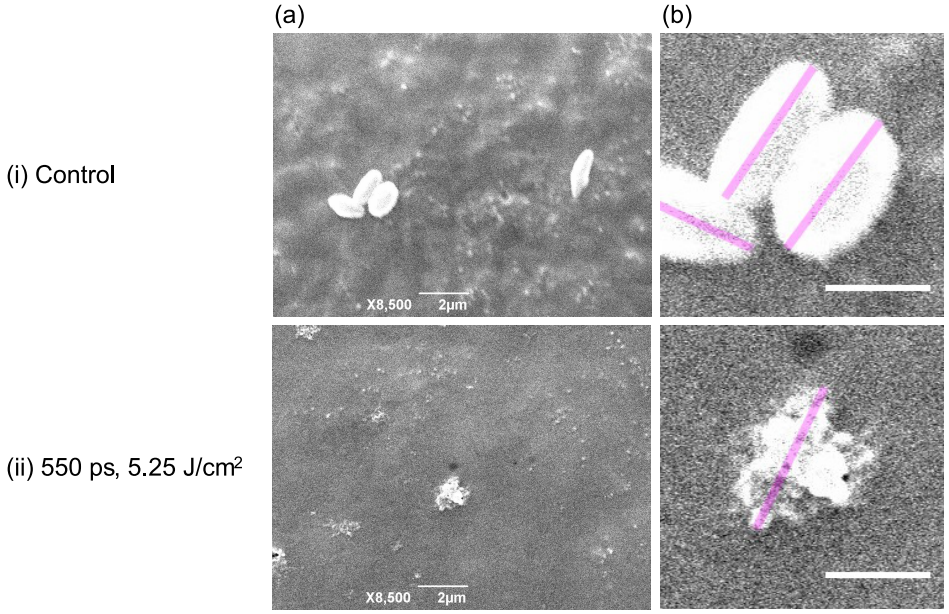


Figure 3.2: (a) Melanosome disruption was confirmed by comparing scanning electron micrographs between (i) unirradiated melanosomes and (ii) melanosomes irradiated with picosecond laser. The picosecond laser was irradiated at a wavelength of 755 nm, pulse width of 550 ps, and fluence of 5.25 J/cm$^2$. (b) The melanosomes were shown with greater magnification. The long axes of the melanosomes shown as the pink lines were measured using the ImageJ. The scale bars in (a) and (b) show 2 and 1 $\mu$m, respectively. Figure reproduced with permission from Ref. [11].

### 3.3.2 Change in morphological characteristics of melanins

The unirradiated melanins and melanins irradiated with picosecond laser were analyzed by DLS and SEM to confirm the morphological change caused by picosecond laser irradiation. Figure 3.3 shows the mean particle sizes of unirradiated melanins and melanins exposed to 550-ps laser pulses with a fluence of 5.25 J/cm$^2$ measured by DLS. Although the mean particle size of irradiated melanins slightly decreased, the statistical comparison indicated that the mean particle sizes did not change significantly between unirradiated and irradiated melanins. Figure 3.4 shows the scanning electron micrographs of unirradiated melanins and melanins exposed to 550-ps laser pulses with a fluence of 5.25 J/cm$^2$. The melanins appeared to be formed by aggregates. The unirradiated melanins retained their smooth surface structures (Fig. 3.4(a)) while the irradiated melanins still retained the native structures (Fig. 3.4(b)).

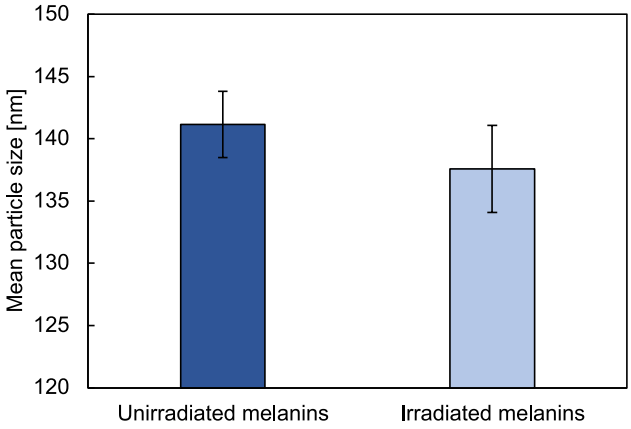


Figure 3.3: Mean particle sizes of unirradiated melanins and melanins irradiated with picosecond laser. The picosecond laser was irradiated at a wavelength of 755 nm, pulse width of 550 ps, and fluence of 5.25 J/cm$^2$. The error bars represent the SD. Statistical comparison of the mean particle sizes between unirradiated and irradiated melanins indicated no significant difference. Figure reproduced with permission from Ref. [15].

### 3.3.3 Change in optical properties of melanins

Figure 3.5 shows the transmittances of unirradiated melanins and melanins irradiated with picosecond laser. There was almost no transmittance change in the samples. This result showed that melanins did not change their optical properties by picosecond laser.

## 3.4 Discussion

The threshold fluences of 550- and 750-ps laser pulses were determined by evaluating the relationships between the irradiated fluences and the mean particle sizes measured by DLS and confirming the melanosome disruption when the mean particle sizes changed significantly by SEM. The decrease in the sizes of the disrupted melanosomes resulting from the DLS analysis was consistent

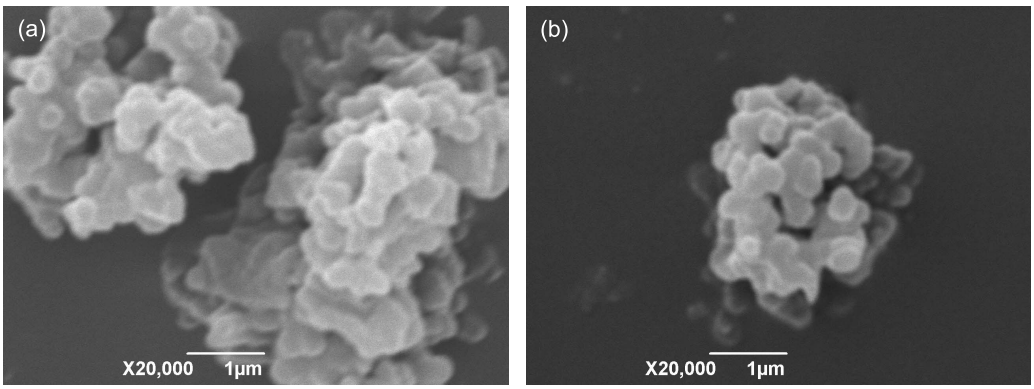


Figure 3.4: Morphologies of (a) unirradiated melanins and (b) melanins irradiated with picosecond laser. The picosecond laser was irradiated at a wavelength of 755 nm, pulse width of 550 ps, and fluence of 5.25 J/cm$^2$. The scale bars show 1 $\mu$m. Figure reproduced with permission from Ref. [15].

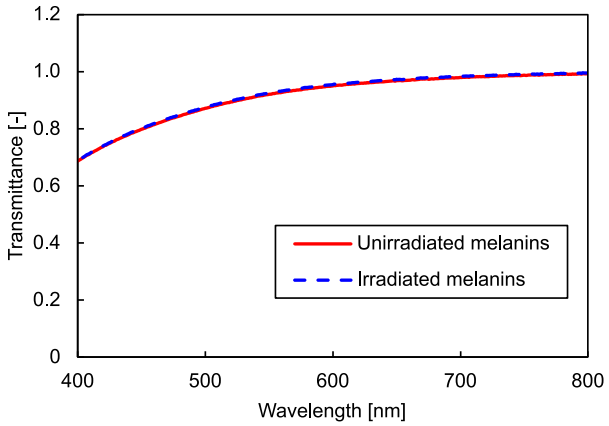


Figure 3.5: Transmittances of unirradiated melanins and melanins irradiated with picosecond laser. The picosecond laser was irradiated at a wavelength of 755 nm, pulse width of 550 ps, and fluence of 5.25 J/cm$^2$.

with the results of the SEM observation. Almost no difference was found between the threshold fluences because both laser pulses satisfy the thermal confinement condition of melanosomes. Because the output stability of fluence was ±20%, the threshold fluences may vary within this range. The effect of the difference in the size of unirradiated melanosomes on the thresholds was negligible (Fig. 3.3). This is because the laser pulses satisfy the thermal confinement condition regardless of individual differences. In Fig. 3.3, there was almost no variation in the mean particle sizes of melanosomes irradiated above the threshold fluences. When the mean particle sizes irradiated at or above the thresholds were compared with those irradiated with the maximum fluences (5.25 and 5.26 J/cm$^2$ for 550- and 750-ps laser pulses, respectively), the differences were not significant for irradiations above 2.19 and 2.83 J/cm$^2$ for 550- and 750-ps laser pulses, respectively. This comparison suggested that irradiation at a fluence higher than the thresholds had little effect on melanosome disruption.

The threshold fluences obtained were one order of magnitude greater than the values of 532-nm nanosecond laser for transient microbubble formation on a melanosome surface for selective retina treatment [2, 6]. Neumann and Brinkmann [2] observed no threshold hysteresis during repeated irradiations, nor morphological changes in melanosomes by optical microscopy after irradiation at or near the threshold. In contrast, the experiments in this chapter used a different laser wavelength of 755 nm and determined the threshold fluences for the different selective responses, *i.e.*, melanosome disruption. These differences could cause a variance between the values obtained and those previously reported. Glickman *et al.* [16] predicted the threshold fluence for melanosome disruption to be 153.6 mJ/cm$^2$ when a 10-ns laser pulse at a wavelength of 532 nm was irradiated approximately 1800 times at 10 Hz. The determined threshold fluences were greater than the reported value because they were the fluence required to disrupt melanosomes with a single pulse rather than multiple pulses.

The temperature rise necessary for explosive vaporization is reasonably similar between porcine RPE melanosomes (136 ± 23°C) [2] and human cutaneous melanosomes (112 ± 7°C) [7], and is calculated from the irradiated fluence and absorption coefficient of melanosomes. The absorption coefficient of porcine RPE melanosomes was reported to be larger than that of human cutaneous melanosomes [2, 7], which might affect the threshold fluences. Herein, picosecond laser irradiated the melanosomes suspended in distilled water. From a thermal perspective, the interaction between the melanosomes and their surroundings was similar to the actual skin because there is little difference in thermal diffusivity between water and skin [2, 17].

The DLS analysis and SEM observation of melanins found that the morphological characteristics of melanins irradiated with picosecond laser were not significantly changed. The transmittance measurement also indicated that the optical properties of melanins irradiated with picosecond laser were not significantly altered. These results suggested that melanins do not change their optical structures and are involved as a heat source in picosecond laser treatment of pigmented lesions. In the investigation of the melanosome response to picosecond laser, the smooth surface structures were broken in melanosomes irradiated by 550-ps laser pulses with a fluence of 5.25 J/cm$^2$. Thermal diffusion from melanins that absorb picosecond laser energy might disrupt the lipid bilayer membranes within melanosomes. The verification using melanin from animal models will be necessary to extrapolate the results to studies of human epidermal melanin.

The melanin aggregates were on the order of 1 $\mu$m (Fig. 3.4), while the mean particle sizes of melanins resulting from the DLS analysis were about 140 nm (Fig. 3.3). The DLS analysis measured the melanin suspensions while the SEM observation dried the suspensions. During the drying, the melanin aggregates were formed. This did not affect the results of the comparison to evaluate the effect of picosecond laser on the morphologies. This investigation used synthetic melanin for irradiation samples. The epidermis has been reported to contain melanin with diameters of 30 to 159 nm [18, 19]. The mean particle size of the unirradiated melanins was within the range of the diameter of epidermal melanin. The absorption coefficient of synthetic melanin was reported to be on the order of magnitude the same as that of natural melanin at the irradiation wavelength [20]. The energy deposition in the melanin samples was similar to that in natural melanin.

The obtained threshold fluences help to predict the incident fluences necessary for computational laser treatment using picosecond laser. Irradiated fluence is attenuated by the skin. This optical attenuation can be calculated using a light transport model with the optical properties measured in Chapter 2. Creating a mathematical model that combines the threshold and the light transport model enables a calculation of incident fluences required for the local fluence at the target to be over the threshold, leading to the design of numerical indices for setting the irradiation parameters in computational laser treatment.

## 3.5 Conclusion of this chapter

The DLS analysis and SEM observation confirmed that the threshold fluences were 2.19 and 2.49 J/cm$^2$ for 550- and 750-ps laser pulses, respectively, while there was almost no change in the morphological and optical characteristics of melanins irradiated with picosecond laser. The results suggested that melanin is involved as a heat source to damage melanosomes in picosecond laser treatment of pigmented lesions. These fundamental findings related to picosecond laser-melanosome interactions will allow for the construction of a mathematical model to provide numerical indices for setting the irradiation parameters in computational laser treatment.

## References


[1] H.C. Lee, J. Childs, H.J. Chung, J. Park, J. Hong, and S.B. Cho. Pattern analysis of 532-and 1,064-nm picosecond-domain laser-induced immediate tissue reactions in *ex vivo* pigmented micropig skin. *Scientific Reports*, 9(1):1–10, 2019.

[2] J. Neumann and R. Brinkmann. Boiling nucleation on melanosomes and microbeads transiently heated by nanosecond and microsecond laser pulses. *Journal of Biomedical Optics*, 10(2):024001, 2005.

[3] H. Lee, C. Alt, C.M. Pitsillides, and C.P. Lin. Optical detection of intracellular cavitation during selective laser targeting of the retinal pigment epithelium: Dependence of cell death mechanism on pulse duration. *Journal of Biomedical Optics*, 12(6):064034, 2007.

[4] M.S. Schmidt, P.K. Kennedy, R.L. Vincelette, M.L. Denton, G.D. Noojin, K.J. Schuster, R.J. Thomas, and B.A. Rockwell. Trends in melanosome microcavitation thresholds for nanosecond pulse exposures in the near infrared. *Journal of Biomedical Optics*, 19(3):035003, 2014.

[5] M.S. Schmidt, P.K. Kennedy, G.D. Noojin, R.J. Thomas, and B.A. Rockwell. Temperature dependence of nanosecond laser pulse thresholds of melanosome and microsphere microcavitation. *Journal of Biomedical Optics*, 21(1):015013, 2016.

[6] P. Deladurantaye, S. Méthot, O. Mermut, P. Galarneau, and P.J. Rochette. Potential of submicrosecond laser pulse shaping for controlling microcavitation in selective retinal therapies. *Biomedical Optics Express*, 11(1):109–132, 2020.

[7] S.L. Jacques and D.J. McAuliffe. The melanosome: Threshold temperature for explosive vaporization and internal absorption coefficient during pulsed laser irradiation. *Photochemistry and Photobiology*, 53(6):769–775, 1991.

[8] S. Watanabe, R.R. Anderson, S. Brorson, G. Dalickas, J.G. Fujimoto, and T.J. Flotte. Comparative studies of femtosecond to microsecond laser pulses on selective pigmented cell injury in skin. *Photochemistry and Photobiology*, 53(6):757–762, 1991.

[9] M. Luecking, R. Brinkmann, S. Ramos, W. Stork, and N. Heussner. Capabilities and limitations of a new thermal finite volume model for the evaluation of laser-induced thermomechanical retinal damage. *Computers in Biology and Medicine*, 122:103835, 2020.

[10] G. Perna, M.C. Frassanito, G. Palazzo, A. Gallone, A. Mallardi, P. Biagi, and V. Capozzi. Fluorescence spectroscopy of synthetic melanin in solution. *Journal of Luminescence*, 129(1):44–49, 2009.

[11] Y. Shimojo, T. Nishimura, H. Hazama, N. Ito, and K. Awazu. Incident fluence analysis for 755-nm picosecond laser treatment of pigmented skin lesions based on threshold fluences for melanosome disruption. *Lasers in Surgery and Medicine*, 53(8):1096–1104, 2021.

[12] M. Wasilewska, Z. Adamczyk, and B. Jachimska. Structure of fibrinogen in electrolyte solutions derived from dynamic light scattering (DLS) and viscosity measurements. *Langmuir*, 25(6):3698–3704, 2009.

[13] J. Stetefeld, S.A. McKenna, and T.R. Patel. Dynamic light scattering: A practical guide and applications in biomedical sciences. *Biophysical Reviews*, 8(4):409–427, 2016.

[14] W. Song, L. Zhang, S. Ness, and J. Yi. Wavelength-dependent optical properties of melanosomes in retinal pigmented epithelium and their changes with melanin bleaching: A numerical study. *Biomedical Optics Express*, 8(9):3966–3980, 2017.

[15] Y. Shimojo, T. Nishimura, H. Hazama, and K. Awazu. Experimental analysis of morphological change in melanin for multiscale modeling of picosecond laser skin treatment. *Proceedings of SPIE*, 11640:9–14, 2021.

[16] R.D. Glickman, S.L. Jacques, J.A. Schwartz, T. Rodriguez, K.W. Lam, and G. Buhr. Photodisruption increases the free-radical reactivity of melanosomes isolated from retinal pigment epithelium. *Proceedings of SPIE*, 2681:460–467, 1996.

[17] F.A. Duck. Thermal Properties of Tissue. In *Physical Properties of Tissues*, pages 9–42. Academic Press, London, UK, 1990.

[18] N. Kollias, R.M. Sayre, L. Zeise, and M.R. Chedekel. New trends in photobiology: Photoprotection by melanin. *Journal of Photochemistry and Photobiology B: Biology*, 9(2):135–160, 1991.

[19] A.N. Bashkatov, E.A. Genina, V.I. Kochubey, M.M. Stolnitz, T.A. Bashkatova, O.V. Novikova, A.Y. Peshkova, and V.V. Tuchin. Optical properties of melanin in the skin and skin-like phantoms. *Proceedings of SPIE*, 4162:219–226, 2000.

[20] V. Capozzi, G. Perna, P. Carmone, A. Gallone, M. Lastella, E. Mezzenga, G. Quartucci, M. Ambrico, V. Augelli, P. Biagi, and others. Optical and photoelectronic properties of melanin. *Thin Solid Films*, 511:362–366, 2006.

# Chapter 4

# Nonlinear absorption-based analysis of energy deposition in melanosomes

## 4.1 Introduction

A detailed evaluation of irradiation parameters, including fluence, wavelength, and pulse width, is essential to provide safe and efficacious laser treatment. Studies performed in Chapter 3 have obtained threshold fluences for melanosome disruption with picosecond laser, and have discussed that the threshold can be used for a mathematical model for evaluating incident fluences in computational laser treatment. Laser wavelengths have been chosen based on the spatial distribution of pigmented lesions and the difference in absorption between melanin and hemoglobin; 755 and 1064 nm are commonly used for deep lesions and 532 nm for upper lesions [1–3]. The appropriate pulse width for treatment has been determined based on the thermal and stress confinement conditions of melanosomes [4, 5]. Since the speed of light propagation is much faster than the speed of thermal diffusion or stress propagation, the light distribution is calculated approximating the temporal pulse profile as a delta-like function [6]. This model is therefore not applicable to evaluating the effect of different pulse widths that satisfy the thermal and stress confinement conditions on the light distribution. Analysis of the effect of different short pulse widths on energy deposition in melanosomes is needed.

Melanosomes deposit laser energy through optical absorption by the internal melanin. This underlying process for treatment has been analyzed based on linear absorption of local fluence [7–9]. However, laser pulses with picosecond to nanosecond widths are absorbed by melanin in a nonlinear manner owing to their high power density [10, 11]. The influence of nonlinear absorption by melanin on the treatment effect becomes more pronounced with increasing power density. Since the power density changes as the pulse width changes, a quantitative evaluation of the energy deposition considering nonlinear absorption allows for a comparative evaluation of treatment with different short-pulsed lasers.

Nonlinear absorption by melanin has been investigated using laser pulses at various wave-

This chapter was submitted under the title, "Nonlinear absorption-based analysis of energy deposition in melanosomes for 532-nm short-pulsed laser skin treatment" by Yu Shimojo, Takahiro Nishimura, Toshiyuki Ozawa, Daisuke Tsuruta, and Kunio Awazu to *Lasers in Surgery and Medicine*.

lengths [11–14]. Fluorescence of melanin excited by resonant NIR two-photon absorption has been detected [15, 16]. The measurements have indicated that a high power density causes nonlinear absorption by melanin based on sequential two-photon absorption, and a nonlinear absorption process of melanin can be modeled as sequential two-photon absorption. For the nonlinear absorption-based analysis of energy deposition, absorption cross-sections and nonradiative lifetimes of melanin are required. In pump-probe spectroscopies in the UV and NIR ranges, the nonradiative relaxation dynamics of melanin have been measured [13, 14]. However, the physical parameters in the VIS range, which is available for short-pulsed laser treatment, are still lacking. Furthermore, the relationships between the nonradiative pathways and lifetimes have not been revealed. The relationships and parameters allow for the calculation of nonlinear absorption coefficients of melanin based on the electron population dynamics of each energy level. A detailed investigation of nonlinear absorption by melanin in the VIS range is required to evaluate the safety and efficacy of short-pulsed laser treatment in terms of energy deposition in melanosomes.

In this chapter, a nonlinear absorption-based analysis of energy deposition in melanosomes for 532-nm short-pulsed laser treatment of pigmented lesions is presented. Energy deposition is obtained from the accumulation of absorbed energy in melanosomes during a laser pulse, and thus, the nonlinear absorption behavior of melanin in response to power density is modeled. The absorption cross-sections and nonradiative lifetimes of melanin are determined from transmittance measurement. The energy deposition in melanosomes is calculated with varying fluences and pulse widths, including actual clinical parameters. As the effect of nonlinear absorption by melanin on melanosome disruption increases with increasing power density, it is hypothesized that the analysis shows that picosecond lasers deliver optical energy to melanosomes more efficiently than nanosecond lasers. The computational analysis will allow a computational laser treatment to establish numerical indices for setting appropriate pulse widths and to evaluate the safety and efficacy of short-pulsed laser treatment.

## 4.2 Materials and methods

### 4.2.1 Nonlinear absorption model of melanin

Nonlinear absorption by melanin for 532-nm laser irradiation is described based on sequential two-photon absorption consisting of the singlet ground ($S_0$), first excited ($S_1$), and second excited states ($S_2$) [13]. Figure 4.1 shows the simplified Jablonski diagram of the nonlinear absorption by melanin. A two-photon absorption process occurs via a real intermediate state in the singlet state because melanin exhibits linear absorption over the UV–NIR range [13, 16]. Therefore, the nonlinear absorption model simulates excitation between the singlet ground and first excited states, excitation between the singlet first and second excited states, and nonradiative decays. The nonlinear absorption model assumes that the absorbed photon energy is released nonradiatively owing to the low radiative quantum yield [17]. At an extremely high-power density, LIOB via multiphoton absorption can occur. The power density of interest is lower than the threshold of $10^{13}$ W/cm$^2$ [10]. The nonlinear absorption model assumes that LIOB is negligible. The rate equations

describing the nonlinear absorption model can be written as follows:

$$\begin{cases} \dfrac{\mathrm{d}n_{\mathrm{S}_0}(t)}{\mathrm{d}t} = -W_{01}n_{\mathrm{S}_0}(t) + \dfrac{1}{\tau_1}n_{\mathrm{S}_1}(t) \\ \dfrac{\mathrm{d}n_{\mathrm{S}_1}(t)}{\mathrm{d}t} = W_{01}n_{\mathrm{S}_0}(t) - \left(W_{12} + \dfrac{1}{\tau_1}\right)n_{\mathrm{S}_1}(t) + \dfrac{1}{\tau_2}n_{\mathrm{S}_2}(t) \ , \\ \dfrac{\mathrm{d}n_{\mathrm{S}_2}(t)}{\mathrm{d}t} = W_{12}n_{\mathrm{S}_1}(t) - \dfrac{1}{\tau_2}n_{\mathrm{S}_2}(t) \end{cases} \tag{4.1}$$

where $n_{\mathrm{S}_0}(t)$, $n_{\mathrm{S}_1}(t)$, and $n_{\mathrm{S}_2}(t)$ are the time-dependent populations of each electron state. $n_{\mathrm{S}_0}(t)$, $n_{\mathrm{S}_1}(t)$, and $n_{\mathrm{S}_2}(t)$ satisfy a boundary condition provided by population normalization $n_{\mathrm{S}_0}(t) + n_{\mathrm{S}_1}(t) + n_{\mathrm{S}_2}(t) = 1$, and the initial condition $n_{\mathrm{S}_0}(0) = 1$. $W_{01}$ and $W_{12}$ are the transition probabilities in the singlet ground and excited states, respectively. $\tau_i$ $(i = 1, 2)$ are the nonradiative lifetimes of melanin. The transition probabilities are defined as $\phi\sigma_{01}$ and $\phi\sigma_{12}$, respectively, where $\phi$ is the irradiated photon density, $I/h\nu$, with $I$ as the intensity of the irradiated laser pulse, $\sigma_{01}$ and $\sigma_{12}$ are the one-photon absorption cross-section for the first and second absorption steps, respectively. When a laser pulse is irradiated to melanin, the population of the $\mathrm{S}_0$ state is excited to the $\mathrm{S}_1$ state in proportion to the power density of the laser pulse, to the absorption cross-section, and to the initial population of the $\mathrm{S}_0$ state. A population fraction of the $\mathrm{S}_1$ state is excited to the $\mathrm{S}_2$ state, and the excited population relaxes back to the $\mathrm{S}_1$ state with a nonradiative lifetime, $\tau_2$. The other fraction of the $\mathrm{S}_1$ state relaxes back to the $\mathrm{S}_0$ state with a nonradiative lifetime, $\tau_1$.

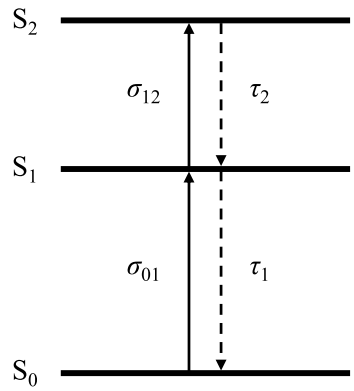


Figure 4.1: Nonlinear absorption model of melanin based on sequential two-photon absorption. The solid arrows show the electron transition in the first and second absorption steps, and the dashed arrows show the nonradiative decays.

### 4.2.2 Sample preparation

Synthetic melanin (M8631, Sigma-Aldrich, USA) was dissolved in PBS and DMSO solutions to prepare the two types of melanin samples. For the PBS-based samples, melanin was mixed at a ratio of 6 mg melanin to 10 mL PBS solution (163-25265, FUJIFILM Wako Pure Chemical Corporation, Japan). The mixture was ultrasonicated for 30 minutes to disperse the melanin and

centrifuged at 4,000 rpm for 30 minutes. The melanin suspension was decanted to remove the large insoluble aggregates. For the DMSO-based samples, melanin was dissolved in DMSO solution (D4540, Sigma-Aldrich) at a concentration of 0.03 mg/mL and ultrasonicated for 15 minutes. The samples were placed in a quartz cell (S15-UV-2, GL Sciences, Japan) with a thickness of 2 mm for transmittance measurements. The two prepared melanin solutions were homogeneous, and light scattering in the samples was neglected because the concentration was so low that the Lambert's law could be applied to transmittance measurements [18].

### 4.2.3 Absorption spectroscopy

The linear dependence of melanin absorption was evaluated with absorption spectroscopy. The absorbance of the melanin samples was measured using a spectrophotometer (U3500, Hitachi, Japan). From the measured spectra, the transmittances through linear absorption were obtained, and compared with those calculated in Sec. 4.2.6.

### 4.2.4 Experimental setup for laser power density-dependent transmittance measurement

Figure 4.2 shows the experimental setup for the measurement of the laser power density-dependent transmittance. A 532-nm pulsed laser (LS-2131M-10, Lotis TII, Belarus), which produces 6-ns pulses at a repetition rate of 10 Hz, was used. The output stability was 0.9%. The pulse width was evaluated by the FWHM of the pulse shape, which was measured with a silicon detector (818-BB-21, Newport, USA) and a digital oscilloscope (TDS3054C, Tektronix, USA). Since nonlinear absorption depends on power density, the transmittances at various power densities were measured by varying the pulse energy with the same pulse width. The laser beam was directed through a half-wave plate (WPMH10M-532, Thorlabs, USA), a polarization beam splitter (PBS12-532-HP, Thorlabs), and neutral-density filters (NEK01, Thorlabs) to control the pulse energy. The laser beam reflected off the polarization beam splitter was blocked by a beam trap (BT610, Thorlabs). The transmitted laser beam was reflected off two mirrors (NB1-K13, Thorlabs) and guided to a sample. The laser beam was then focused by a plano-convex lens (LA1509-A, Thorlabs) onto a sample. The focus beam area was $9.4 \times 10^{-3}$ mm$^2$. The Rayleigh length was 2.2 mm, which was smaller than the sample thickness. The laser beam in the focal region could be approximated as a parallel beam. The input and transmitted laser pulse energies were measured with an energy meter (PE-25C, Ophir Optronics, Israel) in the far field after collimating the laser beam with a plano-convex lens (LA1509-A, Thorlabs).

### 4.2.5 Measurement of laser power density-dependent transmittance

The laser power density-dependent transmittance of the melanin samples was measured in order to obtain the absorption cross-sections and nonradiative lifetimes of melanin. The values were obtained as the ratio of the laser energy transmitted through the melanin sample to the laser energy transmitted through the blank sample. Each laser energy was measured for a single shot, and the

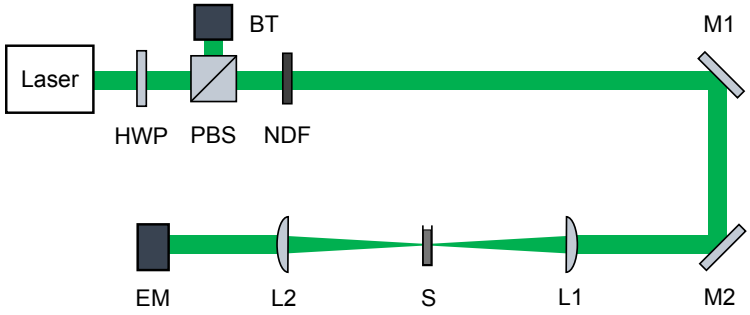


Figure 4.2: Experimental setup for laser power-dependent transmittance measurement. BT, beam trap; EM, energy meter; HWP, half-wave plate; L1, L2, plano-convex lens (f = 100 mm); M1, M2, mirror; NDF, neutral-density filter; PBS, polarization beam splitter; S, sample.

power density was evaluated by dividing the pulse energy by the spot area and the pulse width. The input laser energy was adjusted from approximately 10 $\mu$J to 1.4 mJ so that the input power density was in the range of approximately 0.01–1 GW/cm$^2$, which included the range of clinical parameters [19–21]. The sample was inserted into a cuvette holder (CVH100/M, Thorlabs) along with an outside spacer (CM-2, GL Sciences) and placed at the focus. The melanin sample was stirred for every measurement to avoid heat accumulation and degradation owing to laser irradiation. The measurement was performed three times. The amount of energy transmitted through the blank samples was measured before every measurement to ensure that it was kept within the set power density range. LIOB was not observed in the samples because the transmittance did not decrease rapidly or bubbles were not generated [11].

### 4.2.6 Determination of absorption cross-sections and nonradiative lifetimes

The absorption cross-sections and nonradiative lifetimes were determined by fitting the transmittances calculated with the nonlinear absorption model to the transmittances measured for various power densities with a nonlinear least-squares algorithm. The transmittance was calculated as the ratio of the fluence transmitted through the sample to the input fluence. Each fluence was obtained by integrating the measured temporal profile of the pulse power density.

$$T = \frac{\int_{-\infty}^{\infty} I(t,l)\mathrm{d}t}{\int_{-\infty}^{\infty} I(t,0)\mathrm{d}t}, \tag{4.2}$$

where $I(t,l)$ is the laser intensity transmitted through a sample with a thickness of $l$ and $I(t,0)$ is the input intensity. The input intensity is attenuated by sequential two-photon absorption while penetrating the sample, and the attenuation takes the form

$$\frac{\mathrm{d}I(t,z)}{\mathrm{d}z} = -N_0(\sigma_{01}n_{\mathrm{S}_0}(t,z) + \sigma_{12}n_{\mathrm{S}_1}(t,z))I(t,z), \tag{4.3}$$

where $N_0$ is the number of melanins per unit volume and $n_{\mathrm{S}_0}(t,z)$ and $n_{\mathrm{S}_1}(t,z)$ are obtained from Equation 4.1. $N_0(\sigma_{01}n_{\mathrm{S}_0}(t,z)+\sigma_{12}n_{\mathrm{S}_1}(t,z))$ is the nonlinear absorption coefficient of the melanin

sample. $N_0$ is usually determined from $N_0 = a/(N_A M)$, where $a$ is the concentration of melanin, $M$ is the molecular weight, and $N_A$ is the Avogadro number. However, the molecular weight of melanin is difficult to determine because of its inherent diversity and complex chemical structure [22]. The concentration of melanin dissolved in PBS solution could not be determined because the insoluble aggregate was removed. $N_0$ was determined by fitting, as well as the absorption cross-sections and nonradiative lifetimes, and it was validated by comparing the transmittance calculated by $T = \exp(-N_0\sigma_{01}l)$ and that measured by absorption spectroscopy. The fitting was controlled by MATLAB (2022a, MathWorks, USA), and Equations 4.1 and 4.3 were solved with the Runge-Kuta method. The accuracy of the fit was evaluated using Pearson's $\chi^2$ test statistic at a significance level of 5%.

### 4.2.7 Open-aperture $z$-scan measurement

The number of photons involved in nonlinear absorption by melanin was estimated to confirm that the sequential two-photon absorption process is valid for the nonlinear absorption mechanism of melanin at a wavelength of 532 nm [23]. For the estimation, the $z$-scan profile of the transmittance of melanin dissolved in PBS solution was measured using an open-aperture $z$-scan technique [24]. For the $z$-scan measurement, the experimental setup shown in Fig. 4.2 was modified to move the sample manually along a dovetail optical rail (RLA075/M, Thorlabs). As in Sec. 4.2.5, the sample was stirred at each measurement position to avoid heat accumulation and degeneration by laser irradiation. The measurement was performed three times. The measured $z$-scan profile was compared with the profile calculated using the theoretical formula of normalized transmittance through $n$-photon absorption [25]:

$$T_{\mathrm{nPA}} = \frac{1}{\left[1 + \beta_n L_{\mathrm{eff}} \left(\frac{I_0}{1 + (z/z_0)^2}\right)^{n-1}\right]^{\frac{1}{n-1}}}, \tag{4.4}$$

where $\beta_n$ is the effective $n$-photon absorption coefficient, which is related to the multiple absorption coefficient [26, 27]; $L_{\mathrm{eff}}$ is the effective thickness of the sample ($L_{\mathrm{eff}} = (1-\exp(-(n-1)\alpha l))/((n-1)\alpha)$, where $\alpha$ and $l$ are the one-photon absorption coefficient and the thickness of the sample, respectively); $I_0$ is the input power density at the focus (0.98 GW/cm$^2$); and $z_0$ is the Rayleigh length. $\alpha$ was obtained from the average of the transmittances measured at the three points from the minimum and maximum sample positions, and $\beta_n$ was determined by fitting the calculated data with the measured data for $n = 2, 3$.

### 4.2.8 Energy deposition analysis of melanosomes

The energy deposition in a melanosome during a single laser pulse was calculated with varying fluence and pulse width. The melanosome was assumed to be a spherical object of melanin aggregation with a diameter of 1 $\mu$m [28]. Scattering of the incident laser pulse by the adjacent tissue components was neglected because it was assumed that the melanosome absorbed the laser

light in the same way as a melanosome in water [29]. The effect of surface reflection was also neglected [11]. The energy deposition was calculated by integrating the energy deposition rate in a melanosome during laser pulse irradiation as follows:

$$E = \int_{-\infty}^{\infty} \int_{V} \mu_{\mathrm{a}}(t, \mathbf{r}) I(t, \mathbf{r}) \mathrm{d}V \mathrm{d}t, \tag{4.5}$$

where $\mu_{\mathrm{a}}(t, \mathbf{r})$ is the nonlinear absorption coefficient of melanosomes ($\mathbf{r}$ shows the position inside the melanosome); $I$ is the fluence rate with a Gaussian temporal pulse profile; and $V$ is the volume of a melanosome. The nonlinear absorption coefficient of melanosomes was defined as $N_0(\sigma_{01} n_{\mathrm{S}_0}(t, \mathbf{r}) + \sigma_{12} n_{\mathrm{S}_1}(t, \mathbf{r}))$, and calculated with the physical parameters obtained from the PBS-solution melanin samples. $N_0$ is the density of melanins inside a melanosome, defined as $N_0 = \alpha/\sigma_{01}$, where $\alpha$ is the one-photon absorption coefficient of melanosomes [30]. The laser pulse irradiation was simulated under the conditions of 532 nm wavelength, 100 ps–100 ns pulse widths, 0.25–1.75 J/cm$^2$ fluences with an increment of 0.25 J/cm$^2$, and a single shot. The incident power densities calculated by dividing the fluence by the pulse width were lower than the highest density used in the transmittance measurement. Additionally, a computational analysis of clinical parameters was performed to comparatively evaluate the safety and efficacy of short-pulsed laser treatment. The irradiation parameters were those used in clinical studies comparing 532-nm picosecond and nanosecond laser treatments of epidermal pigmented lesions [19–21, 31]. The energy deposition was calculated with and without taking into account nonlinear absorption by melanin. The energy depositions obtained were compared with the threshold value for explosive vaporization of melanosomes, which was calculated from

$$E_{\mathrm{th}} = \rho c V \Delta T, \tag{4.6}$$

where $\rho$ (1.41 g/cm$^3$) is the density [32], $c$ (2.55 J/(g·K)) is the specific heat [32], and $\Delta T$ (approximately 100 K) is the temperature rise for explosive vaporization of melanosomes [33, 34].

## 4.3 Results

### 4.3.1 Laser power density-dependent transmittance

The absorbance of the melanin samples was measured to calculate the transmittance through linear absorption. Figure 4.3 shows the absorbances of melanin dissolved in PBS and DMSO solutions. Both absorbances decreased monotonically with increasing wavelength. The transmittances of melanin dissolved in PBS and DMSO solutions at a wavelength of 532 nm were calculated as 92.7% and 80.8%, respectively, from the relationship of $T = 10^{-A}$, where $A$ is the absorbance. Figure 4.4 shows the measured laser power density-dependent transmittances of melanin dissolved in PBS and the DMSO solutions and fitted data. The transmittances were almost constant at a low power density ($< 50$ MW/cm$^2$), showing a linear dependence of the absorption by melanin. On the other hand, as the power density increased, the transmittances decreased dramatically, showing a nonlinear dependence of the absorption by melanin. The $\chi^2$ test statistic did not indicate

significant differences between the measured and fitted data ($\chi^2$ = 0.02 and 0.01 for the PBS- and DMSO-solution melanin samples, respectively). The fitting curves showed good agreement with the measured transmittances for both PBS- and DMSO-solution melanin samples.

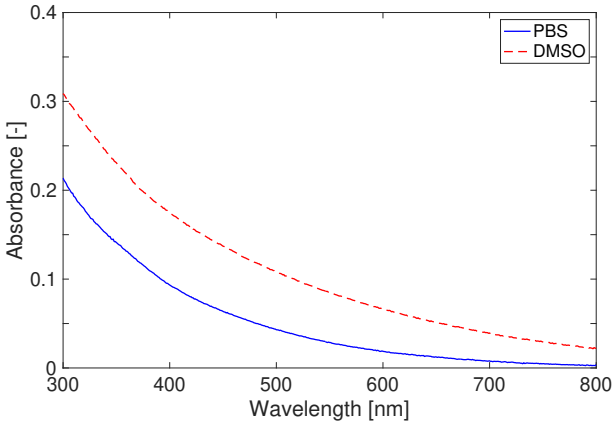


Figure 4.3: Absorbances of melanin dissolved in PBS and DMSO solutions in the wavelength range of 300–800 nm. The blue solid and red dashed lines show the measured data for PBS- and DMSO-based samples, respectively.

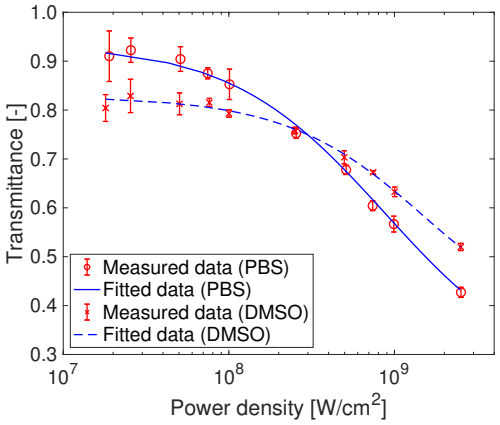


Figure 4.4: Laser power density-dependent transmittances of melanin dissolved in PBS and DMSO solutions. The red circles and crosses show the measured data with the SD for PBS- and DMSO-based samples, respectively. The blue solid and dashed curves show the fitted data obtained from the nonlinear absorption model for PBS- and DMSO-based samples, respectively. The laser irradiation parameters were 532 nm for wavelength, 18 MW/cm$^2$ to 2.5 GW/cm$^2$ for power density at the focus, and a single shot.

### 4.3.2 Absorption cross-sections and nonradiative lifetimes

Table 4.1 shows the resulting parameters of the absorption cross-sections and nonradiative lifetimes. $N_0$ was determined as $(2 \pm 1) \times 10^{17}$ and $(5 \pm 1) \times 10^{17}$ 1/cm$^3$ for PBS- and DMSO-solution

melanin samples, respectively. The obtained $\sigma_{01}$ values were of the same magnitude as the literature value of $5 \times 10^{-18}$ cm$^2$ at a wavelength of 800 nm [15]. The obtained $\sigma_{12}$ values were within the reported values of the typical orders of $10^{-17}$–$10^{-16}$ cm$^2$ for an absorption cross-section for the second absorption step [35]. The determined nonradiative lifetimes had picosecond and subnanosecond components. Previous experiments reported nonradiative lifetimes in the same ranges [13, 14, 36, 37]. The obtained results were consistent with the reported values. Using the $\sigma_{01}$ and $N_0$, transmittance through linear absorption was calculated as $(93.3 \pm 1.6)\%$ and $(82.8 \pm 1.3)\%$ for the PBS- and DMSO-solution melanin samples, respectively. These two calculations were in agreement with within 2% pt of the transmittances measured by absorption spectroscopy. Furthermore, the $N_0$ of the DMSO-solution melanin sample was estimated based on the relationship of $N_0 = a/(\rho \frac{4}{3}\pi r^3)$, where $a$ (0.03 mg/mL) is the concentration of the DMSO-solution melanin sample, $\rho$ (1.41 g/cm$^3$) is the density [32], and $r$ (15–75 nm) is the radius of a melanin particle [38]. The estimated $N_0$ ranged from $1.2 \times 10^{16}$ to $1.5 \times 10^{18}$ 1/cm$^3$, in which the fitted value was included. These agreements showed the accuracy of the obtained parameters.

Table 4.1: Absorption cross-sections and nonradiative lifetimes of melanin.

| Parameter | Melanin in PBS solution | Melanin in DMSO solution |
|---|---|---|
| $\sigma_{01}$ [$\times 10^{-18}$ cm$^2$] | $1.8 \pm 0.7$ | $2.1 \pm 0.5$ |
| $\sigma_{12}$ [$\times 10^{-17}$ cm$^2$] | $6 \pm 3$ | $4.8 \pm 0.5$ |
| $\tau_1$ [ns] | $0.15 \pm 0.05$ | $0.03 \pm 0.01$ |
| $\tau_2$ [ps] | $1.2 \pm 0.2$ | $6 \pm 3$ |

The standard error was calculated from three experiments.

### 4.3.3 Number of photons involved in nonlinear absorption by melanin

Figure 4.5 shows the measured data through the open-aperture $z$-scan technique and the fitted data for $n = 2$ and 3. The decrease in transmittance around the sample position of $z = 0$ mm was indicative of the decreased transmittance of 532-nm nanosecond laser at the focus. This can be attributed to reverse-saturable absorption, such as multiphoton absorption and multiple absorption [39]. Since melanin exhibits linear absorption at 532 nm, multiple absorption was involved in the nonlinear absorption mechanism of melanin. $\alpha$ was obtained as 0.247 cm$^{-1}$ from the three experiments, and $\beta_2$ and $\beta_3$ were determined as 2.5 cm/GW and 4.7 cm$^3$/GW$^2$, respectively. The coefficients of determination for $n = 2$ and 3 were 0.965 and 0.843, respectively. A comparison of the two fitted data indicated that $n = 2$ showed better agreement with the measured data. From these results, it could be concluded that the multiple absorption process by 532-nm short-pulsed laser was attributed to sequential two-photon absorption, validating the nonlinear absorption model.

### 4.3.4 Energy deposition in melanosomes

Energy deposition in a melanosome was numerically analyzed using the nonlinear absorption model and the physical parameters obtained. Figure 4.6 shows the energy depositions for various

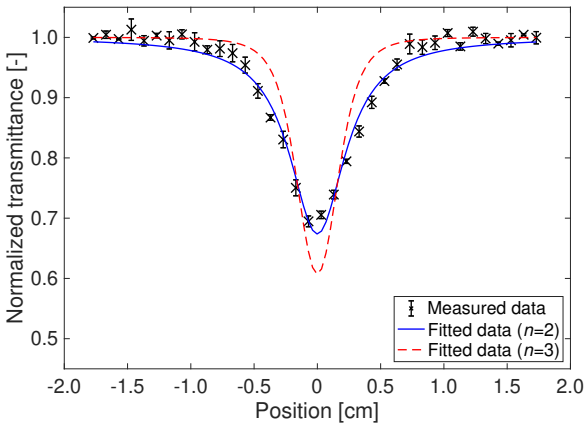


Figure 4.5: Normalized transmittances of melanin dissolved in PBS solution measured by an open-aperture $z$-scan technique and calculated transmittance obtained using the fitting curves for $n = 2$ (solid line) and 3 (dashed line), respectively. The error bars represent the SD of the three experiments. The laser irradiation parameters were 532 nm for wavelength, 0.98 GW/cm$^2$ for power density at the focus, and a single shot.

fluences and pulse widths. The energy deposition increased with increasing fluence and increased with decreasing pulse width owing to nonlinear absorption by melanin in the nanosecond range. The energy deposition reached a maximum at a pulse width of 150 ps for 0.50 J/cm$^2$, 230 ps for 1.00 J/cm$^2$, and 300 ps for 1.50 J/cm$^2$. These picosecond laser pulses delivered optical energy on average approximately 3.1 times more efficiently than a 5-ns laser pulse at the fluence levels. The pulse width at which energy deposition was maximal depended on the irradiated fluence, and melanosomes efficiently absorbed optical energy at subnanosecond pulse widths. The energy deposition decreased as the pulse width decreased from the pulse width at which the energy deposition was at a maximum. This is because the nonlinear absorption coefficient of melanosomes at shorter pulse widths did not increase even at a high fluence compared to that at the pulse width at which the energy deposition was maximized.

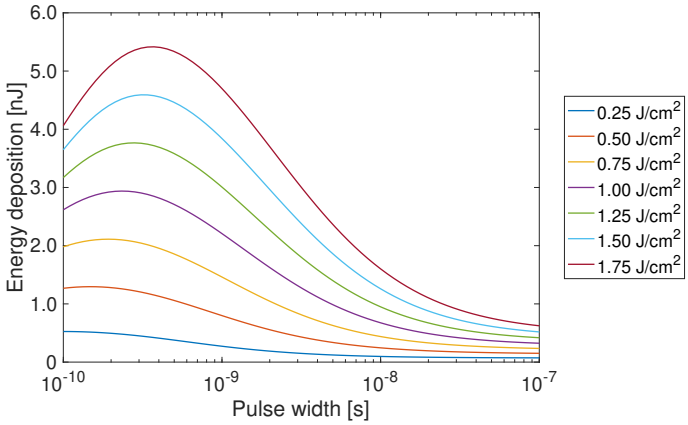


Figure 4.6: Energy depositions in melanosomes for different fluences and pulse widths.

### 4.3.5 Numerical comparison of energy deposition between short-pulsed laser clinical treatments

The differences in treatment effect between picosecond and nanosecond lasers were evaluated in terms of energy deposition in a melanosome with and without considering nonlinear absorption by melanin. Figure 4.7 shows the energy deposition calculated with the clinical parameters, as listed in Table 4.2. Four relevant clinical studies were found [19–21, 31], but one of them was removed from the evaluation because it did not mention the values of pulse width used in treatment [31]. The picosecond laser treatments used lower fluences than the nanosecond laser treatments. The maximum energy deposition was calculated from the maximum fluence or the minimum pulse width, while the minimum energy deposition was calculated from the minimum fluence or the maximum pulse width. Considering only linear absorption, the energy depositions by picosecond lasers were smaller than those by nanosecond lasers. Compared to the threshold, the energy depositions by nanosecond lasers were comparable, while the energy depositions by picosecond lasers were smaller. On the other hand, considering nonlinear absorption, a picosecond laser provided partially a similar amount of energy as a nanosecond laser in Study A, and a greater amount of energy than a nanosecond laser in Study B. In Study C, a picosecond laser provided a smaller amount of energy than a nanosecond laser. Both energy depositions by picosecond and nanosecond lasers were larger than the threshold. The computational analysis demonstrated that picosecond lasers produced treatment effects at lower fluences in terms of energy deposition, showing consistency with the clinical study results.

## 4.4 Discussion

Nonlinear absorption by melanin at a wavelength of 532 nm was modeled based on sequential two-photon absorption in the singlet state. Previous studies reported that fluorescence emission from nonlinear absorption by melanin in the NIR range was derived from sequential two- or three-photon absorption [15, 40], while the nonlinear absorption process at 532 nm has been poorly investigated. In the $z$-scan experiment, the fitted data for $n = 2$ showed better agreement with the measured data. Since melanin exhibits linear absorption over the broad wavelength range, excitation from the singlet state was considered the main pathway for the second absorption step [13]. Therefore, nonlinear absorption by melanin at a wavelength of 532 nm was characterized based on the sequential two-photon absorption. Because the number of photons involved in nonlinear absorption by melanin depends on the excitation wavelength, further investigation of the nonlinear absorption mechanism is required to apply energy deposition analysis to other excitation wavelengths. Energy deposition analysis of melanosomes with a laser wavelength appropriate for benign pigmented lesions can be performed by modeling the wavelength dependency of nonlinear absorption by melanin.

Table 4.2: Short-pulsed laser clinical treatment conditions for epidermal pigmented lesions.

| Study | Wavelength | Pulse width | Fluence | Spot size | Skin type | Endpoint |
|---|---|---|---|---|---|---|
| A [20] | 532 nm | 750 ps | 0.3–0.5 J/cm$^2$ | 3 mm | III, IV, V | IW$^\dagger$ |
| | | 2 ns | 0.5–1.2 J/cm$^2$ | 3 mm | | |
| B [21] | 532 nm | 450 ps | 0.3–0.5 J/cm$^2$ | 3–4 mm | III, IV, V | SIW$^\ddagger$ |
| | | 10 ns | 0.6–0.8 J/cm$^2$ | 3–4 mm | | |
| C [19] | 532 nm | 750 ps | 0.2–0.5 J/cm$^2$ | 3, 4 mm | III, IV | SIW$^\ddagger$ |
| | | 5–10 ns$^\S$ | 1.2 J/cm$^2$ | 3 mm | | |

$^\dagger$ IW, immediate whitening.
$^\ddagger$ SIW, slight immediate whitening.
$^\S$ The nanosecond laser treatment was performed for a skin biopsy of the lesion to compare the differences in skin reaction from the picosecond laser treatment.

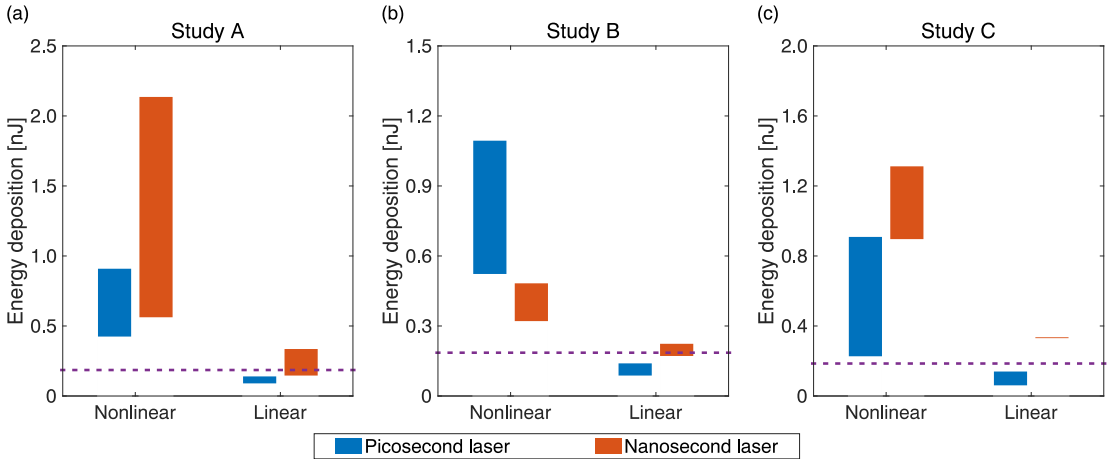


Figure 4.7: Energy depositions in melanosomes calculated with the laser irradiation parameters used in Studies (a) A, (b) B, and (c) C (see Table 4.2). The calculations were performed with and without taking into account nonlinear absorption by melanin. The maximum value was obtained from the maximum fluence or the minimum pulse width, while the minimum was obtained from the minimum fluence or the maximum pulse width. The dashed lines show the estimated threshold energy deposition.

The transmittance measurements used synthetic melanin for the melanin samples. The obtained $\sigma_{01}$ was of the same order of magnitude as the literature value at a wavelength of 800 nm, but slightly smaller. The magnitude relationship was inverse to the increase in linear absorption with decreasing wavelength, which may have been caused by the different types of melanin used [41]. The nonradiative lifetimes obtained were close to those determined by previous pump-probe experiments using various melanins, including human samples [13, 14, 36, 37]. This may have been because the linear absorption spectral shape of the synthetic melanin used was similar to that of human melanin, *i.e.*, a broad absorption spectrum. The similarity of the lifetimes suggested that similar molecules were targeted and similar energy levels were excited between the previous experiments and ours [13]. The time scale of energy relaxation processes depends on the surrounding medium (see Table 4.1). While the melanin samples used were in solution, *in*

*vivo* melanin is packaged within melanosomes, which may affect absorption cross-sections and nonradiative lifetimes. Such parameters derived from *in vivo* melanin can be determined using photoacoustic techniques with high absorption contrast [42].

The computational analysis demonstrated that picosecond lasers produced treatment effects at lower fluences than nanosecond lasers in terms of energy deposition (see Fig. 4.7). The energy depositions by picosecond lasers were less than the threshold without considering nonlinear absorption, and vice versa with considering nonlinear absorption. The analysis of Studies A and B with the nonlinear absorption model showed that the picosecond lasers provided a similar or greater amount of energy than the nanosecond lasers. In these clinical studies, picosecond lasers removed epidermal pigmented lesions more effectively with a lower incidence of PIH at lower fluences than nanosecond lasers [20, 21]. The shorter the pulse width, the more localized the damage [43]. The efficient energy delivery was considered to result in a safer and more efficacious treatment using picosecond laser. The analysis of Study C showed that the nanosecond laser provided a greater amount of energy than the picosecond laser when nonlinear absorption was taken into account. The clinical study showed a greater degree of tissue damage with the nanosecond laser from histological comparison [19]. The length of subsequent thermal diffusion from melanin inside during the nanosecond laser [44], estimated by $\delta_T = 2\sqrt{D_T \tau_p}$, where $D_T$ is the thermal diffusivity of melanin ($1.4 \times 10^{-3}$ cm$^2$/s) [32] and $\tau_p$ is the pulse width, was approximately two to three times longer than during the picosecond laser. The excessive energy deposition and large thermal diffusion were considered to decrease the safety of the nanosecond laser treatment. In summary, the nonlinear absorption-based analysis of the clinical studies demonstrated the differences in treatment effect between picosecond and nanosecond lasers reported in clinical studies can be evaluated.

The results of the computational analysis suggested the potential to establish distinct irradiation endpoints because the energy depositions calculated with the nonlinear absorption model were larger than the threshold. Short-pulsed laser treatment of epidermal pigmented lesions has a risk of PIH, especially in darker skin types [45]. The determination of desirable irradiation endpoints is therefore strongly required for safer treatment [46]. In the current clinical setting, the irradiation endpoint is usually immediate whitening after the laser shot [19–21, 46]. However, there is a clinical study that reported successful whitening without the phenomenon [47]. A previous study also indicated that a lower fluence of picosecond laser could produce treatment effects [29]. These studies suggest that immediate whitening may not always be necessary. Validation of the numerical results will lead to an improved selection of irradiation parameters for the treatment of epidermal pigmented lesions. The computational analysis assumed energy deposition in melanosomes in water, but energy deposition in epidermal melanosomes could be greater because the fluence rate in the tissue increases from that of an incident laser pulse owing to backscattering by the surrounding tissue [48]. Additionally, a temporal laser pulse profile stretches owing to multiple scattering by the tissue [49]. This effect may shift the energy deposition shown in Fig. 4.6 to a value at a longer pulse width. The effects of the surrounding tissue on energy deposition in melanosomes need to be considered.

The computational analysis also indicated that a robust evaluation of the treatment effect between different short-pulsed lasers can be provided. Currently, picosecond laser treatment has been evaluated by statistical comparison with nanosecond laser treatment in clinical studies. However, whether significant differences in the safety and efficacy were observed varied between clinical studies [20, 20, 21]. In terms of irradiation parameters, a spot size of 2–4 mm remained almost similar, but the nanosecond laser treatments used approximately twice the fluence of the picosecond laser treatments [20, 21, 31, 50]. In contrast, as a result of the nonlinear absorption-based analysis, it was confirmed that picosecond lasers produced treatment effects at lower fluences owing to the efficient energy delivery by picosecond laser. The numerical comparisons using clinical parameters demonstrated that the differences in treatment effect between picosecond and nanosecond lasers reported in clinical studies can be evaluated. This finding suggested the feasibility of computational simulations augmenting preclinical and clinical evaluations.

## 4.5 Conclusion of this chapter

The nonlinear absorption-based analysis with the measured absorption cross-sections and nonradiative lifetimes was performed to evaluate energy deposition in melanosomes. The picosecond laser was found to be most efficient in delivering energy to melanosomes. The computational analysis demonstrated that nonlinear absorption by melanin has a significant influence on the mechanism of short-pulsed laser treatment and can explain the difference in treatment effect between picosecond and nanosecond lasers reported in clinical studies. These results suggested the feasibility of computational simulations for the augmentation of preclinical and clinical evaluations.

## References


[1] L. Guss, M.P. Goldman, and D.C. Wu. Picosecond 532 nm neodymium-doped yttrium aluminium garnet laser for the treatment of solar lentigines in darker skin types: Safety and efficacy. *Dermatologic Surgery*, 43(3):456–459, 2017.

[2] C. Chesnut, J. Diehl, and G. Lask. Treatment of nevus of Ota with a picosecond 755-nm alexandrite laser. *Dermatologic Surgery*, 41(4):508–510, 2015.

[3] K.Y. Kung, S.Y.N. Shek, C.K. Yeung, and H.H.L. Chan. Evaluation of the safety and efficacy of the dual wavelength picosecond laser for the treatment of benign pigmented lesions in Asians. *Lasers in Surgery and Medicine*, 51(1):14–22, 2019.

[4] D.D.M. Ho, R. London, G.B. Zimmerman, and D.A. Young. Laser-tattoo removal—a study of the mechanism and the optimal treatment strategy via computer simulations. *Lasers in Surgery and Medicine*, 30(5):389–397, 2002.

[5] R.R. Anderson, R.J. Margolis, S. Watenabe, T. Flotte, G.J. Hruza, and J.S. Dover. Selective photothermolysis of cutaneous pigmentation by Q-switched Nd:YAG laser pulses at 1064, 532, and 355 nm. *Journal of Investigative Dermatology*, 93(1):28–32, 1989.

[6] M. Xu and L.V. Wang. Photoacoustic imaging in biomedicine. *Review of Scientific Instruments*, 77(4):041101, 2006.

[7] J. Tian, B. Chen, and D. Li. Efficacy evaluation and treatment parameter optimization for laser surgery of Ota's nevus based on an advanced non-equilibrium bio-tissue heat transfer model. *Lasers in Medical Science*, 37(1):369–379, 2022.

[8] M. Luecking, R. Brinkmann, S. Ramos, W. Stork, and N. Heussner. Capabilities and limitations of a new thermal finite volume model for the evaluation of laser-induced thermomechanical retinal damage. *Computers in Biology and Medicine*, 122:103835, 2020.

[9] Y. Shimojo, T. Nishimura, H. Hazama, N. Ito, and K. Awazu. Picosecond laser-induced photothermal skin damage evaluation by computational clinical trial. *Laser Therapy*, 29(1):61–72, 2020.

[10] B. Varghese, V. Bonito, M. Jurna, J. Palero, M. Horton, and R. Verhagen. Influence of absorption induced thermal initiation pathway on irradiance threshold for laser induced breakdown. *Biomedical Optics Express*, 6(4):1234–1240, 2015.

[11] D.J. Stolarski, J. Stolarski, R.J. Thomas, G.D. Noojin, K.J. Schuster, and B.A. Rockwell. Nonlinear absorption studies of melanin. *Proceedings of SPIE*, 4617:161–171, 2002.

[12] D. Leupold, M. Scholz, G. Stankovic, J. Reda, S. Buder, R. Eichhorn, G. Wessler, M. Stücker, K. Hoffmann, J. Bauer, and C. Garbe. The stepwise two-photon excited melanin fluorescence is a unique diagnostic tool for the detection of malignant transformation in melanocytes. *Pigment Cell Melanoma Research*, 24(3):438–445, 2011.

[13] I.R. Piletic, T.E. Matthews, and W.S. Warren. Probing near-infrared photorelaxation pathways in eumelanins and pheomelanins. *The Journal of Physical Chemistry A*, 114(43):11483–11491, 2010.

[14] T. Ye and J.D. Simon. Comparison of the ultrafast absorption dynamics of eumelanin and pheomelanin. *The Journal of Physical Chemistry B*, 107(40):11240–11244, 2003.

[15] R. Eichhorn, G. Wessler, M. Scholz, D. Leupold, G. Stankovic, S. Buder, M. Stuecker, and K. Hoffmann. Early diagnosis of melanotic melanoma based on laser-induced melanin fluorescence. *Journal of Biomedical Optics*, 14(3):034033, 2009.

[16] K. Teuchner, W. Freyer, D. Leupold, A. Volkmer, D.J.S. Birch, P. Altmeyer, M. Stucker, and K. Hoffmann. Femtosecond two-photon excited fluorescence of melanin. *Photochemistry and Photobiology*, 70(2):146–151, 1999.

[17] P. Meredith and J. Riesz. Radiative relaxation quantum yields for synthetic eumelanin. *Photochemistry and Photobiology*, 79(2):211–216, 2004.

[18] G. Perna, M.C. Frassanito, G. Palazzo, A. Gallone, A. Mallardi, P. Biagi, and V. Capozzi. Fluorescence spectroscopy of synthetic melanin in solution. *Journal of Luminescence*, 129(1):44–49, 2009.

[19] K. Negishi, H. Akita, and Y. Matsunaga. Prospective study of removing solar lentigines in Asians using a novel dual-wavelength and dual-pulse width picosecond laser. *Lasers in Surgery and Medicine*, 50(8):851–858, 2018.

[20] C. Ungaksornpairote, W. Manuskiatti, N. Junsuwan, and R. Wanitphakdeedecha. A prospective, split-face, randomized study comparing picosecond to Q-switched Nd:YAG laser for treatment of epidermal and dermal pigmented lesions in Asians. *Dermatologic Surgery*, 46(12):1671–1675, 2020.

[21] J.Y. Kim, J. Yang, G. Huh, Y.J. Choi, and W.S. Kim. A split-face, single-blinded, randomized controlled comparison of 532 nm picosecond neodymium-doped yttrium aluminum garnet laser versus 532 nm Q-switched neodymium-doped yttrium aluminum garnet laser in the treatment of solar lentigines. *Annals of Dermatology*, 32(1):8–13, 2020.

[22] W. Cao, X. Zhou, N.C. McCallum, Z. Hu, Q.Z. Ni, U. Kapoor, C.M. Heil, K.S. Cay, T. Zand, A.J. Mantanona, A. Jayaraman, A. Dhinojwala, D.D. Deheyn, M.D. Shawkey, M.D. Burkart, J.D. Rinehart, and N.C. Gianneschi. Unraveling the structure and function of melanin through synthesis. *Journal of the American Chemical Society*, 143(7):2622–2637, 2021.

[23] S. Zongo, K. Sanusi, J. Britton, P. Mthunzi, T. Nyokong, M. Maaza, and B. Sahraoui. Nonlinear optical properties of natural laccaic acid dye studied using Z-scan technique. *Optical Materials*, 46:270–275, 2015.

[24] M. Sheik-Bahae, A.A. Said, T.H. Wei, D.J. Hagan, and E.W.V. Stryland. Sensitive measurement of optical nonlinearities using a single beam. *IEEE Journal of Quantum Electronics*, 26(4):760–769, 1990.

[25] B. Gu, X.Q. Huang, S.Q. Tan, M. Wang, and W. Ji. Z-scan analytical theories for characterizing multiphoton absorbers. *Applied Physics B*, 95(2):375–381, 2009.

[26] B. Gu, W. Ji, P.S. Patil, S.M. Dharmaprakash, and H.T. Wang. Two-photon-induced excited-state absorption: Theory and experiment. *Applied Physics Letters*, 92(9):091118, 2008.

[27] H. Xiaoqin. Analytical resolution of nonlinear optical absorption in polymer. In *2002 International Symposium on Nonlinear Theory and its Applications*, volume N2-6-6, page 539–542, 2002.

[28] S.L. Jacques. Optical absorption of melanin. https://omlc.org/spectra/melanin/, Accessed on December 10, 2021.

[29] Y. Shimojo, T. Nishimura, H. Hazama, N. Ito, and K. Awazu. Incident fluence analysis for 755-nm picosecond laser treatment of pigmented skin lesions based on threshold fluences for melanosome disruption. *Lasers in Surgery and Medicine*, 53(8):1096–1104, 2021.

[30] S.L. Jacques, R.D. Glickman, and J.A. Schwartz. Internal absorption coefficient and threshold for pulsed laser disruption of melanosomes isolated from retinal pigment epithelium. *Proceedings of SPIE*, 2681:468–477, 1996.

[31] V. Vachiramon, W. Iamsumang, and K. Triyangkulsri. Q-switched double frequency Nd:YAG 532-nm nanosecond laser vs. double frequency Nd:YAG 532-nm picosecond laser for the treatment of solar lentigines in Asians. *Lasers in Medical Science*, 33(9):1941–1947, 2018.

[32] J. Neumann and R. Brinkmann. Boiling nucleation on melanosomes and microbeads transiently heated by nanosecond and microsecond laser pulses. *Journal of Biomedical Optics*, 10(2):024001, 2005.

[33] S.L. Jacques and D.J. McAuliffe. The melanosome: Threshold temperature for explosive vaporization and internal absorption coefficient during pulsed laser irradiation. *Photochemistry and Photobiology*, 53(6):769–775, 1991.

[34] P. Deladurantaye, S. Méthot, O. Mermut, P. Galarneau, and P.J. Rochette. Potential of submicrosecond laser pulse shaping for controlling microcavitation in selective retinal therapies. *Biomedical Optics Express*, 11(1):109–132, 2020.

[35] K. Teuchner, J. Ehlert, W. Freyer, D. Leupold, P. Altmeyer, M. Stücker, and K. Hoffmann. Fluorescence studies of melanin by stepwise two-photon femtosecond laser excitation. *Journal of Fluorescence*, 10(3):275–281, 2000.

[36] J.B. Nofsinger, T. Ye, and J.D. Simon. Ultrafast nonradiative relaxation dynamics of eumelanin. *The Journal of Physical Chemistry B*, 105(14):2864–2866, 2001.

[37] S.E. Forest and J.D. Simon. Wavelength-dependent photoacoustic calorimetry study of melanin. *Photochemistry and Photobiology*, 68(3):296–298, 1998.

[38] N. Kollias, R.M. Sayre, L. Zeise, and M.R. Chedekel. New trends in photobiology: Photoprotection by melanin. *Journal of Photochemistry and Photobiology B: Biology*, 9(2):135–160, 1991.

[39] D. Fu, T. Ye, T.E. Matthews, G. Yurtsever, and W.S. Warren. Two-color, two-photon, and excited-state absorption microscopy. *Journal of Biomedical Optics*, 12(5):054004, 2007.

[40] J. Kerimo, M. Rajadhyaksha, and C.A. DiMarzio. Enhanced melanin fluorescence by stepwise three-photon excitation. *Photochemistry and Photobiology*, 87(5):1042–1049, 2011.

[41] V. Capozzi, G. Perna, P. Carmone, A. Gallone, M. Lastella, E. Mezzenga, G. Quartucci, M. Ambrico, V. Augelli, P. Biagi, and others. Optical and photoelectronic properties of melanin. *Thin Solid Films*, 511:362–366, 2006.

[42] A. Danielli, C.P. Favazza, K. Maslov, and L.V. Wang. Picosecond absorption relaxation measured with nanosecond laser photoacoustics. *Applied Physics Letters*, 97(16):163701, 2010.

[43] S. Watanabe, R.R. Anderson, S. Brorson, G. Dalickas, J.G. Fujimoto, and T.J. Flotte. Comparative studies of femtosecond to microsecond laser pulses on selective pigmented cell injury in skin. *Photochemistry and Photobiology*, 53(6):757–762, 1991.

[44] A.L. McKenzie. Physics of thermal processes in laser-tissue interaction. *Physics in Medicine & Biology*, 35(9):1175–1210, 1990.

[45] C.C. Wang, Y.M. Sue, C.H. Yang, and C.K. Chen. A comparison of Q-switched alexandrite laser and intense pulsed light for the treatment of freckles and lentigines in Asian persons: A randomized, physician-blinded, split-face comparative trial. *Journal of the American Academy of Dermatology*, 54(5):804–810, 2006.

[46] M. Wanner, F.H. Sakamoto, M.M. Avram, H.H. Chan, M. Alam, Z. Tannous, and R.R. Anderson. Immediate skin responses to laser and light treatments: Therapeutic endpoints: How to obtain efficacy. *Journal of the American Academy of Dermatology*, 74(5):821–833, 2016.

[47] T. Ohshiro, T. Ohshiro, K. Sasaki, and K. Kishi. Picosecond pulse duration laser treatment for dermal melanocytosis in Asians: A retrospective review. *Laser Therapy*, 25(2):99–104, 2016.

[48] E.V. Ross, J. Raythen, and R.R. Anderson. "Photon recycling" can enhance cutaneous response to lasers: A pilot human study. *Lasers in Surgery and Medicine*, 54(1):152–156, 2022.

[49] B. Morales-Cruzado, F.G. Pérez-Gutiérrez, D.F. Lange, and R. Romero-Méndez. Study of the effect introduced by an integrating sphere on the temporal profile characterization of short laser pulses propagating through a turbid medium. *Applied Optics*, 54(9):2383–2390, 2015.

[50] Y. Ge, Y. Yang, L. Guo, M. Zhang, Q. Wu, R. Zeng, H. Rong, G. Jia, H. Shi, J. Fang, and T. Lin. Comparison of a picosecond alexandrite laser versus a Q-switched alexandrite laser for the treatment of nevus of Ota: A randomized, split-lesion, controlled trial. *Journal of the American Academy of Dermatology*, 83(2):397–403, 2020.

# Chapter 5

# Picosecond laser-induced photothermal skin damage evaluation by computational clinical trial

## 5.1 Introduction

Studies performed through Chapters 2 to 4 have analyzed picosecond laser-skin interactions at the tissue, cell, and molecular scales. The obtained physical parameters of the skin and the light transport model have enabled computational simulations of picosecond laser treatment to calculate the light distribution in the skin, melanosomes, and melanin. The results have suggested that computational simulations can augment preclinical and clinical studies. Based on these findings, this chapter will address the question of how computational laser treatment can be applied to computational clinical trials for rapid and low-cost clinical applications of novel laser devices. As a specific example, photothermal skin damage induced by a novel picosecond laser device is evaluated based on a comparison with approved picosecond and nanosecond laser devices in a computational clinical trial. A comparison of photothermal damage will confirm that computational laser treatment can provide the same results as those achieved in clinical trials.

In laser skin treatment, a significant amount of laser energy is injected to produce the treatment effect. There is a risk of damage to normal tissues surrounding the surgical site. Because laser treatments should be performed under the condition that the risk is acceptably small, the evaluation of damage to normal tissue is required in preclinical and clinical evaluations. Although the risk evaluation can be performed by *ex vivo* and *in vivo* experiments [1–3], such experiments have difficulties in that the physical phenomena induced by picosecond laser are too fast to make direct observations. For this reason, conventional trials have required statistical comparison between large groups of patients and histological analysis of laser-irradiated tissues [4]. These processes require massive amounts of time and cost, which prevents smooth clinical applications. Due to delays in the regulatory evaluation, some picosecond lasers have been used without regulatory

This chapter was originally published under the title, "Picosecond laser-induced photothermal skin damage evaluation by computational clinical trial" by Yu Shimojo, Takahiro Nishimura, Hisanao Hazama, Nobuhisa Ito, and Kunio Awazu in *Laser Therapy* 29(1):61–72 (2020).

approval in Japan; as a result, medical malpractices or accidents have occurred [5]. Because this problem also presents a barrier to the development and clinical application of novel laser devices, not only quantitative and reproducible but also rapid and low-cost methods for the evaluation of laser treatment are urgently required.

As a third trial, in addition to preclinical and clinical trials, computational clinical trials can evaluate the safety and efficacy of laser treatment [6]. In computational clinical trials, preclinical and clinical evaluations are performed by computational modeling and simulation of a laser treatment procedure. The trials offer quantitative and reproducible scientific evidence because computational simulations can reproduce physical phenomena induced by laser irradiation. According to reports from the FDA, computational simulations help investigate how a treatment behaves in many clinically relevant cases, without temporal, financial, or ethical considerations [7]. Computational simulations can exclude individual differences between subjects, variations in surgical technique by operators in clinical trial data, and uncertainty of scientific evidence for extrapolation of animal study data to humans. Once computational clinical trials are established, they can have huge potential to reduce barriers to the development of novel laser devices, augment and partially replace preclinical and clinical trials, and facilitate rapid and low-cost clinical applications of laser devices.

For computational clinical trials, mathematical models of laser-tissue interactions are required. By modeling light transport in skin with the MC method, diffuse reflectance spectra of tissue were simulated for quantitative monitoring of chromophores in biological tissues. The model yielded results that agree reasonably well with the *in vivo* measurement when a skin model was provided with reasonable physical and structural parameters of the tissues [8]. By modeling the thermal response of tissue, laser tissue coagulation has been simulated [9, 10]. The validity of the model was evaluated by comparing it with MRI-based temperature data obtained from the *in vivo* experiment. The computational simulation of the temperature distribution showed good agreement with the MRI-based data. [9]. By modeling light and heat transfer in tissue, photothermal effects, including tissue coagulation and vaporization, for the laser treatment of benign prostatic hyperplasia have been simulated [11, 12]. The simulation results were found to be consistent with the results of the *ex vivo* experiment [11]. These models enable computational simulations to reproduce light propagation and thermal diffusion in tissue. Therefore, computational simulations of light propagation and thermal diffusion can be applied to evaluate photothermal skin damage between novel and approved laser devices.

## 5.2 Materials and Methods

### 5.2.1 Computational clinical trial model

The computational clinical trial evaluates the approved laser device (Device A) versus the approved laser devices (Devices B and C) due to the history of approval of Devices B and C before Device A. Device A was a picosecond alexandrite laser with a wavelength of 755 nm. Device B was a nanosecond alexandrite laser with a wavelength of 755 nm, and Device C was a picosecond Nd:YAG

laser with wavelengths of 532 and 1064 nm. Table 5.1 shows the specifications of picosecond and nanosecond laser devices. The computational simulation assumed that all the absorbed laser energy was converted to heat to calculate the maximum photothermal damage induced by laser irradiation. As indicators of photothermal damage, optical penetration depth $\delta$, temperature rise $T$, and thermal damage rate $P$ in normal skin tissue are employed. $\delta$, $T$, and $P$ in normal skin tissue were compared between the novel and approved laser devices. Figure 5.1 describes the steps of computational modeling and simulation: an MC simulation of light propagation [13], a finite difference method for thermal diffusion calculation [14], and an Arrhenius model to quantify thermal damage [15]. Light propagation in skin tissue is calculated to obtain energy deposition. The MC simulation assumes a linear absorption process [13]. Nonlinear absorption induced by picosecond laser leads to the formation of LIOB and the subsequent creation of plasma above the irradiance threshold of $10^{12}$–$10^{13}$ W/cm$^2$ [16]. The threshold is two orders of magnitude greater than the maximum power density of Devices A, B, and C. Thus, the nonlinear absorption process is assumed to be negligible in this trial. Furthermore, tissue damage due to photoacoustic effects is also assumed to be negligible. The highest generation of stress waves by Device A was estimated at 0.1 MPa referring to Ref. [17, 18]. The calculated value is three orders of magnitude lower than the damage threshold of 30 MPa [19]. From the calculated fluence distribution, $\delta$ is obtained. Here, heat diffusion during a laser pulse can be negligible because the thermal confinement condition is satisfied. Based on this approximation, thermal diffusion can be calculated by setting the initial value of a heat source as the energy deposition distribution after laser irradiation. From the calculated distribution, $T$ and $P$ are calculated. The degree of thermal damage depends on the temperature of the skin tissue and the exposure time at that temperature [20, 21].

Table 5.1: Specifications of picosecond and nanosecond laser devices numerically evaluated in a computational clinical trial. Table reproduced from Ref. [22].

| | Device A | Device B | Device C |
|---|---|---|---|
| Wavelength | 755, 532 nm | 755 nm | 1064, 532 nm |
| Pulse width | 550–750 ps | 50–100 ns | 750 ps, 2 ns |
| Spot size | 1.5–10 mm (□) | 2–6 mm ($\phi$) | 2–8 mm ($\phi$) |
| Fluence | 0.21–6.37 J/cm$^2$ | 1.6–18 J/cm$^2$ | 0.2–10.0, 0.2–2.5 J/cm$^2$ |
| Repetition rate | Single, 1–10 Hz | Single, 1–10 Hz | Single, 1–10 Hz |

### 5.2.2 Three-dimensional numerical skin tissue model

A 3D numerical skin model was constructed as described in Chapter 2. The skin model consisted of the epidermis, dermis, and subcutaneous fat. The dermis included three different sizes of blood vessels; capillary vessels, upper dermis vessels, and deep dermis vessels. The skin tissue model was constructed with cube voxels of 500 × 500 × 400 elements. The voxel size was 10 $\mu$m × 10 $\mu$m × 10 $\mu$m. The depth direction was set along the $z$ axis. The skin surface was set as $z$ = 0 mm. The vertical plane to the $z$ axis was defined as the $xy$ plane. The center of the skin surface was ($x$, $y$) = (0 mm, 0 mm). The thickness of the epidermis, dermis, and subcutaneous fat was set

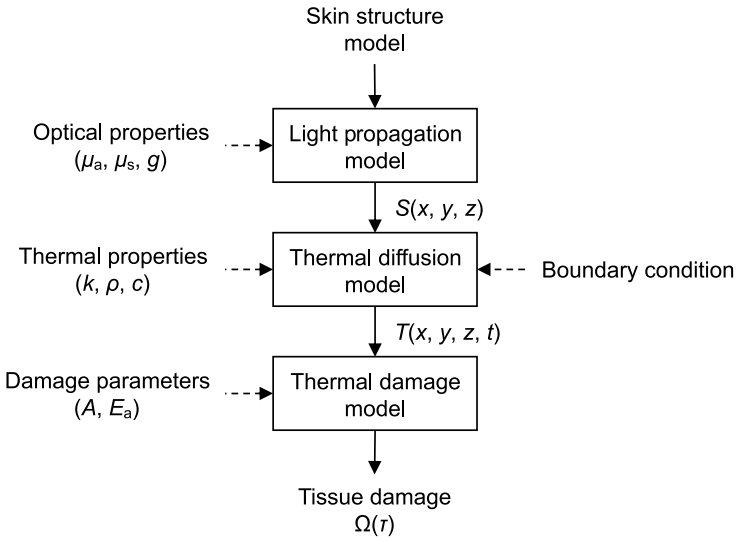


Figure 5.1: Schematic diagram of the computational modeling and simulation of light and heat transfer. After creating a numerical skin model, light propagation in the skin is calculated with optical properties to produce the spatial distribution of energy deposition $S(x, y, z)$. By using the energy deposition distribution as the initial value of a heat source, thermal diffusion is calculated to obtain the temperature distribution $T(x, y, z, t)$. From the calculated temperature rise, the spatial distribution of thermal damage rate in the skin model is obtained. Figure reproduced from Ref. [22].

as 0.1, 1.1, and 2.8 mm, respectively [23]. Each voxel was assigned the absorption and scattering coefficients, and anisotropy factor, as listed in Table 5.2. The absorption coefficients of the dermis and subcutaneous fat were bloodless parameters.

### 5.2.3 Light propagation calculation

An MC simulation was used to calculate the light distribution in normal skin tissue [13]. The collimated laser beam with uniform spatial distribution was irradiated vertically to the skin surface. The laser wavelength was set to 532, 755, or 1064 nm, according to the specifications of the laser devices. The MC simulation was carried out for 12 million photons to achieve a sufficient light distribution.

### 5.2.4 Thermal diffusion calculation

The $T$ by laser irradiation is determined by the heat capacity and thermal conductivity of skin, and the heat is diffused at a speed proportional to the temperature gradient. Thermal diffusion promotes an increase in the temperature of normal tissues and causes cell necrosis and protein coagulation [34]. The time variation of the temperature distribution in skin was calculated using the heat conduction equation [14]:

$$\rho c \frac{\partial T}{\partial t} = k \nabla^2 T + S, \tag{5.1}$$

Table 5.2: Optical, thermal, and damage parameters for light and heat transfer simulation. Table reproduced from Ref. [22].

| | Epidermis | Dermis | Fat | Blood |
|---|---|---|---|---|
| **Optical properties** | | | | |
| $\lambda$ = 532 nm [24–27] | | | | |
| Absorption coefficient [mm$^{-1}$] | 1.43 | 0.053 | 0.09 | 10.0 |
| Scattering coefficient [mm$^{-1}$] | 60.5 | 38.8 | 31.4 | 29.5 |
| Anisotropy factor [-] | | 0.9 | | |
| $\lambda$ = 755 nm [24, 25, 27, 28] | | | | |
| Absorption coefficient [mm$^{-1}$] | 0.46 | 0.025 | 0.01 | 0.3 |
| Scattering coefficient [mm$^{-1}$] | 39.4 | 23.8 | 21.7 | 32.1 |
| Anisotropy factor [-] | | 0.9 | | |
| $\lambda$ = 1064 nm [24, 25, 27, 29] | | | | |
| Absorption coefficient [mm$^{-1}$] | 0.16 | 0.024 | 0.05 | 0.2 |
| Scattering coefficient [mm$^{-1}$] | 29.1 | 17.7 | 16.9 | 25.0 |
| Anisotropy factor [-] | | 0.9 | | |
| **Thermal properties** [30–33] | | | | |
| Thermal conductivity [$\times 10^{-3}$ W/(cm·K)] | 2.09 | 3.00 | 2.05 | 4.92 |
| Specific heat [J/(g·K)] | 3.60 | 3.22 | 2.30 | 3.84 |
| Density [g/cm$^3$] | 1.19 | 1.12 | 0.97 | 1.00 |
| Internal heat source [W/cm$^3$] | Output from MC simulations | | | |
| **Damage parameters** [15] | | | | |
| Frequency factor [1/s] | $8.82 \times 10^{94}$ ($T \leq 53$°C), $1.297 \times 10^{31}$ ($T > 53$°C ) | | | |
| Activation energy [J/mol] | $6.028 \times 10^5$ ($T \leq 53$°C), $2.04 \times 10^5$ ($T > 53$°C ) | | | |
| Gas constant [J/(mol·K)] | 8.314 | | | |

where $\rho$ [g/cm$^3$] is the density, $c$ [J/(g·K)] is the specific heat, $k$ [W/(cm·K)] is the thermal conductivity, and $S$ [W/cm$^3$] is the internal heat source, as shown in Table 5.2. The heat source term was present during a laser pulse. This equation was solved with the finite difference technique. The adiabatic boundary conditions were applied to the boundaries at $z$ = 4.0 mm and $x$, $y$ = ± 2.5 mm. The convective surface boundary condition was applied at the boundary between air and skin tissue.

$$-k \left.\frac{\partial T}{\partial t}\right|_{z=0} = h(T_{\text{air}} - T_{\text{surface}}), \tag{5.2}$$

where $h$ [W/(cm$^2$·K)] is the heat transfer coefficient between the air and skin (0.001 W/(cm$^2$·K)) [35], $T_{\text{air}}$ [°C] is the temperature at the air, and $T_{\text{surface}}$ [°C] is the temperature at the skin surface. The initial skin and air temperatures were set to 32 and 24°C, respectively. The temporal step size during and after laser irradiation was one-hundredth of a pulse width and 10 nanoseconds, respectively.

### 5.2.5 Thermal damage calculation

The $P$ was quantified with the Arrhenius model with experimentally derived parameters (frequency factor, $A$ and activation energy, $E_{\text{a}}$). The model is based on a unimolecular formulation of the

standard rate process model of tissue damage in chemical kinetics. This model can be used to predict the probability of irreversible thermal damage and to calculate a non-dimensional damage parameter Ω [-] from

$$\Omega(\tau) = \ln\left\{\frac{C(0)}{C(\tau)}\right\} = A\int_0^{\tau} \exp\left\{\frac{E_a}{RT(\tau)}\right\}dt, \tag{5.3}$$

where $C(t)$ [M] is the remaining concentration of undamaged tissue at exposure time $t$ [s], $A$ [1/s] is the frequency factor, $E_a$ [J/mol] is the activation energy for the denaturation of molecules, and $R$ [J/(mol·K)] is the gas constant, as shown in Table 5.2. The concentration ratio of damaged tissue to undamaged tissue at exposure time $\tau$ [s] was expressed using the damage parameter Ω with the following equation [15]:

$$P\ [\%] = 100[1 - \exp\{-\Omega(\tau)\}]. \tag{5.4}$$

The thermal damage of 63.2% ($\Omega \geq 1$) was applied to the threshold for irreversible thermal damage, such as cell necrosis and protein coagulation [15].

### 5.2.6 Irradiation conditions

The laser irradiation conditions for the three devices are listed in Table 5.3. Severe conditions indicate the conditions that provide the maximum fluence in the specification. Clinical conditions indicate the typical conditions used in tattoo removal [4, 36]. The spot shape of Device A was square, while those of Devices B and C were circular. The repetition rates were set at 10 Hz. The thermal diffusion by single pulse irradiation was analyzed for 100 ms to compare Device A with Devices B and C. Because the repetition rate was the highest in their specifications, $T$ and $P$ were severely evaluated. Cooling during and after laser irradiation was not considered.

Table 5.3: Simulation conditions of picosecond and nanosecond laser irradiations. Table reproduced from Ref. [22].

| | Severe conditions | | | | Clinical conditions | | | |
|---|---|---|---|---|---|---|---|---|
| | A | B | C | | A | B | C | |
| Wavelength [nm] | 755 | 755 | 1064 | 532 | 755 | 755 | 1064 | 532 |
| Pulse width [ns] | 0.55 | 50 | 0.75 | | 0.55 | 50 | 0.75 | |
| Spot size [mm] | 2 (□) | 2 ($\phi$) | 2 ($\phi$) | | 3 (□) | 3 ($\phi$) | 3 ($\phi$) | |
| Fluence [J/cm$^2$] | 6.37 | 18 | 10 | 2.5 | 2.83 | 10 | 4.6 | 1.65 |
| Repetition rate [Hz] | 10 | | | | | | | |
| Cooling | None | | | | | | | |

## 5.3 Results

### 5.3.1 Light propagation in the skin model

The difference in $\delta$ between Device A and Devices B and C was evaluated. The $\delta$ was defined as the depth at which the fluence within the skin model reaches $1/e$ (36.8%) of its original fluence at

the surface. Figure 5.2(a) shows the fluence distributions. The irradiated laser pulse was diffused radially due to scattering. Figure 5.2(b) shows the energy deposition distributions. The laser energy was well absorbed by the epidermis and blood vessels. Figure 5.3 shows the $\delta$ of the three devices. The $\delta$ of Device A was 0.85 mm, while the $\delta$ of Device B, Device C with a wavelength of 1064 nm [Device C ($\lambda$ = 1064 nm)], and Device C with a wavelength of 532 nm [Device C ($\lambda$ = 532 nm)] were 0.82, 0.86, and 0.51 mm, respectively. The $\delta$ of Device A was placed between the $\delta$ of Device C ($\lambda$ = 1064 nm) and Device C ($\lambda$ = 532 nm). The comparison indicated that the $\delta$ was similar between Device A and Device C. Figure 5.4 shows the energy deposition profile on the $z$ axis. Laser irradiation with Device B delivered a greater amount of energy to the subcutaneous fat than with Device A. Therefore, it was confirmed that the $\delta$ of Device A is equivalent to those of Devices B and C.

### 5.3.2 Temperature rise

Figure 5.5 shows the time variation of temperature profiles on the $z$ axis for 100 ms after laser irradiation. Immediately after laser irradiation, temperature peaks were found in the epidermis, capillary vessels, upper dermis vessels, and deep dermis vessels, and these temperatures reached a maximum. After 100 ms, the temperature peaks in the blood vessels nearly disappeared due to thermal diffusion. Although the temperature peak in the epidermis became smooth, the peak was still higher than that before laser irradiation. Figure 5.6 shows the maximum temperature of each tissue. Under the severe conditions, the maximum temperature of each tissue after laser irradiation with Device A was not the largest compared with Devices B and C. Moreover, except in the epidermis, the maximum temperature of each tissue under the severe conditions with Device A was lower than that under the clinical conditions with Devices B and C. Therefore, it was confirmed that the $T$ with Device A is lower than those with Devices B and C.

### 5.3.3 Concentration ratio of thermally damaged tissue

The $P$ values were calculated using the $T$ values. After 100 ms, the $P$ peaks were found in the epidermis, capillary vessels, and upper dermis vessels. The maximum $P$ with Device A was 1.2 $\times 10^{-2}$% at most in the epidermis, while those with Devices B and C ($\lambda$ = 1064 nm) were 42 and 7.5 $\times 10^{-6}$%, respectively, in the epidermis, and that with Device C ($\lambda$ = 532 nm) was 99% in the capillary vessels. The $P$ with Device A was much less than the threshold of 63.2%. Therefore, it was confirmed that the $P$ with Device A is equivalent to that with Devices B and C.

## 5.4 Discussion

Comparing Fig. 5.5(a) and (b), the shape of the temperature profile was similar, while the degree was different. Under the set irradiation conditions, Devices A and B had the same wavelength, but the set pulse width and fluence were different. The thermal diffusivities $D_T = k/\rho c$ of epidermis, dermis, and subcutaneous fat are 4.88 $\times 10^{-4}$, 8.32 $\times 10^{-4}$, and 9.19 $\times 10^{-4}$ cm$^2$/s, respectively. The thermal relaxation time can be written as $\tau_{\text{thermal}} = d^2/4D_T$, where $d$ is the

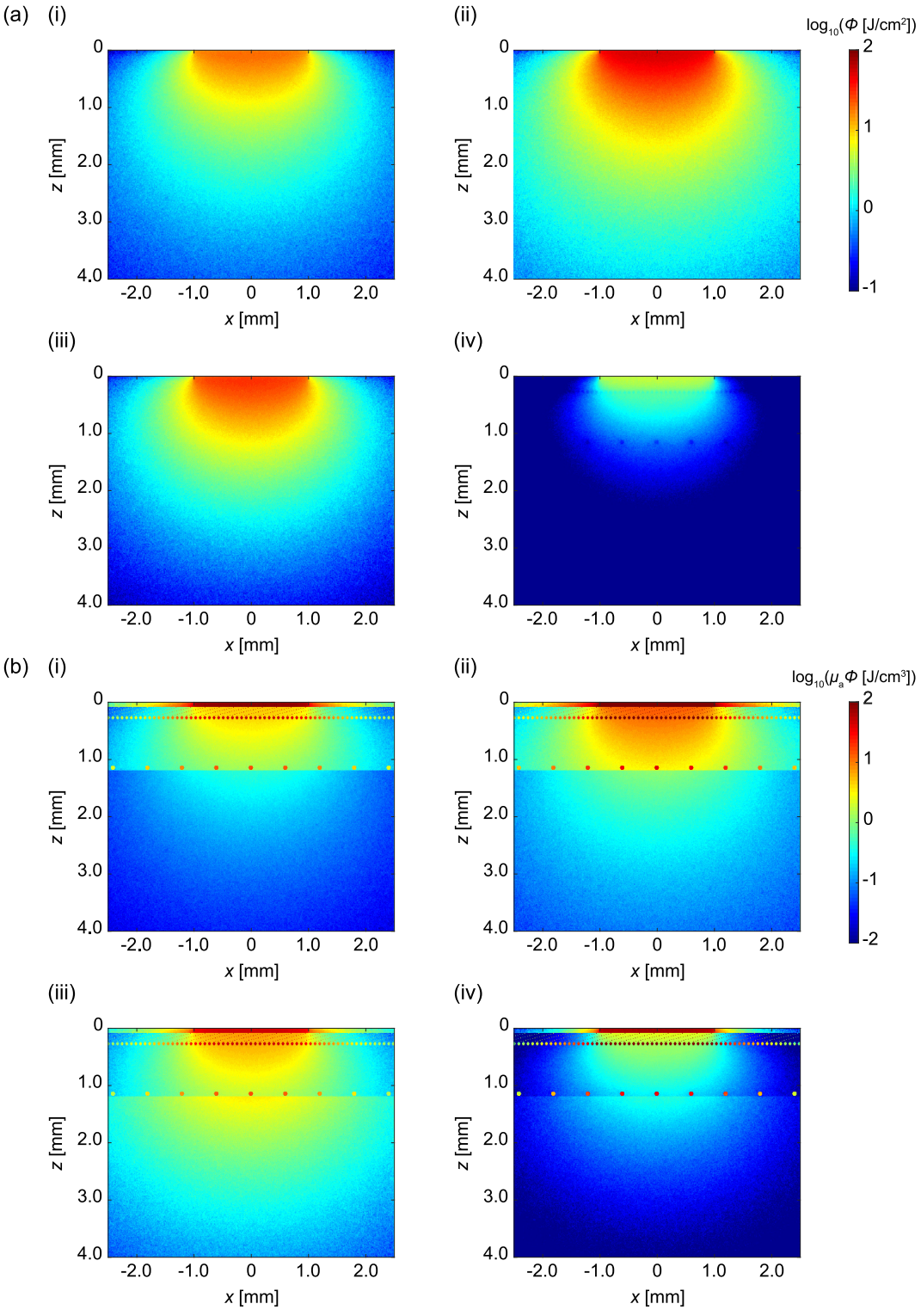


Figure 5.2: Spatial distributions of (a) fluence and (b) energy deposition in the skin model on the $zx$ plane after laser irradiation with (i) Device A (755 nm, 2 mm □, 6.37 J/cm$^2$), (ii) Device B (755 nm, 2 mm $\phi$, 18 J/cm$^2$), (iii) Device C (1064 nm, 2 mm $\phi$, 10 J/cm$^2$), and (iv) Device C (532 nm, 2 mm $\phi$, 2.5 J/cm$^2$) under the severe conditions. Figure reproduced from Ref. [22].

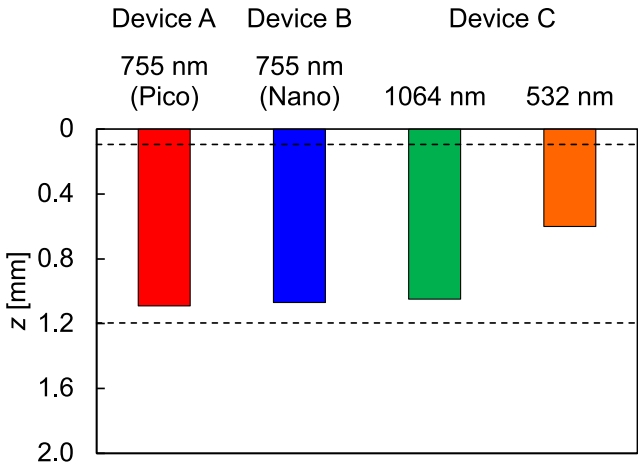


Figure 5.3: Optical penetration depth $\delta$ in the skin model. Figure reproduced from Ref. [22].

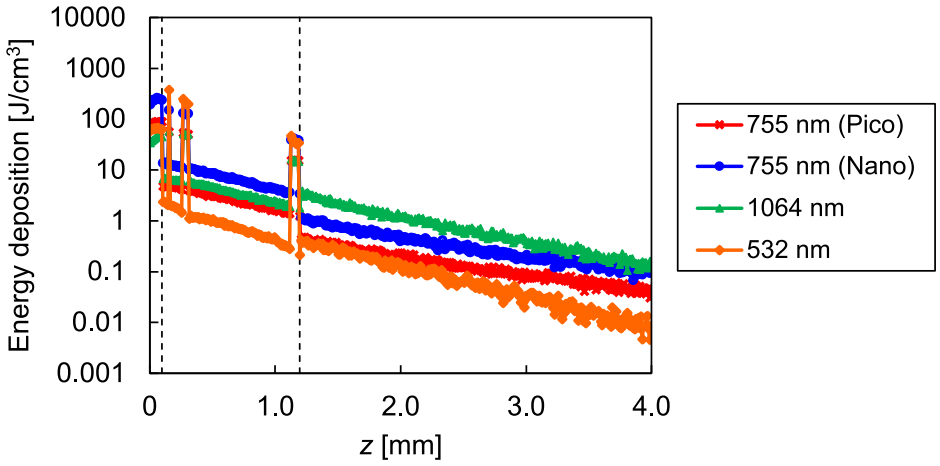


Figure 5.4: Energy deposition profiles in the skin model on the $z$ axis with $x = y = 0$ after laser irradiation under the severe conditions. Figure reproduced from Ref. [22].

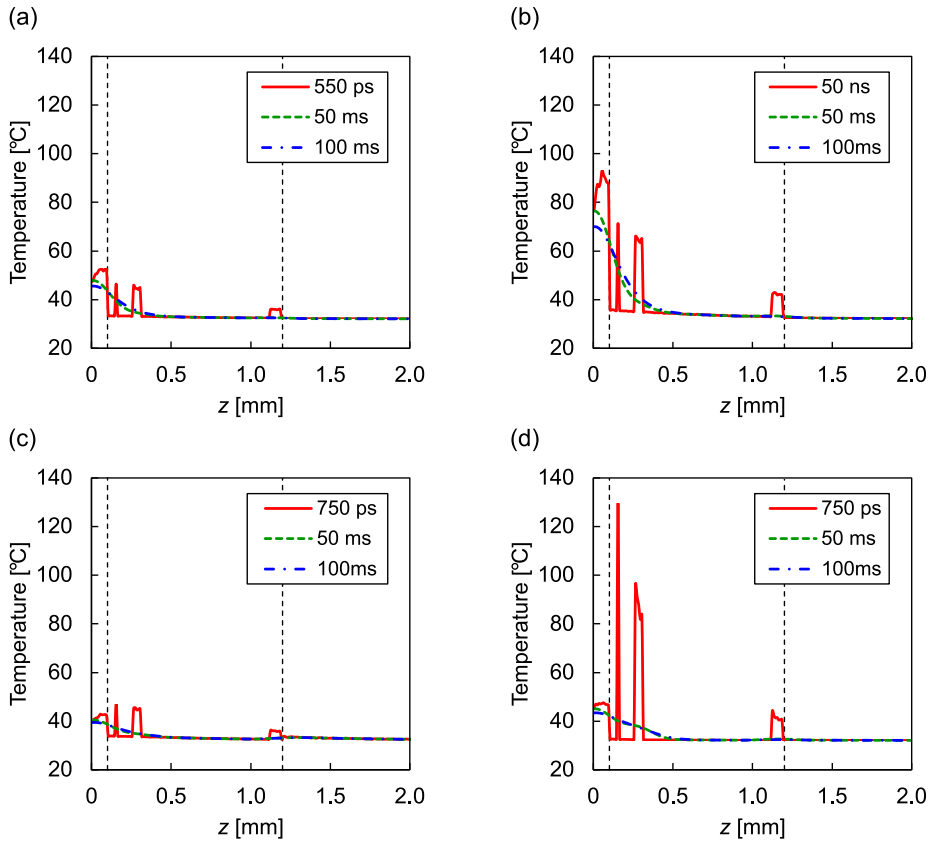


Figure 5.5: Time variations of temperature profiles in the skin model for 100 ms after laser irradiation with (a) Device A (755 nm, 2 mm □, 6.37 J/cm$^2$), (b) Device B (755 nm, 2 mm $\phi$, 18 J/cm$^2$), (c) Device C (1064 nm, 2 mm $\phi$, 10 J/cm$^2$), and (d) Device C (532 nm, 2 mm $\phi$, 2.5 J/cm$^2$) under the severe conditions. Figure reproduced from Ref. [22].

thickness. The $\tau_{\text{thermal}}$ values of epidermis, dermis, and subcutaneous fat were 0.051, 3.6, and 21.3 s, respectively. Because the pulse width was much shorter than $\tau_{\text{thermal}}$, the thermal confinement condition was satisfied. Therefore, fluence had a more pronounced effect on the $T$ than the pulse width. Furthermore, the temperature after 100 ms was kept higher than the initial temperature (Fig. 5.5). The simulation results suggested that the repetition rate of 10 Hz resulted in the accumulation of thermal damage. Continuous pulse irradiation to the same area may cause an excessive temperature rise because of heat accumulation. It may be required to provide a sufficient interval between laser pulses and to cool the skin tissue during operation to reduce thermal damage.

A novel picosecond laser was evaluated based on photothermal damage to normal skin tissue immediately after the laser shot. The computational simulation assumed that all the laser energy was converted into heat to calculate the maximum photothermal damage. Since acute damage was considered in the simulation, the necessary modeling after light absorption by the skin is a temperature rise and thermal damage. The temperature distribution can be computationally reproduced using the heat conduction equation. Furthermore, the use of computational simulations is a standard for evaluating thermal damage because necessary parameters, such as a threshold

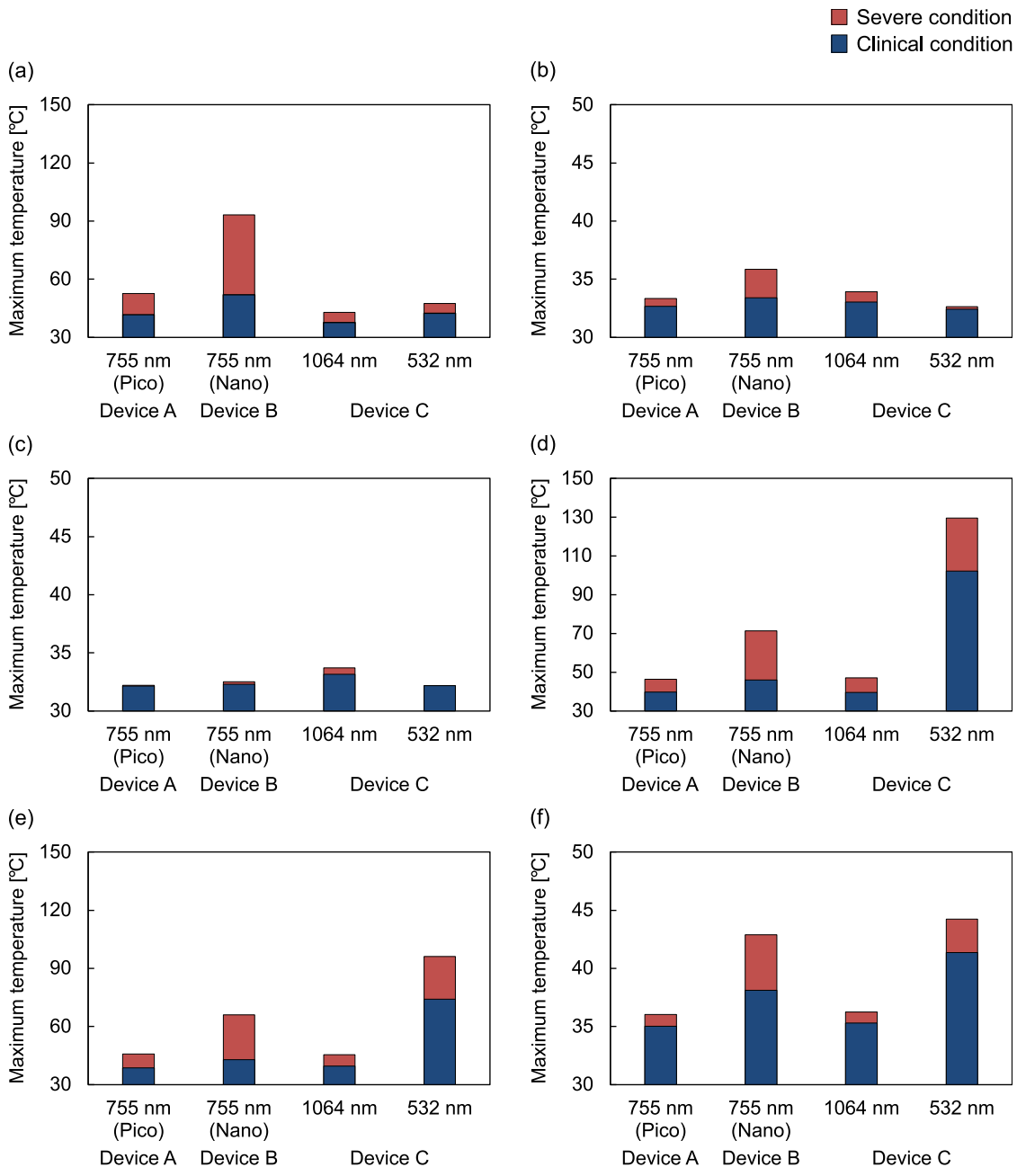


Figure 5.6: Maximum temperature after laser irradiation in (a) epidermis, (b) dermis, (c) capillary vessels, (d) upper dermis vessels, (e) deep dermis vessels, and (f) subcutaneous fat. Figure reproduced from Ref. [22].

for irreversible thermal damage, have already been obtained [37]. Therefore, the evaluation of photothermal damage was achieved by calculating $T$ and $P$. In the light propagation calculation, the MC simulation assumed the linear absorption of picosecond laser. However, picosecond laser can induce nonlinear absorption owing to the high power density, which affects the light distribution in skin tissue [38]. The light transport model considering nonlinear absorption will improve the accuracy of the quantitative evaluation of the effects of picosecond lasers on skin tissue, as described in Chapter 4. For abnormal skin tissues, pigments such as melanosomes and tattoo particles are disrupted by photomechanical effect and cleared by macrophages and other phagocytes [39]. Mathematical models of photomechanical and biological effects will enable computational simulations to quantitatively evaluate the long-term treatment outcome.

The accuracy of the optical and thermal parameters affects the simulation results of photothermal damage. The mathematical model assumed that the dynamics of the optical properties of the skin tissue resulting from the increase in temperature were constant. Several studies reported that $\delta$ becomes shorter when the tissue is coagulated [40–42]. This suggested that the calculated $P$ was estimated to be more severe in deep tissues than in reality. However, $P$ in deep tissues such as the dermis and subcutaneous fat were lower than the threshold. Therefore, the dynamics of the optical properties were negligible in the evaluation of the photothermal skin damage. The $T$ could be overestimated because the cooling effect of blood perfusion was not considered in the thermal diffusion calculation. It is known that the cooling effect resulting from vasculature causes a change in the temperature distribution and reduces the degree of thermal damage [43]. However, the knowledge of physical properties has not been accumulated enough to reproduce the cooling effect by a mathematical model. Experimental analyses will be required to model the cooling effect resulting from blood flow.

The simulation results demonstrated that the photothermal skin damage caused by Device A was less than that caused by Devices B and C. Clinical studies reported that picosecond laser treatment had less or comparable side effects than nanosecond laser treatment [44, 45], confirming that the simulation results were consistent with the clinical study results. Since thermal damage is one of the indicators of safety [46], computational clinical trials could partially replace preclinical and clinical trials. It is desirable to conduct a safety and efficacy evaluation of laser devices with various combinations of parameters, including pulse width, spot size, fluence, and repetition rate. Conventional evaluations of novel laser devices require a time-consuming and expensive process due to the many combinations of irradiation parameters in preclinical trials and the number of subjects required to obtain reliable data in clinical trials [4, 36, 47–51]. Compared to preclinical and clinical trials, computational clinical trials can provide a rapid and low-cost evaluation of laser devices because of the simple operation of setting the parameters on a computer. Furthermore, computational clinical trials investigate laser-tissue interactions by computational modeling and simulation. They provide a quantitative and reproducible evaluation of laser devices. The implementation of computational clinical trials for regulatory evaluations is expected to accelerate the clinical applications of novel laser devices.

## 5.5 Conclusion of this chapter

A computational clinical trial was performed to evaluate the photothermal skin damage induced by a novel picosecond laser device. The $T$ and $P$ of skin tissue between the novel laser device and the approved laser devices were compared by computational simulation, and the photothermal damage caused by the novel device was shown to be less than that caused by the approved laser devices. These results demonstrated that computational laser treatment can be applied to computational clinical trials for the partial replacement of preclinical and clinical trials. The accumulation of clinical data and physical parameters will improve the reliability of computational clinical trials.

## References


[1] M.N. Rylander, R.J. Stafford, J. Hazle, J. Whitney, and K.R. Diller. Heat shock protein expression and temperature distribution in prostate tumours treated with laser irradiation and nanoshells. *International Journal of Hyperthermia*, 27(8):791–801, 2011.

[2] R. Van Den Bos, P. Van Ruijven, C. Van Der Geld, M. Van Gemert, H. Neumann, and T. Nijsten. Endovenous simulated laser experiments at 940 nm and 1470 nm suggest wavelength-independent temperature profiles. *European Journal of Vascular and Endovascular Surgery*, 44(1):77–81, 2012.

[3] J.W. Decorato, B. Chen, and R. Sierra. Subcutaneous adipose tissue response to a non-invasive hyperthermic treatment using a 1,060 nm laser. *Lasers in Surgery and Medicine*, 49(5):480–489, 2017.

[4] E.F. Bernstein, K.T. Schomacker, L.D. Basilavecchio, J.M. Plugis, and J.D. Bhawalkar. A novel dual-wavelength, Nd:YAG, picosecond-domain laser safely and effectively removes multicolor tattoos. *Lasers in Surgery and Medicine*, 47(7):542–548, 2015.

[5] Y. Hashishin. Safety standard and their trend relating to lights and lasers. *Nippon Laser Igakkaishi*, 33(1):27–33, 2012.

[6] T.M. Morrison, P. Pathmanathan, M. Adwan, and E. Margerrison. Advancing regulatory science with computational modeling for medical devices at the FDA's office of science and engineering laboratories. *Frontiers in Medicine*, 5(241):1–11, 2018.

[7] T.M. Morrison, M.L. Dreher, S. Nagaraja, L.M. Angelone, and W. Kainz. The role of computational modeling and simulation in the total product life cycle of peripheral vascular devices. *Journal of Medical Devices*, 11(2):024503, 2017.

[8] I.V. Meglinski and S.J. Matcher. Quantitative assessment of skin layers absorption and skin reflectance spectra simulation in the visible and near-infrared spectral regions. *Physiological Measurement*, 23(4):741–753, 2002.

[9] X. Chen and G.M. Saidel. Modeling of laser coagulation of tissue with MRI temperature monitoring. *Journal of Biomechanical Engineering*, 132(6):064503, 2010.

[10] C.P. Cain, G.D. Polhamus, W.P. Roach, D.J. Stolarski, K.J. Schuster, K. Stockton, B.A. Rockwell, B. Chen, and A.J. Welch. Porcine skin visible lesion thresholds for near-infrared lasers including modeling at two pulse durations and spot sizes. *Journal of Biomedical Optics*, 11(4):041109, 2006.

[11] H. Elkhalil, A. Alshare, G. Shafirstein, and J. Bischof. A three-dimensional transient computational study of 532-nm laser thermal ablation in a geometrical model representing prostate tissue. *International Journal of Hyperthermia*, 35(1):568–577, 2018.

[12] H. Hazama, M. Yoshimori, N. Honda, and K. Awazu. Evaluation of endovenous laser ablation for varicose veins using a computer simulation model (Secondary publication). *Laser Therapy*, 26(4):282–287, 2017.

[13] S.L. Jacques. Coupling 3D Monte Carlo light transport in optically heterogeneous tissues to photoacoustic signal generation. *Photoacoustics*, 2(4):137–142, 2014.

[14] H.H. Pennes. Analysis of tissue and arterial blood temperatures in the resting human forearm. *Journal of Applied Physiology*, 1(2):93–122, 1948.

[15] J.A. Pearce. Relationship between Arrhenius models of thermal damage and the CEM 43 thermal dose. *Proceedings of SPIE*, 7181:718104, 2009.

[16] B. Varghese, V. Bonito, M. Jurna, J. Palero, M. Horton, and R. Verhagen. Influence of absorption induced thermal initiation pathway on irradiance threshold for laser induced breakdown. *Biomedical Optics Express*, 6(4):1234–1240, 2015.

[17] D.K. Yao, C. Zhang, K.I. Maslov, and L.V. Wang. Photoacoustic measurement of the Grüneisen parameter of tissue. *Journal of Biomedical Optics*, 19(1):017007, 2014.

[18] A.A. Oraevsky, S.L. Jacques, and F.K. Tittel. Measurement of tissue optical properties by time-resolved detection of laser-induced transient stress. *Applied Optics*, 36(1):402–415, 1997.

[19] A. Doukas and T. Flotte. Physical characteristics and biological effects of laser-induced stress waves. *Ultrasound in Medicine & Biology*, 22(2):151–164, 1996.

[20] M. Sherar, J. Moriarty, M. Kolios, J. Chen, R. Peters, L. Ang, R. Hinks, R. Henkelman, M. Bronskill, and W. Kucharcyk. Comparison of thermal damage calculated using magnetic resonance thermometry, with magnetic resonance imaging post-treatment and histology, after interstitial microwave thermal therapy of rabbit brain. *Physics in Medicine & Biology*, 45(12):3563–3576, 2000.

[21] D.P. Poppas, R.B. Stewart, J.M. Massicotte, A.E. Wolga, R.T. Kung, A.B. Retik, and M.R. Freeman. Temperature-controlled laser photocoagulation of soft tissue: *In vivo* evaluation using a tissue welding model. *Lasers in Surgery and Medicine*, 18(4):335–344, 1996.

[22] Y. Shimojo, T. Nishimura, H. Hazama, N. Ito, and K. Awazu. Picosecond laser-induced photothermal skin damage evaluation by computational clinical trial. *Laser Therapy*, 29(1):61–72, 2020.

[23] Y. Lee and K. Hwang. Skin thickness of Korean adults. *Surgical and Radiologic Anatomy*, 24(3):183–189, 2002.

[24] S.L. Jacques. Skin optics summary. *Oregon Medical Laser Center News*, 1998.

[25] S.L. Jacques. Optical properties of biological tissues: A review. *Physics in Medicine & Biology*, 58(11):R37–R61, 2013.

[26] G.M. Palmer, C. Zhu, T.M. Breslin, F. Xu, K.W. Gilchrist, and N. Ramanujam. Monte Carlo-based inverse model for calculating tissue optical properties. Part Ⅱ: Application to breast cancer diagnosis. *Applied Optics*, 45(5):1072–1078, 2006.

[27] M. Meinke, G. Müller, J. Helfmann, and M. Friebel. Empirical model functions to calculate hematocrit-dependent optical properties of human blood. *Applied Optics*, 46(10):1742–1753, 2007.

[28] C.R. Simpson, M. Kohl, M. Essenpreis, and M. Cope. Near-infrared optical properties of *ex vivo* human skin and subcutaneous tissues measured using the Monte Carlo inversion technique. *Physics in Medicine & Biology*, 43(9):2465, 1998.

[29] P. Djorev, E.G. Borisova, and L.A. Avramov. Interaction of IR laser radiation with human skin: Monte Carlo simulation. *Proceedings of SPIE*, 5226:403–407, 2003.

[30] M.L. Cohen. Measurement of the thermal properties of human skin. A review. *Journal of Investigative Dermatology*, 69(3):333–338, 1977.

[31] F. Henriques Jr and A.R. Moritz. Studies of thermal injury: I. The conduction of heat to and through skin and the temperatures attained therein. A theoretical and an experimental investigation. *The American Journal of Pathology*, 23(4):530–549, 1947.

[32] F.A. Duck. Thermal Properties of Tissue. In *Physical Properties of Tissues*, pages 9–42. Academic Press, London, UK, 1990.

[33] T. Balasubramaniam and H. Bowman. Thermal conductivity and thermal diffusivity of biomaterials: A simultaneous measurement technique. *Journal of Biomechanical Engineering*, 99(3):148–154, 1977.

[34] N.B. Smith, J.M. Temkin, F. Shapiro, and K. Hynynen. Thermal effects of focused ultrasound energy on bone tissue. *Ultrasound in Medicine & Biology*, 27(10):1427–1433, 2001.

[35] A.J. Welch and M.J. Van Gemert. *Optical-thermal response of laser-irradiated tissue*. 2 edition, 2011.

[36] N. Saedi, A. Metelitsa, K. Petrell, K.A. Arndt, and J.S. Dover. Treatment of tattoos with a picosecond alexandrite laser: A prospective trial. *Archives of Dermatology*, 148(12):1360–1363, 2012.

[37] N.T. Wright. On a relationship between the Arrhenius parameters from thermal damage studies. *Journal of Biomechanical Engineering*, 125(2):300–304, 2003.

[38] D.J. Stolarski, J. Stolarski, R.J. Thomas, G.D. Noojin, K.J. Schuster, and B.A. Rockwell. Nonlinear absorption studies of melanin. *Proceedings of SPIE*, 4617:161–171, 2002.

[39] D.C. Wu, M.P. Goldman, H. Wat, and H.H. Chan. A systematic review of picosecond laser in dermatology: Evidence and recommendations. *Lasers in Surgery and Medicine*, 53(1):9–49, 2021.

[40] N. Honda, K. Ishii, T. Terada, T. Nanjo, and K. Awazu. Determination of the tumor tissue optical properties during and after photodynamic therapy using inverse Monte Carlo method and double integrating sphere between 350 and 1000 nm. *Journal of Biomedical Optics*, 16(5):058003, 2011.

[41] H. Ao, D. Xing, H. Wei, H. Gu, G. Wu, and J. Lu. Thermal coagulation-induced changes of the optical properties of normal and adenomatous human colon tissues *in vitro* in the spectral range 400–1100 nm. *Physics in Medicine & Biology*, 53(8):2197–2206, 2008.

[42] V.K. Nagarajan and B. Yu. Monitoring of tissue optical properties during thermal coagulation of *ex vivo* tissues. *Lasers in Surgery and Medicine*, 48(7):686–694, 2016.

[43] M.C. Kolios, M. Sherar, and J. Hunt. Large blood vessel cooling in heated tissues: A numerical study. *Physics in Medicine & Biology*, 40(4):477–494, 1995.

[44] L. Izikson, W. Farinelli, F. Sakamoto, Z. Tannous, and R.R. Anderson. Safety and effectiveness of black tattoo clearance in a pig model after a single treatment with a novel 758 nm 500 picosecond laser: A pilot study. *Lasers in Surgery and Medicine*, 42(7):640–646, 2010.

[45] W. Yu, J. Zhu, W. Yu, D. Lyu, X. Lin, and Z. Zhang. A split-face, single-blinded, randomized controlled comparison of alexandrite 755-nm picosecond laser versus alexandrite 755-nm nanosecond laser in the treatment of acquired bilateral nevus of Ota-like macules. *Journal of the American Academy of Dermatology*, 79(3):479–486, 2018.

[46] J. Takada, N. Honda, H. Hazama, N. Ioritani, and K. Awazu. Analysis of thermally denatured depth in laser vaporization for benign prostatic hyperplasia using a simulation of light propagation and heat transfer (Secondary publication). *Laser Therapy*, 25(4):273–284, 2016.

[47] E.V. Ross, G. Naseef, C. Lin, M. Kelly, N. Michaud, T.J. Flotte, J. Raythen, and R.R. Anderson. Comparison of responses of tattoos to picosecond and nanosecond Q-switched neodymium:YAG lasers. *Archives of Dermatology*, 134(2):167–171, 1998.

[48] R.M. Herd, M.B. Alora, B. Smoller, K.A. Arndt, and J.S. Dover. A clinical and histologic prospective controlled comparative study of the picosecond titanium: Sapphire (795 nm) laser versus the Q-switched alexandrite (752 nm) laser for removing tattoo pigment. *Journal of the American Academy of Dermatology*, 40(4):603–606, 1999.

[49] J.A. Brauer, K.K. Reddy, R. Anolik, E.T. Weiss, J.K. Karen, E.K. Hale, L.A. Brightman, L. Bernstein, and R.G. Geronemus. Successful and rapid treatment of blue and green tattoo pigment with a novel picosecond laser. *Archives of Dermatology*, 148(7):820–823, 2012.

[50] H. Alabdulrazzaq, J.A. Brauer, Y.S. Bae, and R.G. Geronemus. Clearance of yellow tattoo ink with a novel 532-nm picosecond laser. *Lasers in Surgery and Medicine*, 47(4):285–288, 2015.

[51] S. Au, A.M. Liolios, and M.P. Goldman. Analysis of incidence of bulla formation after tattoo treatment using the combination of the picosecond Alexandrite laser and fractionated $CO_2$ ablation. *Dermatologic Surgery*, 41(2):242–245, 2015.

# Chapter 6

# Incident fluence analysis based on tissue optical properties and threshold fluences for melanosome disruption

## 6.1 Introduction

Picosecond lasers have treatment effects on benign pigmented lesions by selective disruption of melanosomes. In clinical practice, irradiation endpoints are usually determined by a visual assessment of immediate whitening after the laser shot, corresponding to an increase in optical scattering with vacuolization of the melanosomes [1]. Because the determination is highly dependent on the surgeon's skill and experience, adverse events to unintended tissues, such as erythema, blistering, hypopigmentation, and PIH, have been caused by inappropriate settings of the irradiation parameters. In particular, patients with darker skin types have a higher risk of these events [2, 3]. A robust setting of irradiation parameters considering skin type is strongly required for safer treatment.

In picosecond laser treatment, multiple factors, including laser wavelength, pulse width, fluence, spot size, and skin type, contribute to the treatment outcome [4]. To provide a standardized treatment, these irradiation parameters should be optimized to maximize treatment outcomes. Computational modeling and simulation of picosecond laser treatment can provide quantitative information to determine irradiation parameters [5]. In tattoo removal, the minimum incident fluence for treatment was estimated using a computational simulation of light transport and subsequent photothermal and photomechanical effects [6]. However, an evaluation of the effect of skin type on light distribution in picosecond laser treatment has remained lacking. During picosecond laser propagation in the skin, the incident fluence is attenuated by the epidermis and dermis depending on their optical properties [7, 8]. Additionally, because the depth of abnormal melanosomes in the skin varies with the type of pigmented lesions [9–11], the extent to which the incident fluence reaches the target lesions depends on the depth of the lesions. A mathematical model based on

Portions of this chapter were originally published under the title, "Incident fluence analysis for 755-nm picosecond laser treatment of pigmented skin lesions based on threshold fluences for melanosome disruption" by Yu Shimojo, Takahiro Nishimura, Hisanao Hazama, Nobuhisa Ito, and Kunio Awazu in *Lasers in Surgery and Medicine* 53(8):1096–1104 (2021).

the optical properties of the skin and the threshold fluence for melanosome disruption enables computational laser treatment to estimate the incident fluence depending on the patient's skin type and the depth of lesions.

This chapter demonstrates that computational laser treatment can provide numerical indices for setting the irradiation parameters for reproducible laser treatment regardless of the surgeon's skill and experience. Incident fluences for picosecond laser treatment are analyzed using an MC simulation combined with the optical properties of the skin (Chapter 2) and the threshold fluences for melanosome disruption (Chapter 3). The calculated incident fluences are comparatively evaluated between skin types. Because MC simulations can calculate light distribution in skin tissue with high accuracy [12–15], the computational laser treatment allows for the prediction of irradiation parameters for the laser to reach pigmented lesions with minimal damage to the surrounding tissue. The numerical indices obtained can provide guidelines for surgeons to deliver safe and efficacious picosecond laser treatment.

## 6.2 Materials and Methods

### 6.2.1 Theory on incident fluence analysis for picosecond laser treatment

The incident fluence was analyzed at a wavelength of 755 nm, which is available in picosecond laser systems for clinical use. Pigmented lesions such as solar lentigines, nevus of Ota, and ectopic Mongolian spots were located at different depths in the epidermis or dermis. An irradiated laser pulse is attenuated by the epidermis and dermis, depending on their optical properties. The incident fluence $F(\mathbf{r})$ [J/cm$^2$] delivering the threshold fluence to the target melanosomes at position $\mathbf{r}$ is therefore expressed as

$$F(\mathbf{r}) \cdot A \cdot I(\mathbf{r}) \geq H_{\mathrm{th}}, \tag{6.1}$$

where $A$ [cm$^2$] is the laser irradiated area, $I(\mathbf{r})$ [1/cm$^2$] is the relative fluence distribution at position $\mathbf{r}$ depending on the optical properties of the skin, and $H_{\mathrm{th}}$ [J/cm$^2$] is the threshold fluence of a picosecond laser pulse for melanosome disruption, which was set to 2.19 and 2.49 J/cm$^2$ for 550- and 750-ps laser pulses, respectively, from the results in Chapter 3. Here, $A \cdot I(\mathbf{r})$ was defined as the light-propagation efficiency of skin tissue from the irradiated surface to position $\mathbf{r}$, $\alpha(\mathbf{r})$ (unitless quantity), because it indicates the light distribution in skin tissue when a unit of laser fluence is incident over the spot area $A$. Substituting $\alpha(\mathbf{r})$ into Equation 6.1, the following equation was obtained:

$$F(\mathbf{r}) \cdot \alpha(\mathbf{r}) \geq H_{\mathrm{th}}. \tag{6.2}$$

The incident fluences $F(\mathbf{r})$ were calculated using this equation.

### 6.2.2 Numerical human skin tissue model

A numerical model of human skin tissue was constructed to calculate the light distributions depending on skin type, as described in Chapter 2. Figure 6.1 shows the numerical skin model

comprising of the epidermis, dermis, subcutaneous fat layers and three different sized blood vessels in the dermis layer [7]. The model was constructed using 500 × 500 × 400 cubic voxels. The size of each voxel was 10 $\mu$m × 10 $\mu$m × 10 $\mu$m. The depth direction of the model was set as the $z$ axis. The skin surface was set at $z$ = 0 mm. The center of the model on the $xy$ plane was set at ($x$, $y$) = (0 mm, 0 mm). In the model, a melanin layer mimicking pigmented lesions was absent. The incident fluences to provide the threshold for a single melanosome located at a given depth of the skin tissue were calculated, assuming that it absorbs the laser light in the same way as the melanosome in water. To compare the incident fluences between skin types, absorption $\mu_a$ and reduced scattering $\mu_s'$ coefficients, and anisotropy factor $g$ for Caucasian, Asian, and African human skins at a wavelength of 755 nm were input, as listed in Table 6.1 [7]. Melanin in the normal epidermis was simulated to be uniformly distributed in the epidermis. The effect of optical absorption by normal melanin was included in the $\mu_a$ values of the epidermis. The blood oxygen saturation was 96%.

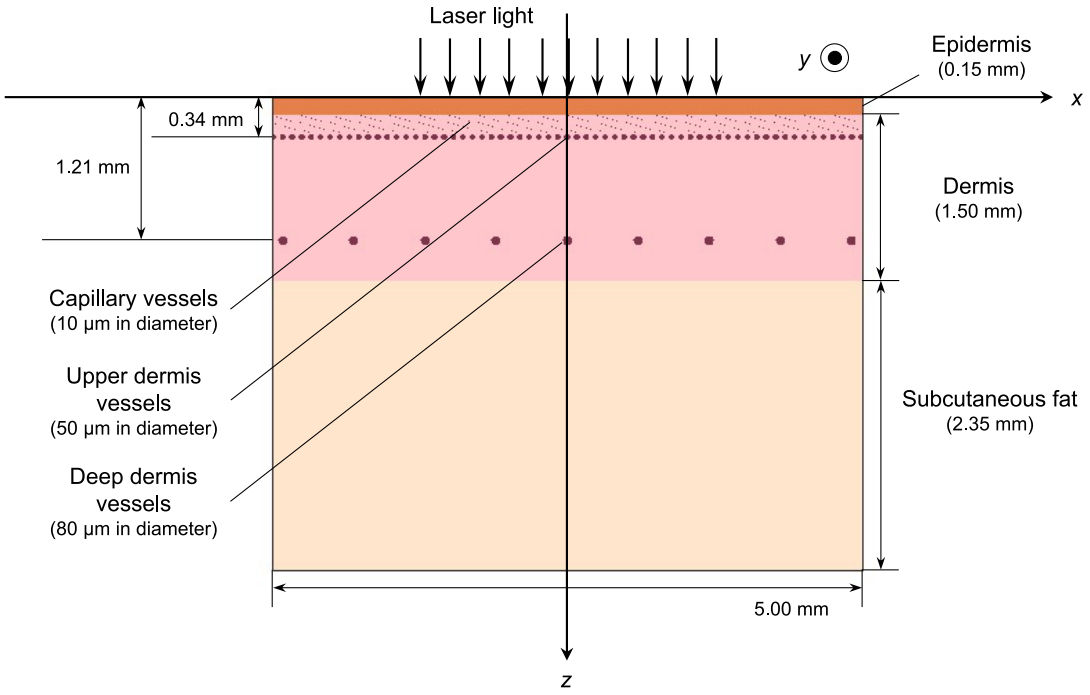


Figure 6.1: Numerical model of human skin geometry consisting of the epidermis, dermis, subcutaneous fat, and three different sized blood vessels (capillary vessels, upper dermis vessels, and deep dermis vessels). Figure reproduced with permission from Ref. [16].

### 6.2.3 MC simulation of light transport in skin tissue

A 3D MC simulation was used to calculate the relative fluence distribution depending on the optical properties of the skin [17]. In this simulation, it was assumed that a rectangular temporal laser pulse was vertically irradiated at the center of the skin surface [18, 19]. The largest $\mu_a$ value in the skin model was 4.9 cm$^{-1}$ (see Table 6.1) and the maximum power density was calculated as 9.6

Table 6.1: Absorption $\mu_a$ and reduced scattering $\mu_s'$ coefficients, and anisotropy factor $g$ of the epidermis, dermis, subcutaneous fat, and blood at a wavelength of 755 nm.

| | Epidermis | Dermis | Subcutaneous fat | Blood |
|---|---|---|---|---|
| **Caucasian** | | | | |
| $\mu_a$ [mm$^{-1}$] | 0.24 | 0.05 ± 0.01 | 0.04 ± 0.02 | 0.32 |
| $\mu_s'$ [mm$^{-1}$] | 4.28 ± 1.04 | 2.20 ± 0.43 | 1.43 ± 0.22 | 1.68 |
| $g$ [-] | | 0.9 | | |
| **Asian** | | | | |
| $\mu_a$ [mm$^{-1}$] | 0.49 ± 0.19 | 0.05 ± 0.01 | 0.04 ± 0.02 | 0.32 |
| $\mu_s'$ [mm$^{-1}$] | 4.28 ± 1.04 | 2.20 ± 0.43 | 1.43 ± 0.22 | 1.68 |
| $g$ [-] | | 0.9 | | |
| **African** | | | | |
| $\mu_a$ [mm$^{-1}$] | 2.98 | 0.05 ± 0.01 | 0.04 ± 0.02 | 0.32 |
| $\mu_s'$ [mm$^{-1}$] | 4.28 ± 1.04 | 2.20 ± 0.43 | 1.43 ± 0.22 | 1.68 |
| $g$ [-] | | 0.9 | | |

GW/cm$^2$ by dividing the fluence by the pulse width [20, 21]. The maximum power density was two orders of magnitude lower than the threshold irradiance for the nonlinear excitation condition of the skin tissue [22]. The nonlinear absorption induced by picosecond laser irradiation was negligible. The simulation was carried out for 180 million photons to achieve sufficient relative fluence distributions in skin tissue.

## 6.3 Results

### 6.3.1 Light-propagation efficiency

Figure 6.2 shows the light-propagation efficiencies $\alpha$ of Asian skin tissue at spot sizes of 2, 3, and 4 mm. The $\alpha$ tended to decrease with increasing depth. The maximum and minimum dispersions of $\alpha$ were estimated using the SDs of the $\mu_a$ and $\mu_s'$ values of each tissue, which were derived from individual and body-site differences [7]. The maximum $\alpha$ was obtained from the minimum $\mu_a$ and $\mu_s'$ values (mean − 1 SD), while the minimum $\alpha$ was obtained from the maximum $\mu_a$ and $\mu_s'$ values (mean + 1 SD). The laser pulse entering the skin tissue propagated radially (Fig. 6.2(i)). The $\alpha$ increased near the dermal-epidermal junction owing to the backscattering (Fig. 6.2(ii)).

### 6.3.2 Incident fluence of picosecond laser for Asian skin

The incident fluences for the disruption of melanosomes located at different depths in Asian skin were obtained using Equation 6.2. Figure 6.3 shows the incident fluences of 550- and 750-ps laser pulses for melanosome disruption in the skin when the spot size is 2, 3, and 4 mm. The incident fluences increased with increasing depth of the target melanosomes. The deviation of the incident fluences increased as the target melanosomes were deeply located owing to the deviation of $\alpha$. Because $\alpha$ increased near the dermal-epidermal junction, the incident fluences were found to decrease at its depth. Figure 6.4 shows the detailed comparison of incident fluence focusing

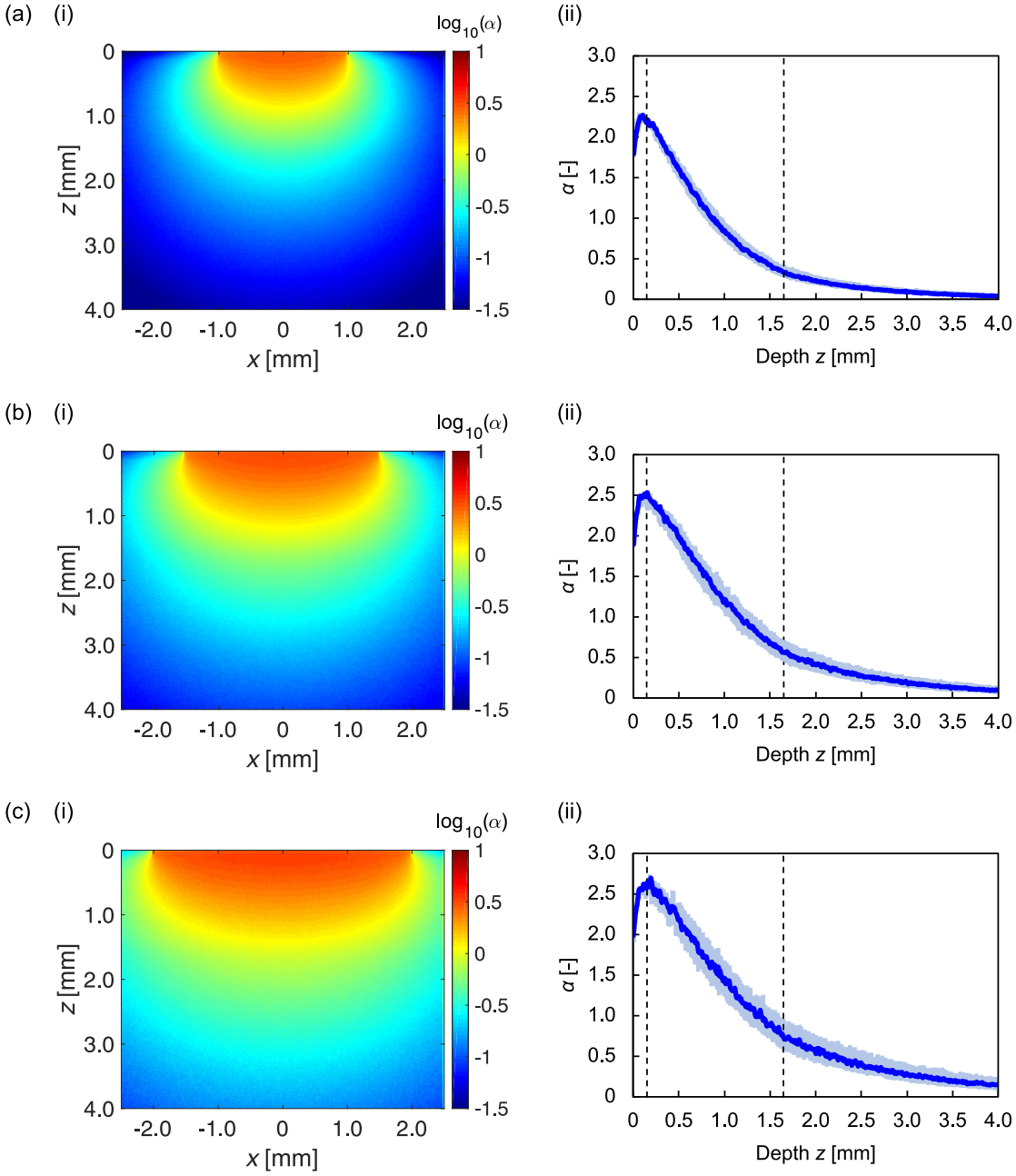


Figure 6.2: Light-propagation efficiencies $\alpha$ calculated with MC simulation for square spots of (a) 2, (b) 3, and (c) 4 mm. (i) Spatial distributions on the $zx$ plane and (ii) depth profiles along the $z$ axis with $x = y = 0$. The broken lines at 0.15 and 1.65 mm exhibit the boundaries between the epidermis and dermis, and between the dermis and subcutaneous fat, respectively. Figure reproduced with permission from Ref. [16].

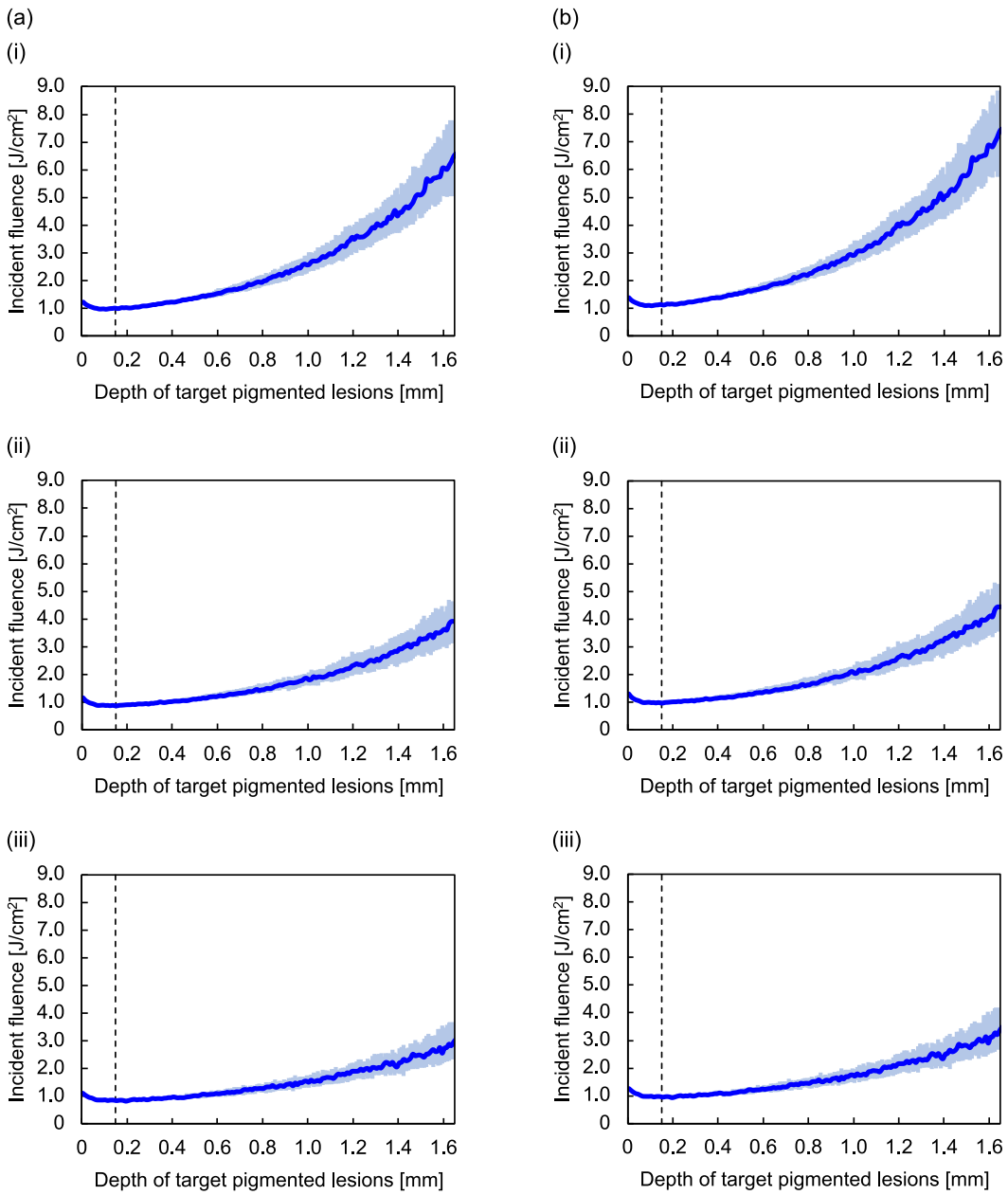


Figure 6.3: Incident fluences $F$ of (a) 550- and (b) 750-ps laser pulses for disruption of melanosomes with different depth distributions in skin tissue calculated at square spots of (i) 2, (ii) 3, and (iii) 4 mm. The broken lines at 0.15 mm exhibit the boundary between the epidermis and dermis. The depth range of subcutaneous fat is not shown since pigmented lesions are located in the epidermis and dermis. Figure reproduced with permission from Ref. [16].

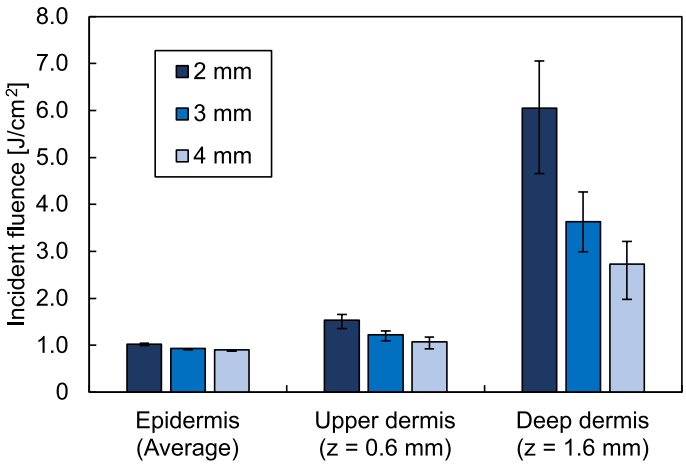


Figure 6.4: Comparison of incident fluences between different sizes of a circular spot in the epidermis, upper dermis, and deeper dermis. The irradiation parameters were a wavelength of 755 nm and a pulse width of 550 ps.

on spot size. Differences in incident fluence between the epidermis and the deep dermis were observed for spot sizes of 2, 3, and 4 mm: 5.0, 2.7, and 1.8 J/cm$^2$ for a 550-ps laser pulse and 5.7, 3.1, and 2.1 J/cm$^2$ for a 750-ps laser pulse. In the deep dermis, increasing the spot size from 2 mm to 4 mm reduced the incident fluence by 55%.

### 6.3.3 Comparison between different skin types

Figure 6.5 shows the comparison of the incident fluences between Caucasian, Asian, and African skins. The pulse width was 550 ps and the spot size was 3 mm. The incident fluences for epidermal lesions were 0.67, 0.74, and 1.52 J/cm$^2$ while those for deep dermal lesions were 3.21, 3.49, and 6.76 J/cm$^2$ for Caucasian, Asian, and African skins, respectively. The incident fluences for Asian skin were similar to those for Caucasian skin and approximately half those for African skin due to a lower concentration of melanin in the epidermis.

## 6.4 Discussion

The lesion depth-dependent incident fluences of picosecond laser were calculated taking into account the skin type. The simulation results for Asian skin were consistent with those reported for picosecond laser treatment of dermal pigmented lesions using the same laser device as in our experiment [23–25]. Clinical studies reported that patients with Fitzpatrick skin type Ⅲ or Ⅳ who suffer from nevus of Ota, Hori's macules, or ectopic Mongolian spots obtained good results without any complications through picosecond laser irradiation at a pulse width of 750 ps, fluences of 1.59–5.26 J/cm$^2$, and spot sizes of 2.2–4.0 mm. The incident fluences calculated for spot sizes of 3 and 4 mm were within the range of the reported incident fluences when the target melanosomes were located in the dermis. The simulation results revealed that the incident fluences necessary for melanosome disruption in skin tissue differ when melanosomes are located in the

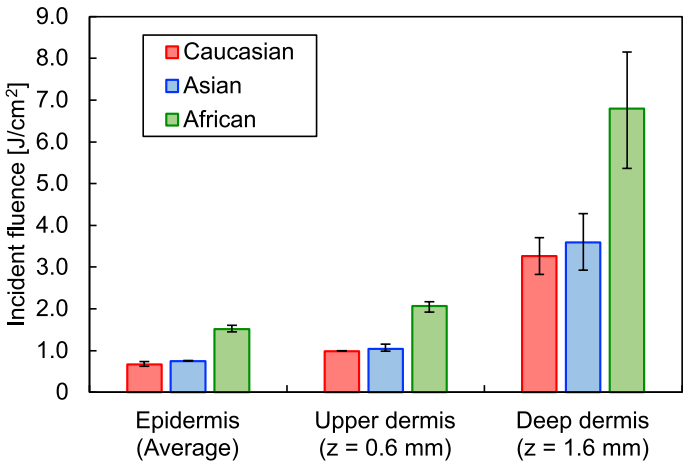


Figure 6.5: Comparison of incident fluences between different skin types in the epidermis, upper dermis, and deeper dermis. The irradiation parameters were a wavelength of 755 nm, a pulse width of 550 ps, and a circular spot of 3 mm.

epidermis and deep dermis, and the larger the spot size, the lower the incident fluence required to disrupt melanosomes in deeper skin tissue (Fig. 6.3). These results have an important clinical implication in demonstrating that the appropriate choice of irradiation parameters depends on the depth of pigmented lesions. In a clinical study of 755-nm picosecond laser treatment of epidermal pigmented lesions in Asians, a fluence of 3.5 J/cm$^2$ gave rise to marginal hyperpigmentation [26]. In contrast, the results indicated that a fluence of 1 J/cm$^2$ of picosecond laser could be capable of treating epidermal pigmented lesions with less damage to the surrounding tissues. Figure 6.3 also shows a slight decrease in the incident fluences when the target melanosomes were around the dermal-epidermal junction. Because a laser wavelength of 755 nm, employed for picosecond laser devices, penetrates deeply into skin tissue and has a large ratio of optical absorption by melanin relative to hemoglobin [7, 27], the laser light is suitable for the treatment of dermal pigmented lesions [28–30]. The simulation results suggested that even if the appropriate incident fluences are chosen to disrupt melanosomes in the dermis layer, an unavoidable injury at the junction may occur, often involving PIH or hypopigmentation [25, 31]. The design of a novel optical delivery system that allows a sufficient amount of laser energy to reach the deep layer of skin tissue while reducing damage to the surface layer is required [32].

When short-pulsed laser energy is directed at pigmented skin lesions, an irradiation endpoint is usually immediate whitening [33–35]. However, Ohshiro *et al.* [25] reported that patients with dermal pigmented lesions obtained successful lightning without immediate whitening in 12 of 16 treatments, suggesting that immediate whitening is not needed to achieve clinical clearance in picosecond laser treatment. Furthermore, immediate whitening can also occur in melanosomes in normal tissues located above pigmented lesions, making it difficult to distinguish them from the melanosomes in pigmented lesions. The determination through a visual assessment is therefore difficult if the desired energy is delivered to the target lesions. These contradictions suggest the need for a quantitative evaluation of irradiation parameters for the treatment of pigmented lesions.

The calculated incident fluences can provide fundamental knowledge to establish numerical indices for determining distinct irradiation endpoints of picosecond laser. Because the optical properties of the tissue and the depth of the lesions can be measured, the validation of the simulation results will lead to the design of a treatment protocol tailored to a patient.

## 6.5 Conclusion of this chapter

The light transport simulation revealed that the appropriate incident fluences of picosecond laser for pigmented lesions depend on the skin type and the depth of the lesions. The incident fluences for Asian skin were similar to those for Caucasian skin while approximately half those for African skin. Choosing a larger spot size can disrupt melanosomes in deeper tissue with minimal collateral damage because a lesser incident fluence is necessary. These results demonstrated that computational laser treatment can provide numerical indices for determining distinct irradiation endpoints. These indices will contribute to designing a treatment protocol tailored to the optical properties of a patient and developing novel laser devices.

## References


[1] M. Wanner, F.H. Sakamoto, M.M. Avram, H.H. Chan, M. Alam, Z. Tannous, and R.R. Anderson. Immediate skin responses to laser and light treatments: Therapeutic endpoints: How to obtain efficacy. *Journal of the American Academy of Dermatology*, 74(5):821–833, 2016.

[2] T. Kono, S.Y. Shek, H.H. Chan, W.F. Groff, K. Imagawa, and T. Akamatsu. Theoretical review of the treatment of pigmented lesions in Asian skin. *Laser Therapy*, 25(3):179–184, 2016.

[3] C.C. Wang, Y.M. Sue, C.H. Yang, and C.K. Chen. A comparison of Q-switched alexandrite laser and intense pulsed light for the treatment of freckles and lentigines in Asian persons: A randomized, physician-blinded, split-face comparative trial. *Journal of the American Academy of Dermatology*, 54(5):804–810, 2006.

[4] D.C. Wu, M.P. Goldman, H. Wat, and H.H. Chan. A systematic review of picosecond laser in dermatology: Evidence and recommendations. *Lasers in Surgery and Medicine*, 53(1):9–49, 2021.

[5] J. Tian, B. Chen, and D. Li. Efficacy evaluation and treatment parameter optimization for laser surgery of Ota's nevus based on an advanced non-equilibrium bio-tissue heat transfer model. *Lasers in Medical Science*, 37(1):369–379, 2022.

[6] D.D.M. Ho, R. London, G.B. Zimmerman, and D.A. Young. Laser-tattoo removal—a study of the mechanism and the optimal treatment strategy via computer simulations. *Lasers in Surgery and Medicine*, 30(5):389–397, 2002.

[7] Y. Shimojo, T. Nishimura, H. Hazama, T. Ozawa, and K. Awazu. Measurement of absorption and reduced scattering coefficients in Asian human epidermis, dermis, and subcutaneous fat tissues in the 400- to 1100-nm wavelength range for optical penetration depth and energy deposition analysis. *Journal of Biomedical Optics*, 25(4):045002, 2020.

[8] E.V. Salomatina, B. Jiang, J. Novak, and A.N. Yaroslavsky. Optical properties of normal and cancerous human skin in the visible and near-infrared spectral range. *Journal of Biomedical Optics*, 11(6):064026, 2006.

[9] S. Watanabe and H. Takahashi. Treatment of nevus of Ota with the Q-switched ruby laser. *New England Journal of Medicine*, 331(26):1745–1750, 1994.

[10] K. Negishi, H. Akita, and Y. Matsunaga. Prospective study of removing solar lentigines in Asians using a novel dual-wavelength and dual-pulse width picosecond laser. *Lasers in Surgery and Medicine*, 50(8):851–858, 2018.

[11] K.Y. Kung, S.Y.N. Shek, C.K. Yeung, and H.H.L. Chan. Evaluation of the safety and efficacy of the dual wavelength picosecond laser for the treatment of benign pigmented lesions in Asians. *Lasers in Surgery and Medicine*, 51(1):14–22, 2019.

[12] S. Flock, M. Patterson, B. Wilson, and D. Wyman. Monte Carlo modeling of light propagation in highly scattering tissues. I. Model predictions and comparison with diffusion theory. *IEEE Transactions on Biomedical Engineering*, 36(12):1162–1168, 1989.

[13] I. Meglinski and S. Matcher. Computer simulation of the skin reflectance spectra. *Computer Methods and Programs in Biomedicine*, 70(2):179–186, 2003.

[14] C. Zhu and Q. Liu. Review of Monte Carlo modeling of light transport in tissues. *Journal of Biomedical Optics*, 18(5):050902, 2013.

[15] V. Periyasamy and M. Pramanik. Advances in Monte Carlo simulation for light propagation in tissue. *IEEE Reviews in Biomedical Engineering*, 10:122–135, 2017.

[16] Y. Shimojo, T. Nishimura, H. Hazama, N. Ito, and K. Awazu. Incident fluence analysis for 755-nm picosecond laser treatment of pigmented skin lesions based on threshold fluences for melanosome disruption. *Lasers in Surgery and Medicine*, 53(8):1096–1104, 2021.

[17] S.L. Jacques. Coupling 3D Monte Carlo light transport in optically heterogeneous tissues to photoacoustic signal generation. *Photoacoustics*, 2(4):137–142, 2014.

[18] C.C. Handapangoda, M. Premaratne, L. Yeo, and J. Friend. Laguerre Runge–Kutta–Fehlberg method for simulating laser pulse propagation in biological tissue. *IEEE Journal of Selected Topics in Quantum Electronics*, 14(1):105–112, 2008.

[19] K. Mitra and S. Kumar. Development and comparison of models for light-pulse transport through scattering–absorbing media. *Applied Optics*, 38(1):188–196, 1999.

[20] K. Suthamjariya, W.A. Farinelli, W. Koh, and R.R. Anderson. Mechanisms of microvascular response to laser pulses. *Journal of Investigative Dermatology*, 122(2):518–525, 2004.

[21] O. Ekici, R. Harrison, N. Durr, D. Eversole, M. Lee, and A. Ben-Yakar. Thermal analysis of gold nanorods heated with femtosecond laser pulses. *Journal of Physics D: Applied Physics*, 41(18):185501, 2008.

[22] B. Varghese, V. Bonito, M. Jurna, J. Palero, M. Horton, and R. Verhagen. Influence of absorption induced thermal initiation pathway on irradiance threshold for laser induced breakdown. *Biomedical Optics Express*, 6(4):1234–1240, 2015.

[23] C. Chesnut, J. Diehl, and G. Lask. Treatment of nevus of Ota with a picosecond 755-nm alexandrite laser. *Dermatologic Surgery*, 41(4):508–510, 2015.

[24] J.C.Y. Chan, S.Y.N. Shek, T. Kono, C.K. Yeung, and H.H.L. Chan. A retrospective analysis on the management of pigmented lesions using a picosecond 755-nm alexandrite laser in Asians. *Lasers in Surgery and Medicine*, 48(1):23–29, 2016.

[25] T. Ohshiro, T. Ohshiro, K. Sasaki, and K. Kishi. Picosecond pulse duration laser treatment for dermal melanocytosis in Asians: A retrospective review. *Laser Therapy*, 25(2):99–104, 2016.

[26] K. Kasai. Picosecond laser treatment for tattoos and benign cutaneous pigmented lesions (Secondary publication). *Laser Therapy*, 26(4):274–281, 2017.

[27] S.L. Jacques. Skin optics summary. *Oregon Medical Laser Center News*, 1998.

[28] H.H. Chan, R.S.C. Leung, S.Y. Ying, C.F. Lai, T. Kono, J.K.H. Chua, and W.S. Ho. A retrospective analysis of complications in the treatment of nevus of Ota with the Q-switched alexandrite and Q-switched Nd:YAG Lasers. *Dermatologic Surgery*, 26(11):1000–1006, 2000.

[29] Y. Ge, Y. Yang, L. Guo, M. Zhang, Q. Wu, R. Zeng, H. Rong, G. Jia, H. Shi, J. Fang, and T. Lin. Comparison of a picosecond alexandrite laser versus a Q-switched alexandrite laser for the treatment of nevus of Ota: A randomized, split-lesion, controlled trial. *Journal of the American Academy of Dermatology*, 83(2):397–403, 2020.

[30] S. Hu, C.S. Yang, S.L. Chang, Y.L. Huang, Y.F. Lin, and M.C. Lee. Efficacy and safety of the picosecond 755-nm alexandrite laser for treatment of dermal pigmentation in Asians—a retrospective study. *Lasers in Medical Science*, 35(6):1377–1383, 2020.

[31] R. Sakio, T. Ohshiro, K. Sasaki, and T. Ohshiro. Usefulness of picosecond pulse alexandrite laser treatment for nevus of Ota. *Laser Therapy*, 27(4):251–255, 2018.

[32] J.M. Burns, W. Jia, J.S. Nelson, B. Majaron, and B. Anvari. Photothermal treatment of port-wine stains using erythrocyte-derived particles doped with indocyanine green: A theoretical study. *Journal of Biomedical Optics*, 23(12):121616, 2018.

[33] L.L. Polla, R.J. Margolis, J.S. Dover, D. Whitaker, G.F. Murphy, S.L. Jacques, and R.R. Anderson. Melanosomes are a primary target of Q-switch ruby laser irradiation in guinea pig skin. *Journal of Investigative Dermatology*, 89(3):281–286, 1987.

[34] R.R. Anderson, R.J. Margolis, S. Watenabe, T. Flotte, G.J. Hruza, and J.S. Dover. Selective photothermolysis of cutaneous pigmentation by Q-switched Nd:YAG laser pulses at 1064, 532, and 355 nm. *Journal of Investigative Dermatology*, 93(1):28–32, 1989.

[35] C.R. Taylor and R.R. Anderson. Treatment of benign pigmented epidermal lesions by Q-switched ruby laser. *International Journal of Dermatology*, 32(12):908–912, 1993.

# Chapter 7

# Prospects of computational laser treatment

This study has developed a computational laser treatment based on the experimental and computational analyses of picosecond laser-skin interactions at the tissue, cellular, and molecular scales. The obtained optical properties of Asian skin tissues have enabled computational simulations to calculate light distribution in human skin and provide quantitative data that are difficult to obtain in preclinical and clinical experiments. Furthermore, threshold fluences for melanosome disruption have been determined, and the involvement of nonlinear absorption by melanin in this process has been elucidated. The constructed mathematical models have provided a quantitative evaluation of the difference in treatment effect between picosecond and nanosecond lasers. The computational laser treatment based on the mathematical models and the physical parameters has demonstrated the computational clinical trial from a perspective of photothermal damage and the design of numerical indices for setting the irradiation parameters. Based on these results, this chapter will discuss the prospects of the impacts of computational laser treatment on the processes of device development through regulatory evaluation to clinical use in the field of laser medicine.

Computational laser treatment can provide insights into the development of novel laser devices. Chapters 2 to 4 have revealed changes in light distribution in skin, melanosomes, and melanin for various combinations of irradiation parameters through computational simulations. Because the light distribution significantly affects the treatment effect, the comprehensive evaluation of irradiation parameters is expected to allow for the prediction of the range of laser device settings necessary for treatment effects. Currently, optimal irradiation parameters have not necessarily been employed in laser devices despite the recent advances in laser technology (the expansion of laser wavelengths and pulse widths and the increase in laser output power), because lasers have historically been applied clinically in the order of successful oscillation. Computational laser treatment can reform the current situation and promote the development and evaluation of laser devices with a new framework in which laser device specifications are determined based on the predictions of treatment outcomes from computational simulations, and then laser devices are developed.

Computational laser treatment also provides clues to create the principle of a less invasive laser

treatment than current laser treatments. The principle of current laser treatments has provided safe and efficacious treatment using laser wavelengths with a large difference in optical absorption between diseased and normal tissues. However, because the irradiated laser light undergoes multiple scattering in tissue, the diffused laser light causes unavoidable absorption by normal tissue, resulting in adverse events. The results in Chapter 6 have shown that even when the irradiation parameters are chosen based on the developed numerical indices, it could be difficult to avoid damage to superficial normal tissues when deep lesions are treated. This indicates a limitation of current laser treatments based on wavelength selectivity in the treatment of deep lesions. Multiphoton absorption-based NIR femtosecond laser treatment has been developed to address the problem, but the applicable depth is limited to <0.4 $\mu$m [1], which is insufficient for the treatment of pigmented lesions. Recent advances in optical devices, such as spatial light modulators, have allowed the compensation for optical scattering in the diffusive regime by wavefront shaping [2–4]. Coagulation and vaporization will be confined to lesions by designing light distribution in tissue using computational laser treatment. When the designed irradiation parameters are evaluated with the maximum permissible exposure, it is expected that a truly lesion-selective laser treatment that is noninvasive to normal tissue can be achieved.

Computational laser treatment can be a promising platform for computational clinical trials of novel laser devices, as shown by the results in Chapter 5. With the increase in economic and time burdens of preclinical and clinical trials, laser treatment simulations offer medical device industries a means of reducing development costs and time to market [5, 6]. Computational modeling and simulation allow for the rapid evaluation of the performance of laser devices, the safety and efficacy of laser treatment, and the patient-selection criteria through relatively low-cost simulation. Therefore, they are poised to augment and partially replace device developments and traditional preclinical and clinical trials. Moreover, regulators and administrators are increasingly accepting of the incorporation of computational simulations into the evaluation of medical devices [7, 8]. In 2016, the FDA Center for Devices and Radiological Health published "Reporting of Computational Modeling Studies in Medical Device Submissions" to provide guidance on the utilization of computational simulations in preclinical trials to support medical device applications [9]. In Japan, the Japan Agency for Medical Research and Development published "Development Guideline on *in silico* Evaluation 2019 (Guidance)" in 2019 to provide a guideline regarding *in silico* evaluation for medical devices [10]. Furthermore, the PMDA Scientific Committee released "Report of the Expert Group on the Approach to the Review of Medical Device Software Using Computer Simulation" in 2021, which describes an approach to applying computational simulations to the evaluation of medical devices [11]. These reports from the FDA and the PMDA indicate the growing importance of computational simulations as an evaluation method for medical devices.

Computational laser treatment has shown that the irradiation parameters, including pulse width, fluence, and spot size, can be optimized based on quantitative analysis of laser-skin interactions, in contrast to the current laser treatment, which relies on the surgeon's experience and skill. The numerical indices obtained have already been deployed in clinical studies [12, 13], thus contributing to the standardization of the setting of the irradiation parameters and the improvement of the

surgeon's technique. Such numerical indices can be applied to the treatment of vascular lesions [14], tattoos [15], and melanoma [16] because the principle of laser treatment is similar to that of pigmented lesions. Recently, noninvasive measurements, such as optical coherence tomography [17] and photoacoustic tomography [18], have allowed the spatial distribution of pigmented lesions to be measured. Furthermore, the robot-assisted technique has allowed precisely targeted laser irradiation [19, 20]. Integrating the optical measurements of a patient and the robot-assisted technique into mathematical models of laser treatment will enable the design of a treatment protocol tailored to a patient and precise laser irradiation based on the designed protocol. Future development of laser devices equipped with observation and control systems will be needed.

Although simulations have become prevalent in laser treatment, there are still many barriers to their widespread use. Applications of computational laser treatment are currently targeted at predicting immediate reactions to laser irradiation, such as photothermal and photomechanical effects. However, the primary interest of dermatologists and plastic surgeons is not only the immediate response of the patient after the procedure but also how the patient's skin will respond in the long term. This limitation of computational laser treatment poses a challenge for pathological and immunological simulations, such as macrophage phagocytosis. Computational laser treatments are still in the early stages and require further development of theory, as skin responses are built based on rule-based phenomenological models [5, 21, 22]. The ability to predict how the skin will recover in response to laser treatment is essential for making long-term predictions related to subsequent treatment interventions and will greatly expand the applicability of computational simulations in laser treatment.

## References


[1] Y. Huang, Z. Wu, H. Lui, J. Zhao, S. Xie, and H. Zeng. Precise closure of single blood vessels via multiphoton absorption–based photothermolysis. *Science Advances*, 5(5):eaan9388, 2019.

[2] R. Horstmeyer, H. Ruan, and C. Yang. Guidestar-assisted wavefront-shaping methods for focusing light into biological tissue. *Nature Photonics*, 9(9):563–571, 2015.

[3] P. Lai, L. Wang, J.W. Tay, and L.V. Wang. Photoacoustically guided wavefront shaping for enhanced optical focusing in scattering media. *Nature Photonics*, 9(2):126–132, 2015.

[4] Z. Qin, Z. She, C. Chen, W. Wu, J.K. Lau, N.Y. Ip, and J.Y. Qu. Deep tissue multi-photon imaging using adaptive optics with direct focus sensing and shaping. *Nature Biotechnology*, 40(11):1663–1671, 2022.

[5] Y. Shimojo, T. Nishimura, H. Hazama, N. Ito, and K. Awazu. Picosecond laser-induced photothermal skin damage evaluation by computational clinical trial. *Laser Therapy*, 29(1):61–72, 2020.

[6] S.A. Niederer, J. Lumens, and N.A. Trayanova. Computational models in cardiology. *Nature Reviews Cardiology*, 16(2):100–111, 2019.

[7] O. Inan, P. Tenaerts, S. Prindiville, H. Reynolds, D. Dizon, K. Cooper-Arnold, M. Turakhia, M. Pletcher, K. Preston, H. Krumholz, and others. Digitizing clinical trials. *npj Digital Medicine*, 3(1):1–7, 2020.

[8] M. Viceconti, F. Pappalardo, B. Rodriguez, M. Horner, J. Bischoff, and F.M. Tshinanu. *In silico* trials: Verification, validation and uncertainty quantification of predictive models used in the regulatory evaluation of biomedical products. *Methods*, 185:120–127, 2021.

[9] Reporting of Computational Modeling Studies in Medical Device Submissions, 2016. https://www.fda.gov/regulatory-information/search-fda-guidance-documents/reporting-computational-modeling-studies-medical-device-submissions, Accessed on November 6, 2022.

[10] *in silico*評価に関する開発ガイドライン2019 (手引き), 2019. https://db.bioip-lab.org/guidelines/49, Accessed on November 6, 2022.

[11] コンピューターシミュレーションを活用した医療機器ソフトウエアの審査の考え方に関する専門部会報告書, 2021. https://www.pmda.go.jp/rs-std-jp/outline/0003.html, Accessed on November 6, 2022.

[12] 河野 太郎. ピコ秒レーザーによる色素性病変の治療戦略. 日本レーザー医学会誌, 43(3):182, 2022.

[13] 奥 謙太郎. ピコ秒アレキサンドライトレーザーの良性色素性疾患に対する効果と長期経過. 日本レーザー医学会誌, 42(3):167, 2021.

[14] J.M. Burns, W. Jia, J.S. Nelson, B. Majaron, and B. Anvari. Photothermal treatment of port-wine stains using erythrocyte-derived particles doped with indocyanine green: A theoretical study. *Journal of Biomedical Optics*, 23(12):121616, 2018.

[15] E.F. Bernstein, K.T. Schomacker, L.D. Basilavecchio, J.M. Plugis, and J.D. Bhawalkar. A novel dual-wavelength, Nd:YAG, picosecond-domain laser safely and effectively removes multicolor tattoos. *Lasers in Surgery and Medicine*, 47(7):542–548, 2015.

[16] Y. He, L. Wang, J. Shi, J. Yao, L. Li, R. Zhang, C.H. Huang, J. Zou, and L.V. Wang. *In vivo* label-free photoacoustic flow cytography and on-the-spot laser killing of single circulating melanoma cells. *Scientific Reports*, 6(1):1–8, 2016.

[17] T.C.M.P. Blumetti, M.P. Cohen, E.E. Gomes, M.P. De Macedo, de M.D.F. Souza Begnami, J.H.T.G. Fregnani, J.P. Duprat, G. Pellacani, and G.G. Rezze. Optical coherence tomography (OCT) features of nevi and melanomas and their association with intraepidermal or dermal involvement: A pilot study. *Journal of the American Academy of Dermatology*, 73(2):315–317, 2015.

[18] Y. Zhou, S.V. Tripathi, I. Rosman, J. Ma, P. Hai, G.P. Linette, M.L. Council, R.C. Fields, L.V. Wang, and L.A. Cornelius. Noninvasive determination of melanoma depth using a handheld photoacoustic probe. *The Journal of Investigative Dermatology*, 137(6):1370–1372, 2017.

[19] P.A. York, R. Peña, D. Kent, and R.J. Wood. Microrobotic laser steering for minimally invasive surgery. *Science Robotics*, 6(50):eabd5476, 2021.

[20] W.A. Ross, W.M. Hill, K.B. Hoang, A.S. Laarakker, B.P. Mann, and P.J. Codd. Automating neurosurgical tumor resection surgery: Volumetric laser ablation of cadaveric porcine brain with integrated surface mapping. *Lasers in Surgery and Medicine*, 50(10):1017–1024, 2018.

[21] Y. Shimojo, T. Nishimura, H. Hazama, N. Ito, and K. Awazu. Incident fluence analysis for 755-nm picosecond laser treatment of pigmented skin lesions based on threshold fluences for melanosome disruption. *Lasers in Surgery and Medicine*, 53(8):1096–1104, 2021.

[22] Y. Shimojo, T. Nishimura, T. Ozawa, D. Tsuruta, and K. Awazu. Nonlinear absorption-based analysis of energy deposition in melanosomes for 532-nm short-pulsed laser skin treatment. *Lasers in Surgery and Medicine*, submitted.

# Chapter 8

# Conclusion

The study aimed to develop a computational laser treatment using picosecond laser for rapid and effective clinical applications of laser devices with reproducible and precise laser treatment. Picosecond laser-skin interactions were experimentally and computationally analyzed at the tissue, cellular, and molecular scales to construct mathematical models of treatment and measure the physical parameters of the skin. The applicability of the developed computational laser treatment to the partial replacement of preclinical and clinical trials with the realization of reproducible and precise laser treatment was then evaluated.

Chapter 2 showed the optical properties of Asian epidermis, dermis, and subcutaneous fat measured with the DIS spectrophotometer and iMC technique. The absorption coefficients $\mu_a$ of Asian epidermis differed markedly from those of Caucasian and African epidermises, while the reduced scattering coefficients $\mu_s'$ of each layer in Asian skin were similar to those of the other types of skin. Computational simulations using a layered skin model and the measured optical properties analyzed the optical penetration depth $\delta$ and energy deposition $S$ in skin. The $\delta$ and $S$ complemented measurement data that were difficult to obtain in preclinical and clinical experiments. The computational simulations allow for the light propagation analysis in each Asian skin layer for computational laser treatment using picosecond laser.

In Chapter 3, the DLS analysis and SEM observation confirmed that the threshold fluences for melanosome disruption were 2.19 and 2.49 J/cm$^2$ for 550- and 750-ps laser pulses, respectively, while there was almost no change in the morphological and optical characteristics of melanins irradiated with picosecond laser. The results suggested that melanin is involved as a heat source to damage melanosomes in picosecond laser treatment of pigmented lesions. These fundamental findings related to picosecond laser-melanosome interactions will allow for the construction of a mathematical model to provide numerical indices for setting the irradiation parameters in computational laser treatment.

The nonlinear absorption-based analysis with the measured absorption cross-sections and nonradiative lifetimes was performed to evaluate energy deposition in melanosomes in Chapter 4. The picosecond laser was found to be most efficient in delivering energy to melanosomes. The computational analysis demonstrated that nonlinear absorption by melanin has a significant influence on the mechanism of short-pulsed laser treatment and can explain the difference in

treatment effect between picosecond and nanosecond lasers reported in clinical studies. These results suggested the feasibility of computational simulations for the augmentation of preclinical and clinical evaluations.

Chapter 5 highlights the evaluation of photothermal skin damage induced by a novel picosecond laser device in a computational clinical trial. The temperature rise and thermal damage of skin tissue were compared between the novel device and the approved devices with a computational simulation, and the photothermal damage caused by the novel device was shown to be less than that caused by the approved devices. These results demonstrated that computational laser treatment can be applied to computational clinical trials for the partial replacement of preclinical and clinical trials. The accumulation of clinical data and physical parameters will improve the reliability of computational clinical trials.

The light transport simulation revealed that the appropriate incident fluences of picosecond laser for pigmented lesions depend on the skin type and the depth of the lesions in Chapter 6. The incident fluences for Asian skin were similar to those for Caucasian skin while approximately half those for African skin. Choosing a larger spot size can disrupt melanosomes in deeper tissue with minimal collateral damage because a lesser incident fluence is necessary. These results demonstrated that computational laser treatment can provide numerical indices for determining distinct irradiation endpoints. These indices will contribute to designing a treatment protocol tailored to the optical properties of a patient and developing novel laser devices.

Chapter 7 discussed the prospects of computational laser treatment. To achieve medical care that improves patient well-being and quality of life, there is a growing demand for rapid and efficient processes of device development through regulatory evaluation to clinical use. Computational laser treatment can be a promising platform to facilitate the processes including the development of novel laser devices and treatment principles, the rapid and low-cost regulatory evaluation, the establishment of numerical indices for setting irradiation parameters, and the design of a treatment protocol tailored to a patient. Although applications of computational laser treatment are currently targeted at predicting immediate reactions to laser, future constructions of mathematical models for laser-induced biological responses will allow for long-term predictions related to subsequent treatment interventions and will greatly expand the applicability of computational simulations in laser treatment.

In conclusion, this study has demonstrated a computational laser treatment based on the multiscale analysis of picosecond laser-skin interactions. Since computational simulations provide a reproducible and quantitative evaluation of the treatment effect, computational clinical trials that augment and partially replace preclinical and clinical trials and robust setting of irradiation parameters based on numerical indices are achieved. With the recent focus on computational simulations in regulatory evaluations and the advance in optical measurement techniques, computational laser treatment can be a promising platform for rapid and low-cost clinical applications of novel laser devices and the design of a treatment protocol tailored to a patient.

# Acknowledgments

I would like to express my sincerest gratitude to my supervisor, Prof. Kunio Awazu of the Medical Beam Physics Laboratory for his invaluable guidance, encouragement, and support throughout my Ph.D. study. His comments based on his profound knowledge and experience have motivated me at the various stages of my research activity. My heartfelt appreciation goes to my dissertation committee: Prof. Takanori Kitada of the Nuclear Social Engineering Laboratory for his encouragement and invaluable advice on my dissertation and Assoc. Prof. Hisanao Hazama of the Medical Beam Physics Laboratory for his insightful comments and suggestions for this study.

I would like to show my greatest appreciation to Prof. Daisuke Tsuruta and Prof. Toshiyuki Ozawa of the Department of Dermatology, Graduate School of Medicine, Osaka Metropolitan University, for their support and encouragement. Their cooperation and insightful comments have been a great help in preparing human skin samples for optical property measurement and in improving the significance of my Ph.D. study from a clinical perspective. Many thanks are due to Prof. Miya Ishihara and Asst. Prof. Takeshi Hirasawa of the Department of Medical Engineering, National Defense Medical College, for their insightful discussions for computational modeling and simulation of picosecond laser-skin interactions. I am grateful to Assoc. Prof. Satoshi Seino of the Department of Management of Industry and Technology and Assoc. Prof. Yoko Akiyama of the Quantum Beam and Biomaterials Engineering Laboratory, for their cooperation in the experiment using the particle size analyzer. Furthermore, I would like to appreciate the technical assistance with the picosecond laser device provided by Cynosure LLC.

I would like to express my special appreciation to Asst. Prof. Takahiro Nishimura for his support and encouragement. Despite his busy schedule, he has always provided me with invaluable feedback on this study. I acknowledge Ms. Maiko Yagi, secretary of Awazu Laboratory, for her support in my research. I am also grateful to all the students of Awazu Laboratory, with whom I have shared many pleasures and pains. I would like to thank the Japan Society for the Promotion of Science and the Japan Science and Technology Agency, for their financial support that made it possible to complete this study. I would also like to thank the Japan Student Services Organization, for the scholarship I received during my master's course and the first year of my doctoral course.

Last but never least, I thank my parents and dearest brother and sister for their moral support and warm encouragement throughout my research work. This work could not have been done without them.

# List of Research Achievements

## Peer-Reviewed Papers

1. T. Nishimura*, T. Suzuki, Y. Shimojo, R. Teranishi, T. Ozawa, D. Tsuruta, K. Awazu. Mathematical modelling for antimicrobial photodynamic therapy mediated by 5-aminolaevulinic acid: an *in vitro* study. *Photodiagnosis and Photodynamic Therapy*, 40:103116, 2022.

2. K. Sudo*, Y. Shimojo, T. Nishimura*, K. Awazu. Three-dimensional transient simulation of $CO_2$ laser tissue vaporization and experimental evaluation with a hydrogel phantom. *Journal of Innovative Optical Health Sciences*, 15(3):2250016, 2022.

3. Y. Shimojo*, T. Nishimura*, H. Hazama, N. Ito, K. Awazu. Incident fluence analysis for 755-nm picosecond laser treatment of pigmented skin lesions based on threshold fluences for melanosome disruption. *Lasers in Surgery and Medicine*, 53(8):1096–1104, 2021.

4. 下条裕*, 西村隆宏*, 粟津邦男. XCAVATORファイバーによる接触式レーザー蒸散術のブタ前立腺組織を用いた熱影響解析. 日本レーザー医学会誌, 42(4):219–227, 2021.

5. T. Nishimura*, Y. Takai, Y. Shimojo, H. Hazama, K. Awazu, Determination of optical properties in double integrated sphere measurement by artificial neural network based method, *Optical Review*, 28(1):42–47, 2021.

6. Y. Shimojo*, T. Nishimura*, H. Hazama, T. Ozawa, K. Awazu. Measurement of absorption and reduced scattering coefficients in Asian human epidermis, dermis, and subcutaneous fat tissues in the 400- to 1100-nm wavelength range for optical penetration depth and energy deposition analysis. *Journal of Biomedical Optics*, 25(4):045002, 2020.

7. 西村隆宏*, 下条裕, 粟津邦男. レーザー治療における計算機援用レギュラトリーサイエンス, 日本レーザー医学会誌, 41(4):37–43, 2020.

8. Y. Shimojo*, T. Nishimura, H. Hazama, N. Ito, K. Awazu. Picosecond laser-induced photothermal skin damage evaluation by computational clinical trial, *Laser Therapy*, 29(1):61–72, 2020.

9. 西村隆宏*, 下条裕, 間久直, 粟津邦男. 熱損傷シミュレーションに基づく皮膚良性色素疾患治療用ナノ秒パルスレーザー装置の計算機臨床試験方法, 日本レーザー医学会誌, 40(4):301–308, 2020.

## Review Articles

1. 下条裕. 医療・医用レーザーデバイスを迅速に臨床応用するためのTranslational Research. Laborify, 2019. URL: https://laborify.net/2019/08/24/shimojo-medical-laser-transitional-research/

## Peer-Reviewed Proceedings

1. Y. Shimojo, T. Nishimura. Incident fluence model based on tissue optical properties and threshold fluence for melanosome disruption for 755-nm picosecond laser treatment of benign pigmented lesions. *Lasers in Surgery and Medicine*, 54(S34):S19, 2022.

2. Y. Takai, Y. Shimojo, T. Nishimura, K. Awazu. Artificial neural network based method to estimate optical properties in biological tissues for noise reduction. *Proceedings of Biophotonics Congress: Biomedical Optics*, JM3A.3, 2022.

3. Y. Shimojo, T. Nishimura, K. Awazu. Two-level model of melanin absorption in picosecond laser skin treatment. *Proceedings of SPIE*, 11958, Optical interaction with Tissue and Cells XXXIII, 1195802, 2022.

4. Y. Shimojo, T. Nishimura, H. Hazama, K. Awazu. Experimental analysis of morphological change in melanin for multiscale modeling of picosecond laser skin treatment. *Proceedings of SPIE*, 11640, Optical Interactions with Tissue and Cells XXXII, 1164005, 2021.

5. Y. Shimojo, T. Nishimura, H. Hazama, T. Ozawa, K. Awazu. Computational evaluation of ethnic difference in photothermal damage induced by laser skin treatments. *Proceedings of Biophotonics Congress: Biomedical Optics*, TU3A.1, 2020.

6. Y. Shimojo, T. Nishimura, H. Hazama, N. Ito, K. Awazu. *In silico* evaluation of thermal skin damage caused by picosecond laser irradiation. *Proceedings of Biophotonics Congress: Optics in the Life Sciences Congress*, DS1A.7, 2019.

## International Conferences

### Oral presentations (Peer-reviewed)

1. Y. Shimojo, T. Nishimura, K. Awazu. Quantitative evaluation of light distribution in skin tissue for short-pulsed laser treatment using Monte Carlo simulation combined with nonlinear absorption model of melanin. SPIE Photonics West BiOS (San Francisco, January 28th, 2023).

2. Y. Shimojo, T. Nishimura. Incident fluence model based on tissue optical properties and threshold fluence for melanosome disruption for 755-nm picosecond laser treatment of benign pigmented lesions. The 41st Annual Conference of the American Society for Laser Medicine and Surgery (Online, April 28th, 2022).

3. Y. Shimojo, T. Nishimura, K. Awazu. Two-level model of melanin absorption in picosecond laser skin treatment. SPIE Photonics West BiOS (Online, February 21st, 2022).

4. Y. Shimojo, T. Nishimura, H. Hazama, K. Awazu. Experimental analysis of morphological change in melanin for multiscale modeling of picosecond laser skin treatment. SPIE Photonics West BiOS (Online, March 6th, 2021).

5. Y. Shimojo, T. Nishimura, H. Hazama, N. Ito, K. Awazu. *In silico* evaluation of thermal skin damage caused by picosecond laser irradiation. Biophotonics Congress: Optics in the Life Sciences Congress (Tucson, April 14th, 2019).

### Poster presentations (Peer-reviewed)

1. Y. Takai, Y. Shimojo, T. Nishimura, K. Awazu. Artificial neural network based method to estimate optical properties in biological tissues for noise reduction. Biophotonics Congress: Biomedical Optics (Online, April 26th, 2022).

2. Y. Shimojo, T. Nishimura, H. Hazama, T. Ozawa, K. Awazu. Computational evaluation of ethnic difference in photothermal damage induced by laser skin treatments. Biophotonics Congress: Biomedical Optics (Online, April 21st, 2020).

## Domestic Conferences

### Oral presentations (Peer-reviewed)

1. [招待講演] 下条裕, 西村隆宏, 粟津邦男. コンピュテーショナルレーザー治療技術: 概念とピコ秒レーザー皮膚治療への適用に向けた開発. レーザー学会学術講演会第43回年次大会 (名古屋, 2023年1月18日).

2. 下条裕, 西村隆宏, 粟津邦男. メラニンの非線形吸収モデルに基づいたピコ秒レーザー皮膚治療の評価. 第43回日本レーザー医学会総会 (東京, 2022年10月15日).

3. 下条裕, 西村隆宏, 粟津邦男. 非線形吸収モデルに基づいた短パルス光照射によるメラノソーム光吸収量の*in silico*評価. 第33回日本レーザー医学会西日本大会 (大阪, 2022年7月30日).

4. [招待講演] 西村隆宏, 下条裕, 粟津邦男. レーザー治療機器開発におけるin silico評価技術. 第30回日本コンピュータ外科学会 (オンライン, 2021年11月22日).

5. 高井祐朔, 下条裕, 西村隆宏, 粟津邦男. ニューラルネットワークを用いた双積分球光学系に基づく光学特性計測におけるノイズ除去の検討. 第42回日本レーザー医学会総会 (オンライン, 2021年10月22日).

6. 須藤圭麻, 下条裕, 西村隆宏, 粟津邦男. レーザー組織蒸散の三次元過渡シミュレーション法の開発. 第42回日本レーザー医学会総会 (オンライン, 2021年10月22日).

7. 下条裕, 西村隆宏, 粟津邦男. ピコ秒レーザー皮膚治療におけるスキンタイプと病変深さに基づいた入射フルエンスの計算的評価. 第42回日本レーザー医学会総会 (オンライン, 2021年10月22日).

8. 高井祐朔, 下条裕, 西村隆宏, 間久直, 粟津邦男. ニューラルネットワークに基づく双積分球光学系を用いた生体組織の光学特性値推定. レーザー学会学術講演会第41回年次大会 (オンライン, 2021年1月21日).

9. 下条裕, 西村隆宏, 粟津邦男. レーザー皮膚治療における光深達深さ解析に与える組織層構造の影響評価. 第41回日本レーザー医学会総会 (オンライン, 2020年10月10日).

10. 下条裕, 西村隆宏, 間久直, 小澤俊幸, 粟津邦男. 双積分球光学系と逆モンテカルロ法に基づいた表皮, 真皮, 皮下脂肪の光学特性値計測. レーザー学会学術講演大会第40回年次大会 (仙台, 2020年1月20日).

11. 下条裕, 西村隆宏, 間久直, 粟津邦男. *Q*スイッチNd:YAGレーザーによるダブルパルス照射が皮膚組織に及ぼす熱影響の*in silico*評価. 第40回日本レーザー医学会総会 (浜松, 2019年10月20日).

12. 下条裕, 西村隆宏, 間久直, 伊東信久, 粟津邦男. 経皮的レーザー椎間板減圧術 (PLDD)における*in silico*による熱影響評価手法の開発. 第32回日本レーザー医学会関西地方会 (米子, 2019年7月6日).

13. 下条裕, 西村隆宏, 粟津邦男. ピコ秒レーザー治療機器に対する計算的評価手法の開発. レーザー学会学術講演会第39回年次大会 (東京, 2019年1月14日).

14. 下条裕, 西村隆宏, 粟津邦男. ピコ秒レーザー治療における正常皮膚組織に対する熱損傷の*in silico*評価. 第39回日本レーザー医学会総会 (東京, 2018年11月1日).

**Oral presentations (Not peer-reviewed)**

1. 下条裕, 西村隆宏, 粟津邦男. 皮膚色素性病変の破壊閾値に基づいたピコ秒パルス光照射条件の計算機援用設計. レーザー学会第557回研究会「光・レーザーの医学・医療応用」 (富山, 2021年10月15日).

2. [招待講演] 下条裕. 計算機シミュレーションによるピコ秒レーザー皮膚治療の設計と評価. 情報フォトニクス研究グループ研究会 (オンライン, 2021年9月17日).

3. [招待講演] 下条裕, 粟津邦男. 計算機シミュレーションに基づいたレーザー治療のレギュラトリーサイエンス. 第3期第7回レーザー学会「レーザーバイオ医療」技術専門委員会 (那覇, 2019年11月15日).

**Poster presentations (Not peer-reviewed)**

1. 西村隆宏, 下条裕, 粟津邦男. コンピュテーショナルレーザー治療技術の開発. 第16回新画像システム・情報フォトニクス研究討論会 (東京, 2022年6月17日).

## Awards

1. 下条裕. 令和4年度海外論文発表奨励賞. 一般社団法人生産技術振興協会 (2022年4月).
2. 下条裕. 2021年度技術交流助成交流プログラム (海外派遣). 中谷医工計測技術振興財団. 助成金375千円 (2021年12月).
3. 下条裕. 特に優れた業績による返還免除 (半額), 日本学生支援機構 (2021年6月).
4. 下条裕. 2020年度国際交流 (研究集会) 援助, ライフサイエンス振興財団. 助成金200千円 (2021年1月).
5. 下条裕. 若手アワード. 第41回日本レーザー医学会総会 (2020年10月).
6. 下条裕. 特に優れた業績による返還免除 (全額), 日本学生支援機構 (2020年6月).
7. 下条裕. 2019年度コニカミノルタ光みらい奨励金. 日本光学会. 光治療における生体組織光学に基づいた計算機臨床試験法の創出. 研究奨励金50千円 (2019年12月).
8. 下条裕. 2018年度技術交流助成交流プログラム (海外派遣). 中谷医工計測技術振興財団. 助成金275千円 (2019年3月).

## Competitive Research Funds

1. 下条裕. 非接触・非侵襲なロボット支援下レーザー手術機の開発. 科学技術振興機構, 戦略的創造研究推進事業, ACT–X, 6,000千円 (2021年10月–2024年3月).
2. 下条裕. ピコ秒レーザー皮膚治療における作用機序の解明と計算的評価手法の実証. 日本学術振興会, 科学研究費助成事業, 特別研究員奨励費, 1,500千円 (2021年4月–2023年3月).